Light-Matter Interaction of Molecules with Intense Ultrashort Laser Pulses

by

Andres Mora

B.S., Engineering Physics, 2019

B.A., Chemistry, 2019

A thesis submitted to the
Faculty of the Graduate School of the
University of Colorado in partial fulfillment
of the requirements for the degree of
Master of Science
Department of Physics
2019

This thesis entitled:
Light-Matter Interaction of Molecules with Intense Ultrashort Laser Pulses
written by Andres Mora
has been approved for the Department of Physics

Associate Research Prof. Agnieszka Jaroń-Becker

Prof. Andreas Becker

Date ____________________

The final copy of this thesis has been examined by the signatories, and we find that both the content and the form meet acceptable presentation standards of scholarly work in the above mentioned discipline.

Mora, Andres (MS Physics)

Light-Matter Interaction of Molecules with Intense Ultrashort Laser Pulses

Thesis directed by Associate Research Prof. Agnieszka Jaroń-Becker

Over the last few decades, laser technology has greatly advanced resulting in high intensity ultrashort laser pulses operating at many frequencies, which have made a huge impact in the field of Atomic, Molecular and Optical Physics. As a result of these advances, new phenomena have been discovered and studied in atoms such as high harmonic generation, multiphoton and above-threshold ionization, among many more. While methods have been developed to study such phenomena, such as the strong-field ionization, and the tunneling ionization models, these models fail to properly describe the interaction between high intensity ultrashort laser pulses and molecules due to their complex multielectron nature, and extra degrees of freedom.

In this thesis we apply time-dependent density functional theory, optical Bloch equations, and Floquet theory to study the interaction of high intensity ultrashort laser pulses with molecules in the context of high harmonic generation, strong field ionization and nonadiabatic electron localization. Based on our numerical results we analyze new features in high harmonic spectra of molecules such as the ellipticity of generated harmonics in CO_2, as previously measured in experiments, and the appearance of Mollow sidebands in the respective spectra of N_2^+ and $C_2H_4^+$. We also consider the modification of harmonic spectra by the interaction of two linearly polarized pulses and two circularly polarized pulses interacting with molecules. We then look into the effects of a laser induced coupling of orbitals in the context of ionization and show that as a result of the coupling, ionization contributions from inner shell orbitals are greatly enhanced. We also consider how the addition of a second linearly polarized pulse affects the ionization of molecules. Lastly, we study the effects of electron localization via the laser induced coupling of orbitals for the interactions between molecules and lasers in the context of time-dependent density functional theory and Floquet theory.

Dedication

To my family and friends.

Acknowledgements

I would like to thank and express my gratitude to Agnieszka Jaron-Becker, my research advisor. Without her help and patience I would not have been able to write this thesis.

In addition I would like to thank her husband Andreas Becker for all the guidance over the years.

I would like to also thank all of the graduate students within the group, namely Tennesse Joyce, Brynn Reiff, Joel Venzke, Spencer Walker, Yonas Gebre, and Lauren Bauerle. Thank you for the help and guidance as well as the good memories I have gained.

I will also like to thank the JILA computing group for all of their help whenever I needed insight into software and computational needs.

Contents

Chapter

Appendix

Tables

Table

Figures

Figure

Chapter 1

Introduction

In the world of physics there exist many disciplines that aim to help us understand the behavior of nature ranging from phenomena related to the cosmos, to the behavior of sub-atomic particles. One of those disciplines is Atomic, Molecular and Optical Physics (AMO Physics) which includes the study of the interaction between matter and light. Within itself, AMO is a broad area of physics that spans a variety of topics such as laser cooling and atom trapping, quantum optics, and the study of ultrafast processes in atoms and molecules by ultrashort laser pulses.

Ever since the laser was invented in 1960 it has become a fundamental tool to study the dynamics and response of atomic and molecular systems which in turn has expanded our knowledge of how matter interacts with light. We know that at low laser intensities $I < 10^{13}\frac{W}{cm^2}$ the dominating process is related to emission or absorption of few photons and can be properly analyzed with the use of perturbation theory. However, with technological advances in laser science we were able to increase the intensity threshold beyond what perturbation theory can explain. In turn, a new realm of light-matter interaction was opened. At intensities of $I \geq 10^{13}\frac{W}{cm^2}$ the interaction between the electrons in a system with the electric field of the laser pulse and the Coulomb interaction become comparable, leading to interesting highly nonlinear high order processes due to the absorption and emission of many photons, such as high harmonic generation (HHG), and above threshold ionization (ATI).

So far, the interaction between atomic systems and intense laser pulses has been extensively studied and considered to be well understood. Many theoretical methods exist to describe such interactions and the results have so far agreed with those obtained via experiments. High-order processes such as ATI have been successfully modeled by methods such as the Keldysh, Faisal, Reiss theory (KFR) and quasi-static tunneling models [1,2,3], where it is assumed that only the most loosely bound electron responds to an external field in an adiabatic manner. This is known as the single-active electron approximation (SAE) and so far it has been shown that it works well for atomic systems due to the large energy spacing between atomic orbitals.

However, unlike for atoms, the interaction between molecular systems and strong laser fields is less well understood. This is largely due to the ever increasing complexity brought upon by multielectron effects, rotational and vibrational degrees of freedom, and multi-center nuclear potential surfaces, among many others [4,5,6,7,8,9,10]. As a result, many previous approximations that are useful when studying intense laser light interaction with atoms no longer apply and the theories must be modified, as approximations like SAE begin to break down due to the closer spacing in energy levels, and due to the multielectron effects present.

In this thesis we consider ab-initio methods and certain approximation models that allow us to understand the more complex dynamics occurring in the interaction of intense lasers and molecules. The thesis is organized as follows: In chapter 2 we introduce the theoretical methods we use to study our systems. These include time-dependent density functional theory (TDDFT), the optical Bloch equations, and lastly Floquet theory.

In chapter 3 we investigate multielectron effects in high-harmonic generation, in the cases where either one or two lasers are interacting with molecular systems. We describe the differences that arise in HHG from molecules compared to what has been observed in atoms. We also analyze the appearance of Mollow sidebands present in HHG spectra as a result of laser induced coupling between molecular orbitals in N_2^+ and $C_2H_4^+$ by utilizing TDDFT and optical Bloch equations, and compare both results from theories. We then analyze the ellipticity of harmonics from CO_2 which agrees with previously conducted experiments. We end the chapter by considering the interaction of bichromatic circularly polarized pulses interacting with H_2 and describe the differences that arise in HHG spectra as a result of the fields used.

In chapter 4 we consider the effects of laser induced resonances in multiphoton ionization, and study how such couplings of orbitals can enhance ionization from inner shell orbitals in molecules like N_2^+ and $C_2H_4^+$. We study the case for both one color interactions as well as two color interactions and explain the differences between them.

We then analyze nonadiabatic electron localization arising from the coupling of orbitals in chapter 5, and show how such dynamics can be visualized from the models we utilize such as TDDFT and Floquet theory. We again consider the cases of one and two-color laser interactions and explain how they both differ.

Lastly, we summarize our findings in chapter 6.

Chapter 2

Theoretical Methods in Ultrafast Atomic, Molecular, And Optical Physics

2.1 Multi-Electron Systems

Atoms and molecules are multielectron systems. A system of N electrons interacting with a laser field can be described by its wavefunction $\Psi(\mathbf{r},t)$ ($\mathbf{r} = [\mathbf{r}_1,...,\mathbf{r}_N]$) which obeys the time-dependent Schrödinger equation (note: we will be working in atomic units, $e = m = \hbar = 1$, in the whole thesis):

$$\hat{H}\Psi(\mathbf{r},t) = i\frac{\partial\Psi(\mathbf{r},t)}{\partial t}, \tag{2.1}$$

where the Hamiltonian H is written in the form

$$H(\mathbf{r},t) = T(\mathbf{r}) + V_{ee}(\mathbf{r}) + V_{ne}(\mathbf{r}) + V_{laser}(\mathbf{r},t), \tag{2.2}$$

with $T(\mathbf{r})$ being the kinetic energy of the electrons

$$T(\mathbf{r}) = -\frac{1}{2}\sum_{i=1}^{N}\nabla_i^2. \tag{2.3}$$

The second term denoted $V_{ee}(\mathbf{r})$ is the electron-electron interaction which has the form

$$V_{ee}(\mathbf{r}) = \sum_{i<j=1}^{N}\frac{1}{|\mathbf{r}_i - \mathbf{r}_j|}, \tag{2.4}$$

$V_{ne}(\mathbf{r})$ corresponds to the nuclear-electron interaction given by

$$V_{ne}(\mathbf{r}) = -\sum_{i,k}\frac{Z_k}{|\mathbf{r}_i - \mathbf{R}_k|}, \tag{2.5}$$

where $\mathbf{R}_k$ is the position and Z_k is the charge of the k^{th} nucleus. The last term $V_{laser}(\mathbf{r},t)$ includes the interaction between the electrons and the applied laser field

$$V_{laser}(\mathbf{r},t) = E_o f(t) sin(\omega t)\left(\sum_{i=1}^{N} \mathbf{r}_i \cdot \hat{n}\right), \tag{2.6}$$

where E_o is the amplitude of the electric field, $f(t)$ is the envelope of the pulse, ω is the frequency of the laser, and $\hat{n}$ is the polarization direction of the field.

While the multielectron Schrödinger equation describes the system fully, it is computationally expensive to solve for $\Psi(\mathbf{r},t)$ in the case of larger systems. Due to this, it is indeed currently impossible to exactly solve the multielectron Schrödinger equation for systems with more than two electrons interacting with intense laser pulses in a reasonable amount of time. Fortunately, there exists an alternative approach to approximately solve multielectron systems known as Density Functional Theory (DFT).

2.1.1 Hohenberg-Kohn Theorem

The basis of DFT originates from the Hohenberg-Kohn (HK) theorem [11,12,13] which states that the external potential given by:

$$\hat{V}_{ext} = \hat{V} + \hat{W} = \sum_{i=1}^{N} v(\mathbf{r}_i) + \frac{1}{2}\sum_{i,k,i\neq k}^{N} \frac{1}{|\mathbf{r}_i - \mathbf{r}_k|}, \tag{2.7}$$

of the system is a functional of the electron density $\rho(\mathbf{r})$, and that the ground state of a system can be determined by its electronic density given by

$$\rho_{gs}(\mathbf{r}) = N\sum_{\sigma}\int d\mathbf{x}_2 ... \int d\mathbf{x}_N |\Psi_{gs}(\mathbf{r},\sigma,\mathbf{x}_2,...,\mathbf{x}_N)|^2. \tag{2.8}$$

We can show this by considering a ground state wavefunction $\psi(\mathbf{r})$ with an electron density $\rho(\mathbf{r})$ for an external potential $V(\mathbf{r})$, with a Hamiltonian H and energy E, and another ground state wavefunction $\psi'(\mathbf{r})$ corresponding to a second external potential $V'(\mathbf{r})$ with a Hamiltonian H' and energy E', which gives the same electron density $\rho(\mathbf{r})$. Due to the variational principle we can then say that:

$$\begin{aligned} \langle\psi|H|\psi\rangle <& \langle\psi'|H|\psi'\rangle = \langle\psi'|H'|\psi'\rangle + \langle\psi'|H - H'|\psi'\rangle \\ &= E' + \int (V(\mathbf{r}) - V'(\mathbf{r}))\rho(\mathbf{r})d\mathbf{r}, \end{aligned} \tag{2.9}$$

which gives the following:

$$E < E' + \int (V(\mathbf{r}) - V'(\mathbf{r}))\rho(\mathbf{r})d\mathbf{r}, \tag{2.10}$$

and also for the case of the primed and unprimed indices being reversed:

$$E' < E + \int (V'(\mathbf{r}) - V(\mathbf{r}))\rho(\mathbf{r})d\mathbf{r}. \tag{2.11}$$

If we then add equations (2.10) and (2.11) we get the following contradiction:

$$E + E' < E + E', \tag{2.12}$$

so we see that the external potential $V(\mathbf{r})$ is indeed a unique functional of the ground state electron density $\rho(\mathbf{r})$. Or in other words, the ground state wavefunction $\Psi_{gs}(\mathbf{r})$ is a functional of the ground state density $\rho_{gs}(\mathbf{r})$, so it can be written as

$$\Psi_{gs}(\mathbf{r}) = \Psi_{gs}[\rho_{gs}(\mathbf{r})], \tag{2.13}$$

where square brackets denote functional dependence. This then leads to the fact that any observable corresponding to the ground state is also a functional of the density $\rho_{gs}(\mathbf{r})$

$$O[\rho_{gs}(\mathbf{r})] = \langle\Psi_{gs}[\rho_{gs}(\mathbf{r})]|O|\Psi_{gs}[\rho_{gs}(\mathbf{r})]\rangle. \tag{2.14}$$

2.1.2 Density-Functional Theory and the Kohn-Sham Equations

Based on the HK theorem it has been established that the observables of a system are functionals of the density $\rho_{gs}(\mathbf{r})$, we therefore need to consider ways to solve for the density. This can be done using the Kohn-Sham equations.

Consider a system of noninteracting particles with a Hamiltonian given by:

$$\hat{H}_s = \hat{T} + \hat{V}_s = \sum_{i=1}^{N} \left(-\frac{\nabla_i^2}{2} + v_s(\mathbf{r}_i) \right), \tag{2.15}$$

where V_s is an arbitrary external potential. We can write the associated total energy of the system as a functional given by:

$$E_{v_s}[\rho] = T_s[\rho] + \int d^3 r \rho(\mathbf{r}) v_s(\mathbf{r}), \tag{2.16}$$

where $\rho(\mathbf{r})$ is the electron density of the system.

Since the particles are non-interacting, a Slater determinant can be used to approximate the ground state wavefunction $\Psi_{gs}(\mathbf{r})$ of the N-particle system:

$$\Psi_{gs}(\mathbf{r}) = \frac{1}{\sqrt{N!}} \begin{vmatrix} \phi_1(\mathbf{r}_1) & \phi_1(\mathbf{r}_2) & \phi_1(\mathbf{r}_3) & \dots & \phi_1(\mathbf{r}_N) \\ \phi_2(\mathbf{r}_1) & \phi_2(\mathbf{r}_2) & \phi_2(\mathbf{r}_3) & \dots & \phi_2(\mathbf{r}_N) \\ \vdots & \vdots & \vdots & & \vdots \\ \phi_N(\mathbf{r}_1) & \phi_N(\mathbf{r}_2) & \phi_N(\mathbf{r}_3) & \dots & \phi_N(\mathbf{r}_N) \end{vmatrix} \tag{2.17}$$

where the orbitals $\phi_i(\mathbf{r})$ are solutions to the single particle Schrödinger equation

$$-\frac{1}{2}\nabla^2 \phi_i(\mathbf{r}_i) + V_s(\mathbf{r}_i)\phi_i(\mathbf{r}_i) = \epsilon_i \phi_i(\mathbf{r})_i, \tag{2.18}$$

and the ground state density of the N electron system is given by

$$\rho_{gs}(\mathbf{r}) = \sum_{i=1}^{N} |\phi_i(\mathbf{r})|^2. \tag{2.19}$$

In this case the HK theorem applies and there exists a one to one mapping between the ground state density $\rho(\mathbf{r})$ and the potential $V_s(\mathbf{r})$. The energy of the system is given by

$$E_{s,gs}[\rho] = T_s[\rho_{gs}] + \int d\mathbf{r} \rho(\mathbf{r}) v_s(\mathbf{r}) = \sum_{i=1}^{N} \int d\mathbf{r} \phi_i^*(\mathbf{r})(-\frac{1}{2}\nabla_i^2)\phi_i(\mathbf{r}) + \int d\mathbf{r} \rho(\mathbf{r}) v_s(\mathbf{r}). \tag{2.20}$$

Now consider a system of interacting particles with an external potential denoted by $V_{ext}(\mathbf{r})$. The ground state density $\rho_{gs}(\mathbf{r})$ for this system can be obtained from the ground state density of a system of noninteracting particles with a potential denoted by $V_s(\mathbf{r})$. This turns the problem of solving a multielectron Schrödinger equation into multiple noninteracting single particle Schrödinger-like equations. In turn, this greatly reduces the computational costs needed to numerically solve such systems.

For a system of interacting particles the energy functional is given by

$$E[\rho_{gs}] = T_s[\rho_{gs}] + V_H[\rho_{gs}] + E_{xc}[\rho_{gs}] + V[\rho_{gs}]. \tag{2.21}$$

The second term $V_H[\rho_{gs}]$ is the Hartree energy (classical Coulomb energy) which is given by

$$V_H[\rho_{gs}] = \frac{1}{2}\int d\mathbf{r} \int d\mathbf{r}' \frac{\rho_{gs}(\mathbf{r})\rho_{gs}(\mathbf{r}')}{|\mathbf{r}-\mathbf{r}'|}, \tag{2.22}$$

while $E_{xc}[\rho_{gs}]$ is the exchange correlation energy:

$$E_{xc}[\rho_{gs}] = T[\rho_{gs}] - T_s[\rho_{gs}] + U[\rho_{gs}] - \frac{1}{2}\int d\mathbf{r} \int d\mathbf{r}' \frac{\rho_{gs}(\mathbf{r})\rho_{gs}(\mathbf{r}')}{|\mathbf{r}-\mathbf{r}'|}. \tag{2.23}$$

Taking the derivative of the exchange correlation energy, gives the exchange correlation potential

$$V_{xc}[\rho_{gs}] = \frac{\delta E_{xc}}{\delta \rho_{gs}}. \tag{2.24}$$

This potential has an unknown form, but can be approximated for different systems.

For a system of interacting particles the variational principle with respect to the electron density results in

$$0 = \frac{\delta T_s[\rho_{gs}]}{\delta \rho_{gs}} + \frac{\delta V[\rho_{gs}]}{\delta \rho_{gs}} + \frac{\delta V_H[\rho_{gs}]}{\delta \rho_{gs}} + \frac{\delta E_{xc}[\rho_{gs}]}{\delta \rho_{gs}}. \tag{2.25}$$

Similarly, for a system of noninteracting particles the variational principle with respect to density yields

$$\frac{\delta E_{xc}[\rho_{gs}]}{\delta \rho_{gs}} = 0 = \frac{\delta T_s[\rho_{gs}]}{\delta \rho_{gs}} + \frac{\delta V_s[\rho_{gs}]}{\delta \rho_{gs}}. \tag{2.26}$$

Comparing the variational principle for both the interacting and noninteracting system, we get

$$v_s(\mathbf{r}) = v_{ext}(\mathbf{r}) + v_H(\mathbf{r}) + v_{xc}(\mathbf{r}), \tag{2.27}$$

to achieve both minimizations resulting in the same electron density $\rho_s(\mathbf{r}) = \rho(\mathbf{r})$. This implies that the density of an interacting system within an external potential $v_{ext}(\mathbf{r})$ can be determined by solving the Schrödinger equation for many non-interacting particles in a potential $v_s(\mathbf{r})$, only if the exchange-correlation potential is known. Based on this assumption, the orbitals of the noninteracting system can be obtained by solving the Kohn-Sham (KS) equation, given by

$$-\frac{1}{2}\nabla^2\phi_i(\mathbf{r}) + v_s(\mathbf{r})\phi_i(\mathbf{r}) = \epsilon_i\phi_i(\mathbf{r}), \tag{2.28}$$

and the electron density of the interacting system can then be obtained via

$$\rho(\mathbf{r}) = \sum_{i=1}^{N} |\phi_i(\mathbf{r})|^2. \tag{2.29}$$

The KS equations must be solved self-consistently because both the terms $v_H(\mathbf{r})$ and $v_{xc}(\mathbf{r})$ depend on the density $\rho(\mathbf{r})$, which depends on the orbitals $\phi_i(\mathbf{r})$, which in turn depend on $v_s(\mathbf{r})$. Due to this, the calculation starts with an initial guess for the electron density $\rho(\mathbf{r})$, then the potential $v_s(\mathbf{r})$ is obtained, which leads to a solution of the KS equation $\phi_i(\mathbf{r})$, which then yields a new density $\rho(\mathbf{r})$. This process is repeated until the system converges to the correct ground state density. Once convergence is obtained, then observables for the system can be calculated.

2.2 Runge-Gross Theorem

The Schrödinger equation maps an external potential $v(\mathbf{r}, t)$ to a time-dependent wavefunction $\Psi(\mathbf{r}, t)$ with a given initial state Ψ_o. However, there exists a second mapping between the density $\rho(\mathbf{r}, t)$ and $\Psi(\mathbf{r}, t)$, which leads to the Runge-Gross theorem [11,12,13] which states that given two electron densities $\rho(\mathbf{r}, t)$ and $\rho'(\mathbf{r}, t)$, both obtained from an initial wave function Ψ_o which is influenced by two different potentials $v(\mathbf{r}, t)$ and $v'(\mathbf{r}, t)$, will become different after a given time t_o. This implies that there is a one-to-one correspondence between densities and potentials obtained from a given initial wavefunction.

$$\rho(\mathbf{r}, t) \to V(\mathbf{r}, t) \to \Psi(\mathbf{r}, t). \tag{2.30}$$

2.3 Time-Dependent Density-Functional Theory (TDDFT)

An extension of DFT beyond the static potential is TDDFT, which considers the system being subjected to a time dependent external potential, typically for laser-molecule interactions, of the form of equation (2.6). There are several assumptions made in this description

(1) The field is treated classically since at high intensities the field has a large photon density.

(2) The dipole approximation is used, which holds when the wavelength of the laser field is larger than the size of the system.

The electromagnetic field is treated as purely electric field, and its magnetic component can be neglected for the considered range of laser frequencies and intensities.

In the case of a time dependent external potential, the Runge-Gross theorem states that there is a one-to-one mapping between the electron density $\rho(\mathbf{r}, t)$ and the external potential $v(\mathbf{r}, t)$. Therefore, instead of solving a many body time dependent Schrödinger equation, the density can be found by using the time dependent Kohn-Sham equation given by

$$-\frac{1}{2}\nabla^2\phi_i(\mathbf{r}, t) + v_{ks}(\mathbf{r}, t)\phi_i(\mathbf{r}, t) = i\frac{\partial}{\partial t}\phi_i(\mathbf{r}, t), \tag{2.31}$$

where for the time-dependent case, the external potential includes the potential from the laser field and is of the form:

$$v_{ks}(\mathbf{r}, t) = v_{ext}(\mathbf{r}) + v_H(\mathbf{r}) + v_{xc}(\mathbf{r}) + v_{laser}(\mathbf{r}, t). \tag{2.32}$$

By solving the time-dependent Kohn-Sham equations the time-dependent density is then given by

$$\rho(\mathbf{r}, t) = \sum_{i=1}^{N} |\phi_i(\mathbf{r}, t)|^2, \tag{2.33}$$

where $\phi_i(\mathbf{r}, t)$ is the i^{th} time-dependent Kohn-Sham orbital.

2.4 Spin Polarized Time-Dependent Density Functional Theory

A useful feature of DFT and TDDFT is that spin-dependent cases can be considered [13]. This can be implemented in both the time-independent and time-dependent Kohn-Sham equations by adding a spin index $\sigma =\uparrow, \downarrow$, which gives

$$\left[-\frac{1}{2}\nabla^2 + v_\sigma(\mathbf{r},t) + \int d^3r' \frac{\rho(\mathbf{r'},t)}{|\mathbf{r}-\mathbf{r'}|} + v_{XC,\sigma}[\rho_\uparrow,\rho_\downarrow](\mathbf{r},t)\right]\phi_{i,\sigma}(\mathbf{r},t) = i\frac{\partial}{\partial t}\phi_{i,\sigma}(\mathbf{r},t), \tag{2.34}$$

where upon solving, the total density is given by:

$$\rho(\mathbf{r},t) = \sum_{\sigma=\uparrow,\downarrow} \rho_\sigma(\mathbf{r},t) = \sum_{\sigma=\uparrow,\downarrow}\sum_{i=1}^{N} |\phi_{i,\sigma}(\mathbf{r},t)|^2. \tag{2.35}$$

2.5 Implementation of Time-dependent Density functional Theory

The solution of the KS equation can be found numerically by discretizing both the time and spatial components via some finite difference method. This converts the KS equation into a matrix equation. To obtain the initial wavefunction, the eigenvalue problem is solved self-consistently with an initial guess for the ground state needed. After the ground state of the system has been obtained, the wavefunction can be propagated in time. There are a variety of methods available to numerically solve the KS equations [14].

Given some initial wavefunction for the j^{th} orbital $\psi_j(t=0)$, time evolution states that after some time Δt the wavefunction is given by:

$$\psi_j(t+\Delta t) \approx \frac{1 - i\frac{\Delta t}{2}H(t+\frac{\Delta t}{2})}{1 + i\frac{\Delta t}{2}H(t+\frac{\Delta t}{2})}\psi_j(t). \tag{2.36}$$

This time propagation scheme is known as Crank-Nicolson and it is what was used to generate the results presented in this thesis. The Hamiltonian operator $H(t)$ can be evaluated by using a finite difference scheme [14] where the wavefunction of the system is defined on a discrete spatial and temporal grid.

For the results presented in this thesis, all of the simulations were performed using the ab-initio TDDFT software Octopus [15,16,17]. The simulations for the molecules were performed at their equilibrium bond length with a trapezoidal or $sin^2(.)$ pulse shape at wavelengths 400 nm, 600 nm, and 800 nm. In addition, the simulation grid used is spherically shaped with a varying radius depending on intensity of the pulse. The exchange correlational functional used in the simulations was the local-density approximation (LDA) [17] and an average-density self-interaction correction was applied [18].

2.6 Absorbing-Boundary Conditions in Time-Dependent Density-Functional Theory

A property of TDDFT is that the calculated time-dependent wavefunctions conserve their norm for all times, which can be given by:

$$\int d^3r\rho(\mathbf{r},t) = N, \tag{2.37}$$

where N is the norm, or number of particles. This then implies probability conservation, meaning that probability density cannot be created or destroyed.

In many situations in which a system is driven by a strong electric field, as in this thesis, ionization occurs, and boundary conditions at the edge of the numerical grid have to be considered. Numerically speaking, if one is calculating the dynamics of a system in the presence of a strong electric field via TDDFT, the outgoing wavefunctions driven by the field, will indeed return, if the boundary conditions are reflective. Fortunately, absorbing boundary conditions can be applied to the real-space grid in which the calculation is taking place. This is done by adding a negative short range complex valued potential to the total potential in the asymptotic region which is located far away from the system that is being ionized. If the outgoing wavepacket hits the absorbing boundary and is absorbed, the norm of the wavefunction will no longer be conserved and the outgoing portion of the wavefunction is assumed to describe ionization.

2.7 Optical Bloch Equations

While TDDFT captures the full 3-dimensional dynamics of a system in the presence of a strong electric field, it can be computationally expensive and time-consuming. Therefore, it is useful to consider simple models which can capture some of the dynamics that one can investigate using TDDFT. We apply the optical-Bloch equations, which are useful when analyzing the resonant dynamics in two-level systems. Unfortunately, when using such simple models many aspects of the dynamics are not seen. In the case of high-harmonic generation, which we will study closely in this thesis, the optical Bloch equations fail to capture the ionization process of HHG as there is no way to correctly include the continuum into the picture in a straight forward manner. Yet, the simple picture gives insight into some of the dynamics we will investigate.

2.7.1 Derivation of Optical-Bloch Equations

Consider a two level system with a ground state labeled $|g\rangle$ and an excited state labeled $|e\rangle$ with energies E_g and E_e, respectively. Figure 2.1 shows a diagram of such a system.

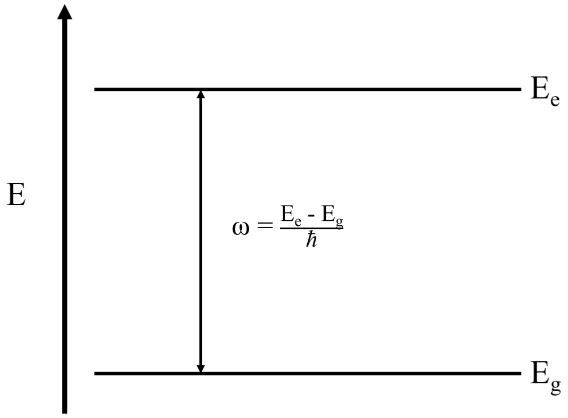

Figure 2.1: Schematic diagram of a two-level system with energies E_g and E_e, representing states $|g\rangle$ and $|e\rangle$ respectively.

For such a system we can write the Hamiltonian as:

$$\hat{H} = \hat{H}_A - \hat{\mathbf{d}} \cdot \hat{E}(\mathbf{r}_o), \tag{2.38}$$

where $\hat{H}_A$ is the unperturbed atomic Hamiltonian of the system, $\hat{d}$ is the transition dipole moment of the atom and $\hat{E}(\mathbf{r}_o)$ is the electric field operator evaluated at the position of the dipole $\mathbf{r}_o$. We make the assumption that the electric field is monochromatic and has a frequency close to the transition frequency between the states $|g\rangle$ and $|e\rangle$. We then find the matrix elements of the various atomic operators which are:

$$\begin{aligned} \langle e|\hat{H}_A|e\rangle &= E_e, \qquad & \langle g|\hat{H}_A|g\rangle &= E_g \\ \langle e|\hat{H}_A|g\rangle &= 0, \qquad & \langle g|\hat{H}_A|e\rangle &= 0, \end{aligned} \tag{2.39}$$

and

$$\begin{aligned} \langle e|\hat{\mathbf{d}}|e\rangle &= 0, \qquad & \langle g|\hat{\mathbf{d}}|g\rangle &= 0 \\ \langle e|\hat{\mathbf{d}}|g\rangle &= \mathbf{d}_{eg}, \qquad & \langle g|\hat{H}_A|e\rangle &= (\mathbf{d}_{eg})^*, \end{aligned} \tag{2.40}$$

where d_{eg} and $(d_{eg})^*$ are the transition dipole moments between states and can be written as:

$$\mathbf{d}_{eg} = \mathbf{d}_r + i\mathbf{d}_i, \qquad \mathbf{d}_{ge} = \mathbf{d}_r - i\mathbf{d}_i, \tag{2.41}$$

where $\mathbf{d}_r$ and $\mathbf{d}_i$ are the real and imaginary components of the dipole moment. From here we can now express the dipole operator in terms of Pauli matrices:

$$\hat{\mathbf{d}} = \mathbf{d}_r\hat{\sigma}_x - \mathbf{d}_i\hat{\sigma}_y. \tag{2.42}$$

Similarly we can write the atomic Hamiltonian in terms of Pauli operators given by:

$$\hat{H}_A = \frac{1}{2}(E_e + E_g)\hat{I} + \frac{1}{2}(E_e - E_g)\hat{\sigma_z}, \tag{2.43}$$

where $\hat{I}$ is the identity matrix. The full form of the Hamiltonian given in equation (2.38) is then:

$$\hat{H} = \frac{1}{2}(E_e + E_g)\hat{I} + \frac{1}{2}(E_e - E_g)\hat{\sigma_z} - (\mathbf{d}_r \cdot \hat{\mathbf{E}})\hat{\sigma}_x + (\mathbf{d}_i \cdot \hat{\mathbf{E}})\hat{\sigma}_y. \tag{2.44}$$

If we consider the Heisenberg equation for some operator $\hat{O}$ given by:

$$i\hbar\dot{\hat{O}} = [\hat{O}, \hat{H}], \tag{2.45}$$

we then obtain three equations for the Pauli matrices given by:

$$\dot{\hat{\sigma}}_x(t) = -\omega_o\hat{\sigma}_y(t) + \frac{2}{\hbar}[\mathbf{d}_i \cdot \hat{\mathbf{E}}(t)]\hat{\sigma}_z(t), \tag{2.46}$$

$$\dot{\hat{\sigma}}_y(t) = \omega_o\hat{\sigma}_x(t) + \frac{2}{\hbar}[\mathbf{d}_r \cdot \hat{\mathbf{E}}(t)]\hat{\sigma}_z(t), \tag{2.47}$$

$$\dot{\hat{\sigma}}_z(t) = -\frac{2}{\hbar}[\mathbf{d}_r \cdot \hat{\mathbf{E}}(t)]\hat{\sigma}_y(t) - \frac{2}{\hbar}[\mathbf{d}_i \cdot \hat{\mathbf{E}}(t)]\hat{\sigma}_x(t), \tag{2.48}$$

where ω_o is the transition frequency between states:

$$\omega_o = \frac{E_e - E_g}{\hbar}. \tag{2.49}$$

We then introduce the expectation values of the Pauli operators given by:

$$s_i(t) =< \hat{\sigma}_i >, \ i = x, y, z, \tag{2.50}$$

so then our coupled equations can be written as:

$$\dot{s}_x(t) = -\omega_o s_y(t) + \frac{2}{\hbar}[\mathbf{d}_i \cdot \hat{\mathbf{E}}(t)]s_z(t), \tag{2.51}$$

$$\dot{s}_y(t) = \omega_o s_x(t) + \frac{2}{\hbar}[\mathbf{d}_r \cdot \hat{\mathbf{E}}(t)]s_z(t), \tag{2.52}$$

$$\dot{s}_z(t) = -\frac{2}{\hbar}[\mathbf{d}_r \cdot \hat{\mathbf{E}}(t)]s_y(t) - \frac{2}{\hbar}[\mathbf{d}_i \cdot \hat{\mathbf{E}}(t)]s_x(t), \tag{2.53}$$

which are the optical Bloch equations that describe the interaction of a two-level atom with an electric field.

2.8 Floquet Theory and The Dressed-State Picture

There is yet another theoretical method that gives insight into the interaction of atoms and molecules with laser pulses, known as Floquet Theory. In this method we consider an intense field interacting with a system, whose interaction energy is labeled $H_{int}(t)$, so the full time-dependent Hamiltonian is of the form:

$$H(t) = H_o + H_{int}(t), \tag{2.54}$$

where H_o is some field free Hamiltonian. We consider that the laser pulse is a CW monochromatic field of intensity I such that $H_{int}(t)$ is periodic in time. This then implies that the time-dependent Hamiltonian in equation (2.54) is also periodic in time:

$$H(t) = H(t + \tau), \tag{2.55}$$

where τ is the optical period of the applied laser field, equal to $2\pi/\omega$, where ω is the optical frequency of the pulse. With this, the time-dependent Schrödinger equation (TDSE) can be written as:

$$i\frac{\partial}{\partial t}|\Psi(t)\rangle = H(t)\Psi(t) = [H_o + H_{int}(t)]|\Psi(t)\rangle, \tag{2.56}$$

where H_o is the field-free Hamiltonian. According to Floquet theory, the solution to the TDSE for this system can be written as:

$$|\Psi(t)\rangle = e^{-iE_F t}|P_E(t)\rangle, \tag{2.57}$$

where, E_F is the Floquet quasienergy, and $|P_E(t)\rangle$ is some state vector that is periodic in time:

$$|P_E(t + \tau)\rangle = |P_E(t)\rangle. \tag{2.58}$$

We can then find the state vector $|P_E(t)\rangle$ and the quasienergy E_F by considering the TDSE to be a time-independent problem and write $|P_E(t)\rangle$ as:

$$|P_E(t)\rangle = \sum_{n=-\infty}^{\infty} e^{-in\omega t}|F_n(E)\rangle. \tag{2.59}$$

Then the solution to the TDSE given in equation (2.57) can be written as:

$$|\Psi(t)\rangle = e^{-iE_F t}\sum_{n=-\infty}^{\infty} e^{-in\omega t}|F_n(E)\rangle. \tag{2.60}$$

We can also expand the interaction term $H_{int}(t)$ as a Fourier series resulting in:

$$H_{int}(t) = \sum_{n=-\infty}^{\infty} (H_{int})_n e^{-in\omega t}. \tag{2.61}$$

We substitute equations (2.60) and (2.61) into the TDSE given in equation (2.56) and obtain the following form:

$$(H_o - n\omega)|F(E)_n\rangle + \sum_{k=-\infty}^{\infty} (H_{int})_{n-k}|F(E)_k\rangle = E|F(E)_n\rangle, \tag{2.62}$$

where $n = 1, 2, 3, ...$ denotes the number of photons absorbed or emitted by the system. We can then write the above equation in a simpler form as a time-independent Schrödinger equation:

$$H_F|F(E)\rangle\rangle = E|F(E)\rangle\rangle, \tag{2.63}$$

where H_F is the Floquet Hamiltonian given by a matrix whose elements are time-independent operators, and $|F(E)\rangle\rangle$ are the Floquet vectors. Recall that we assumed that the laser field was monochromatic with frequency ω. We can therefore write our interaction Hamiltonian $H_{int}(t)$ in the form:

$$H_{int}(t) = H_+ e^{-i\omega t} + H_- e^{i\omega t}, \tag{2.64}$$

where H_+ and H_- are time-independent Hermitian operators. With this we can rewrite equation (2.62) in the form:

$$(H_o - n\omega)|F(E)_n\rangle + H_+|F(E)_{n-1}\rangle + H_-|F(E)_{n+1}\rangle = E|F(E)_n\rangle, \tag{2.65}$$

which tells us that the Floquet Hamiltonian will be of the form:

$$H_F = \begin{bmatrix} \ddots & & & & & \\ \cdots & H_+ & H_o - (n-1)\omega & H_- & 0 & \cdots \\ \cdots & 0 & H_+ & H_o - (n-1)\omega & H_- & 0 \\ & & & & & \ddots \end{bmatrix}. \tag{2.66}$$

This form of the Floquet Hamiltonian has a simple interpretation, the harmonic components $|F(E)_n\rangle$ describe the state that the system becomes upon exchanging n-photons with the applied laser field. We refer to these Floquet states as "dressed" states which are obtained via diagonalization. We apply this method to charge resonance enhanced ionization related to localization in chapter 5 of this thesis.

Chapter 3

Multi-electron Effects in High Harmonic Generation

3.1 High Harmonic Generation

High harmonic generation (HHG) is a phenomenon that has been observed and studied for several decades now. While many studies of HHG have been focused on atoms, it has been shown that HHG can in fact occur in molecules.

In this chapter, we will study the cases of laser induced resonant coupling in molecules which results in non-adiabatic electron dynamics that leads to Mollow sidebands appearing in HHG spectra. We consider the cases of a single linearly polarized laser pulse interacting with the system, as well as the case of multiple linearly and circularly polarized pulses interacting with a molecule. In addition, we study the cases where generated harmonics are elliptically polarized.

3.1.1 Motivation for High Harmonic Generation

The demand for efficient coherent light generation at high frequencies has been something scientists and engineers have pushed for since the maser was first invented. In particular, the generation of coherent light in the extreme-ultraviolet (EUV) to x-ray regime has been a problem for many years. An attractive and practical solution to this problem has been the generation of radiation by non-linear processes such as the interaction of ultra-short high-intensity pulses with atoms, which as a result generate high harmonics [19,20]. A particularly important application of HHG has been the generation of attosecond (1 attosecond = 10^{-18} seconds) pulses, which are important within the discipline of ultrafast AMO.

To motivate HHG further we consider a historical experiment performed by Leland Stanford and Eadweard Muybridge in 1872 [21]. Stanford asked the question if, at any point during a horses gallop, were all of its feet in the air. Unfortunately, the human eye was not enough to determine this. With the help of Muybridge, they arranged many threads along a race track, each connected to an individual camera which captured a photograph when the threads were pulled or broken. The horse proceeded to run along the track triggering each camera resulting in a series of pictures (see figure 3.1). The mystery was then solved and it was determined that by time resolving the horse's motion, that all its feet were indeed in the air at a given time within its gallop.

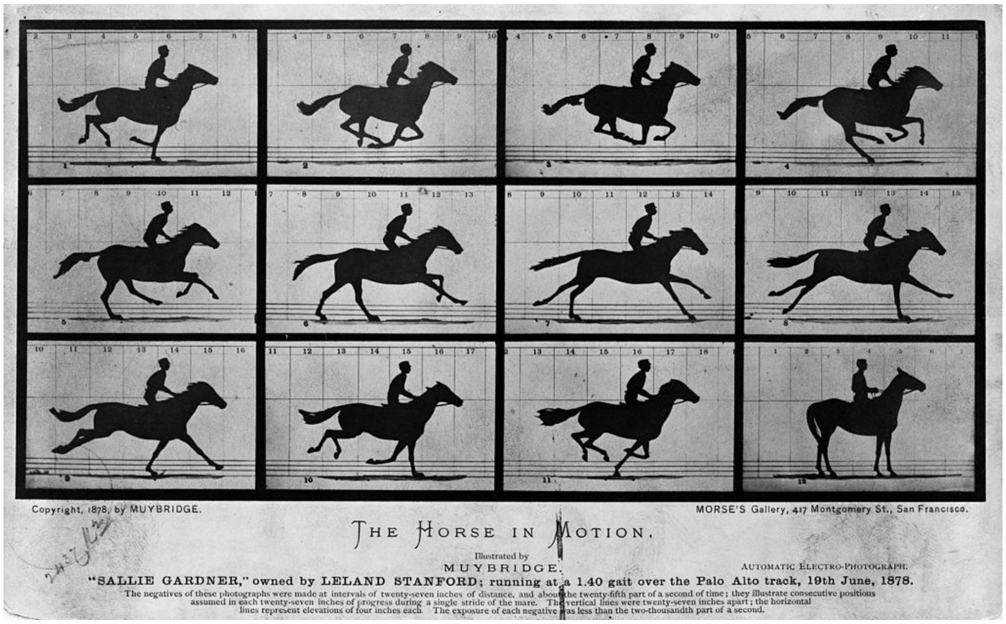

Figure 3.1: Eadweard Muybridge's The Horse in Motion, 1878. [19]

Similar to Stanford's and Muybridge's experiment, HHG can act as a camera which capture electron dynamics in atoms and molecules at their fundamental time scale, the attosecond. Hence, it is a powerful tool within AMO, and gives us further insight into the behavior of light matter interactions.

3.1.2 A Semi-Classical Description of High Harmonic Generation

The mechanism of HHG was first proposed by Corkum and others in 1993 [22, 23]. This model is referred to as the three step model. It gives a simple description of the dynamics involved in HHG. In step 1 of the model, the bound electron is ionized into the continuum by the applied field, which in this case is a laser pulse. In step 2, the electron is accelerated by the field, until in step 3 the switching of direction of the polarization of the field causes the electron to return and recombine with the parent ion, and a photon of energy equal to the energy of the recombined electron is emitted. There is a caveat in step 3 however, if the recollision of the ionized electron is inelastic then above-threshold ionization occurs, and HHG is suppressed. Figure 3.2 shows a diagram of the three-step model.

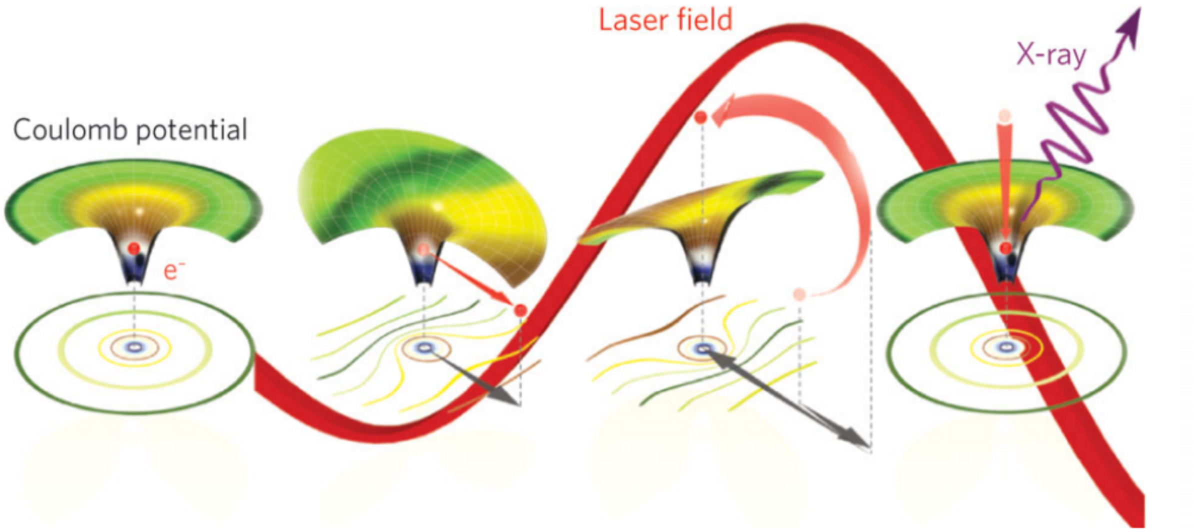

Figure 3.2: Diagram of the three-step model for high harmonic generation. Adapted from [46].

3.1.3 Features in High Harmonic Generation

High harmonic spectra are often calculated by taking the Fourier transform of the time-dependent dipole moment $\mathbf{d}(t)$, and then using the formula below:

$$P(\omega) = \frac{\alpha^3\omega^2}{3}\mathbf{d}(\omega) \cdot \mathbf{d}^*(\omega). \tag{3.1}$$

Such spectra have various notable features as can be seen in figure 3.3. The first regime of the spectra is regarded as the perturbative regime, which typically shows up to the 3^{rd}-5^{th} generated harmonics. Following is the plateau, where high-order harmonics are generated at similar intensities. Occurrence of this regime is a sign that there is a non-perturbative interaction between the electrons in an atom or a molecule and the applied laser field. There is then a cutoff following the plateau beyond which the intensity of the generated harmonics is greatly reduced.

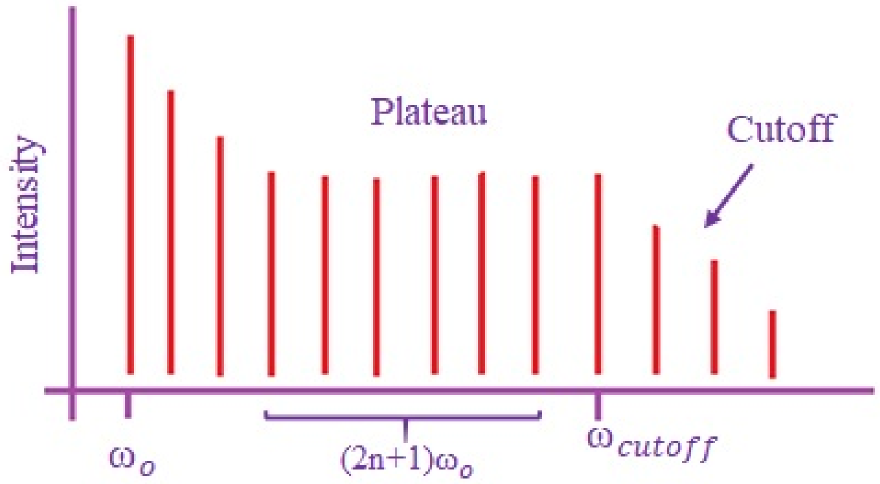

Figure 3.3: A schematic of a spectrum obtained from HHG due to the interaction of an atom or molecule with a linearly polarized laser.

The frequency at which the cutoff occurs can be determined using the following formula obtained from classical analysis:

$$\omega_{cutoff} = |I_p| + 3.17U_p, \tag{3.2}$$

where I_p is the ionization energy of the bound electron and U_p is the ponderomotive energy of an electron interacting with a laser, given by:

$$U_p = \frac{E_o^2}{4\omega^2}, \tag{3.3}$$

where e is the electron charge, E_o is the amplitude of the laser field, m is the mass of the electron, and ω is the frequency of the laser field.

It is typical for systems with inversion symmetry, i.e. systems with invariance under a point reflection, to exhibit only odd harmonics in their respective spectra, while under the influence of a linearly polarized pulse. It is worthwhile to mention that HHG spectra do not necessarily have the features shown in figure 3.3, modified properties of HHG can be seen when the polarization of the laser field or fields is not linear, but rather circular, as will be discussed later on in this chapter.

3.2 Molecular High Harmonic Generation

Harmonics generated from atoms with the interaction of linearly polarized pulses are linearly polarized as well. However, since molecular systems tend to be more complicated due to multielectron effects, their interaction with linearly polarized pulses is also more complex. An example of such complex interactions is that elliptically polarized harmonics can be generated. This is largely due to the non-spherical symmetry of molecular orbitals.

3.2.1 Ellipticity of Generated High-Harmonics

As described by the 3-step model, HHG is a result of tunnel ionization followed by acceleration of the wavepacket into the continuum and then recombination with the parent ion accompanied by the release of energy as a harmonic. It is expected that the polarization of these harmonics is the same as the polarization of the laser field. This is indeed the case for atoms due to their inversion symmetry. However, harmonic generation from molecules has two components, one parallel and another perpendicular to the polarization of the field. One would expect another component to be along the propagation direction of the field, however it cannot be phase-matched, thus it is neglected [24]. This further complicates the use of the 3-step model to describe HHG from molecules.

HHG generated from molecules can encode various properties of the molecule such as structural information [24], in particular if the molecule is aligned. Until recently, only the intensity of generated harmonics could be obtained as well. However, due to technological advances, the phase of generated harmonics can now be measured. As a result, it is now possible to experimentally determine elliptically polarized HHG emission from molecules interacting with a linearly polarized pulse. It is also worth mentioning that the widely used theory known as the strong-field approximation (SFA) fails to predict elliptical polarization of molecular harmonics correctly. However via the use of ab-initio methods such as TDDFT, ellipticity of HHG can be predicted properly.

Measuring the polarization of emitted harmonics is of particular interest for various reasons. Both the parallel and perpendicular components depend on the optical frequency ω and the angle θ of the molecule with respect to the field polarization. These components are directly related to the field induced dipole moment and have a ratio given by:

$$r = \frac{|d_{\perp}(\omega)|}{|d_{||}(\omega)|}, \tag{3.4}$$

which is independent of the angle-dependent ionization (see [24]). From there it is possible to determine the phase difference between the parallel and perpendicular components given by:

$$\delta = arg[d_{\perp}(\omega)] - arg[d_{||}(\omega)], \tag{3.5}$$

where this relative phase is not dependent on the intrinsic phase accumulated during the ionization and acceleration steps of the 3-step model because they are common for both the parallel and perpendicular components. While both r and δ are assumed to be independent of angle dependent ionization in SFA, we do not make this assumption within TDDFT and in our calculations. In the end, measuring the polarization of HHG should in theory allow us to investigate the ionization and recombination steps in the 3-step model in deeper detail and thus extend our knowledge of the mechanism of HHG in molecules.

By obtaining the HHG spectrum, we can then determine the ellipticity of a given harmonic within the spectrum with the following equation:

$$\epsilon = \sqrt{\frac{1 + r^2 - \sqrt{1 + 2r^2 cos(2\delta) + r^4}}{1 + r^2 + \sqrt{1 + 2r^2 cos(2\delta) + r^4}}}, \tag{3.6}$$

The ellipticity has a range of $0 \leq \epsilon \leq 1$, where 0 corresponds to linear polarization, and 1 to circular polarization and anything in between is considered elliptical polarization. From equation (3.6) we can see that the maximum ellipticity occurs when $r = 1$ and $\delta = 90^o$, which means that both the parallel and perpendicular components of the dipole moment must be of similar magnitude. However, as a result of the strong oscillation of the electron due to the laser, the perpendicular component tends to be smaller in magnitude than the parallel component, which is due to the shaking of the electron wavepacket happening in the parallel direction, so a larger time-dependent dipole moment component is expected.

3.2.2 Ensemble Alignment Averaging

In this thesis we investigated the appearance of elliptically polarized harmonics generated from the interaction of a linearly polarized laser and CO_2. It is typical in experiments that molecules are aligned using a laser pulse, which creates a rotational wave-packet that synchronizes the motion of molecules. Then at a certain time during the experiment the molecules are aligned, however not perfectly. The distribution of alignment is measured by doing rotational averaging.

Within our theoretical studies, we begin by solving the time-dependent Kohn-Sham equation (2.31) for our system to obtain the time-dependent dipole moments $\mathbf{d}(\mathrm{t})$. This is done for each orientation angle ranging from 0^o to 90^o. Then, in order to account for the distribution of alignment angles, as done in the experiment, the dipole moments are averaged using the same averaging technique, $\langle cos^2\theta \rangle$ [24,26].

If we consider the direction of the probe laser pulse to be along the z-direction and the pump laser field to lie in the xy-plane with a polar angle α, while orienting the molecule around the direction given by the vector $(sin\theta_m cos\phi_m, sin\theta_m sin\phi_m, cos\theta_m)$, as shown in figure 3.4, where θ is the intersection angle between the molecular axis and the pump laser field. As a result, the distribution of the alignment of the molecules with respect to the pump laser is a function of the intersection angle θ. We can then solve for this angle via:

$$cos\theta = sin\alpha sin\theta_m sin\phi_m + cos\alpha cos\theta_m. \tag{3.7}$$

We can then determine an angular distribution $\rho(\alpha, \theta_m, \phi_m)$ for the molecular axis at any given orientation angle given by (θ_m, ϕ_m) with respect to the pump-probe angle α. With that the averaged time dependent dipole is given by:

$$\langle d_{\parallel/\perp}(t, \alpha)\rangle = \int_0^{\pi}\int_0^{2\pi} d\theta_m d\phi_m d_{\parallel/\perp}(t, \theta_m, \phi_m)\rho(\alpha, \theta_m, \phi_m) sin\theta_m. \tag{3.8}$$

Considering to the symmetry of molecules, we only performed calculations in which the polar angle θ_m was varied from 0^o to 90^o as mentioned prior, while setting $\phi_m = 0$

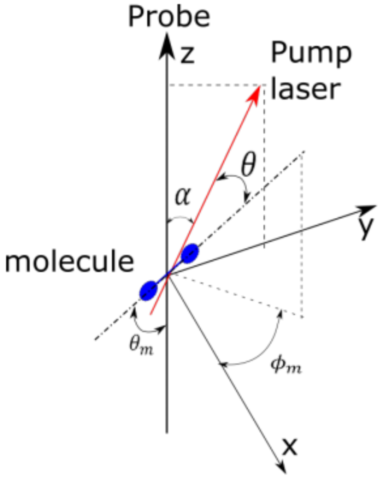

Figure 3.4: Diagram illustrating the method for angle averaging.

3.2.3 Ellipticity of Harmonics From CO_2

In experiments involving N_2 and CO_2 interacting with a linearly polarized laser field, ellipticity of harmonics was observed for N_2 but not for CO_2 [24,25]. However, other theories based on SFA which include multiple electronic continuum dynamics predict ellipticity of harmonics from CO_2 [24,25]. In other words, multi-electron effects in molecules can indeed lead to the production of elliptically polarized harmonics in CO_2.

We investigate the cases of CO_2 interacting with an 800 nm field of intensities (i) $1.5 \times 10^{14} \frac{W}{cm^2}$ and (ii) $2 \times 10^{14} \frac{W}{cm^2}$. The orientation angle of the molecule with respect to the laser polarization is varied from 0^o to 90^o with a step of 10^o. With the use of TDDFT we are able to calculate the responses of a set of occupied orbitals to the driving field. Figures 3.5a-b show ellipticity as a function of harmonic order for various orientation angles $\theta = 20^o$, $\theta = 40^o$, and $\theta = 80^o$ for both intensities discussed above. We can see that there is in fact elliptically polarized harmonic generation in CO_2, and for some harmonic orders the ellipticity is quite large ranging from values of 0.5 to 0.8, which contradicts the results found in experiments conducted in [24,25]. We investigate this further in the following sections by looking at the single orbital contributions to ellipticity.

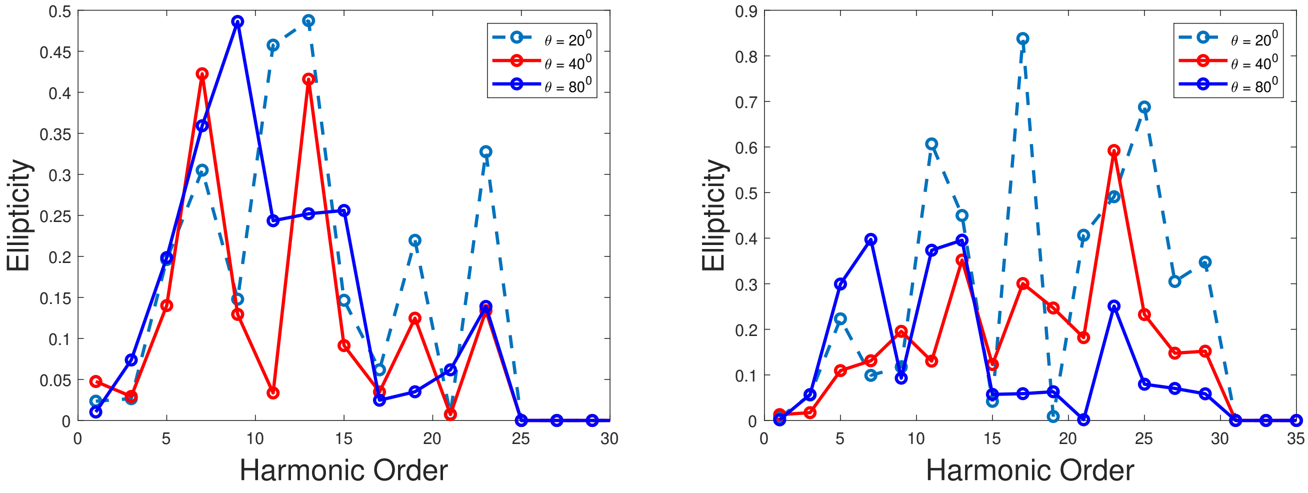

(a) (b)

Figure 3.5: Ellipticity as a function of harmonic order for CO_2 interacting with an 800 nm pulse at intensities (a) $I = 1.5 \times 10^{14} \frac{W}{cm^2}$ and (b) $I = 2 \times 10^{14} \frac{W}{cm^2}$. Various orientation angles are shown: $\theta = 20^o$, $\theta = 40^o$, and $\theta = 80^o$.

3.2.3.1 Orbital Contributions to Ellipticity of Harmonics

As mentioned, multi-electron effects in molecules play a role in the generation of elliptically polarized harmonics. To further analyze, we look at the individual orbital contributions to the generation of elliptical harmonics. We begin by looking at an intensity plot of the ellipticity for each orbital added step by step as a function of harmonic order and molecular alignment angle as shown in figure 3.6a-f. For the sake of understanding these contributions, we do not perform an ensemble average of the molecular alignment. From the figures we observe that each orbital is indeed influencing the generation of elliptically polarized harmonics. We observe that the ellipticity of harmonics is quite strong when we consider just the $1\pi_u$ orbital. However upon adding other orbital contributions the ellipticity becomes weaker largely due to interference.

Recall that HHG depends on ionization which in turn is dependent on the ionization potential and the alignment angle of the molecule. When the molecule is oriented at 0^o and 90^o the contribution to HHG from the $1\pi_g$ orbital is greatly suppressed due to quantum interference, thus ellipticity is nearly zero at these angles. However when the alignment angle is between 0^o and 90^o ellipticity of harmonics in non-zero. In contrast the σ_g and σ_u orbitals exhibit strong ellipticity when the alignment is near these angles.

Realistically and experimentally we do not have the means of observing ellipticity without ensemble averaging, or the ability to observe individual orbital contributions. As a result the actual ellipticity of generated harmonics will be quite weak as is observed in figure 3.7. Interestingly enough, when the intensity of the field is increased, ellipticity becomes more apparent, as can be seen in figure 3.9. This makes sense as the strength of the induced dipole is related to the strength of the field, thus the generation of harmonics will be increased

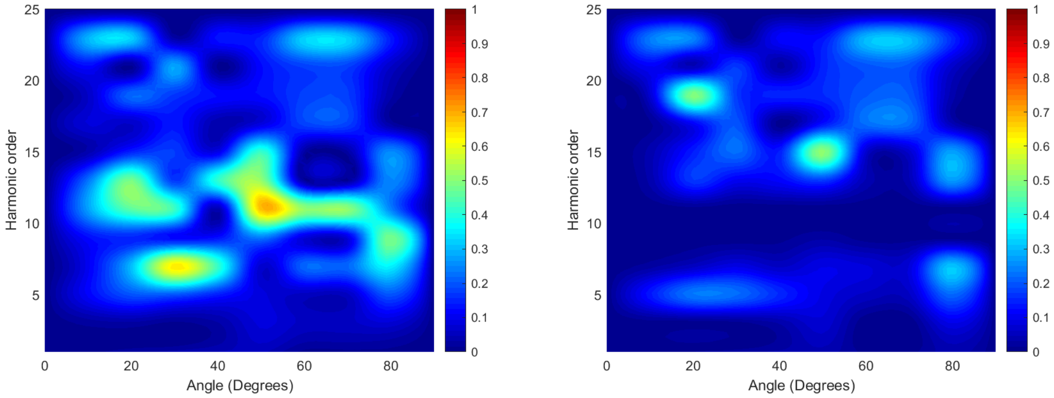

(a) $(3\sigma_g)^2(2\sigma_u)^2(4\sigma_g)^2(1\pi_u)^4(3\sigma_u)^2(1\pi_g)^4$ (b) $(2\sigma_u)^2(4\sigma_g)^2(1\pi_u)^4(3\sigma_u)^2(1\pi_g)^4$

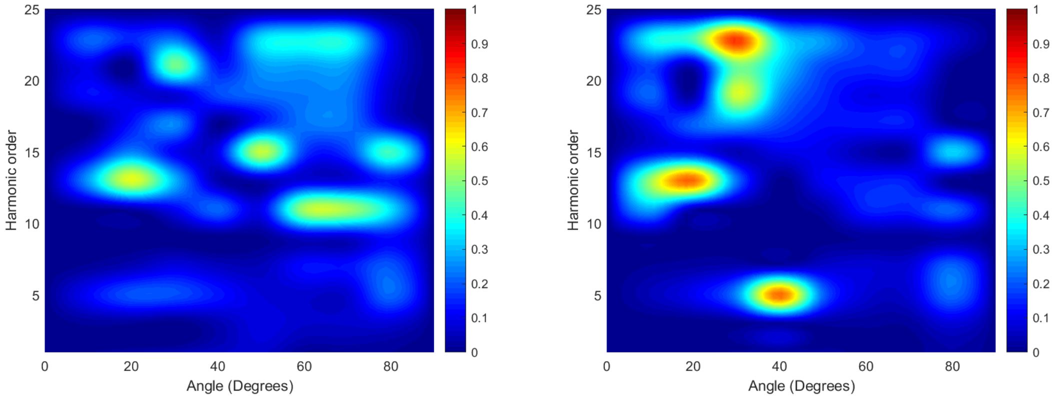

(c) $(4\sigma_g)^2(1\pi_u)^4(3\sigma_u)^2(1\pi_g)^4$ (d) $(1\pi_u)^4(3\sigma_u)^2(1\pi_g)^4$

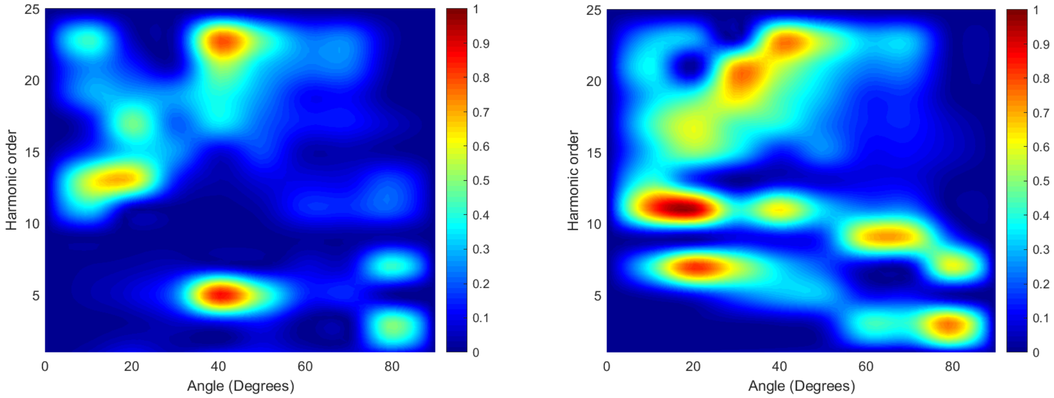

(e) $(3\sigma_u)^2(1\pi_g)^4$ (f) $(1\pi_g)^4$

Figure 3.6: Ellipticity of harmonics of CO_2 as a function of harmonic order and alignment angle for different orbital contributions added step by step. No ensemble average is made. The applied laser field is an 800 nm linearly polarized field with intensity $1.5 \times 10^{14} \frac{W}{cm^2}$.

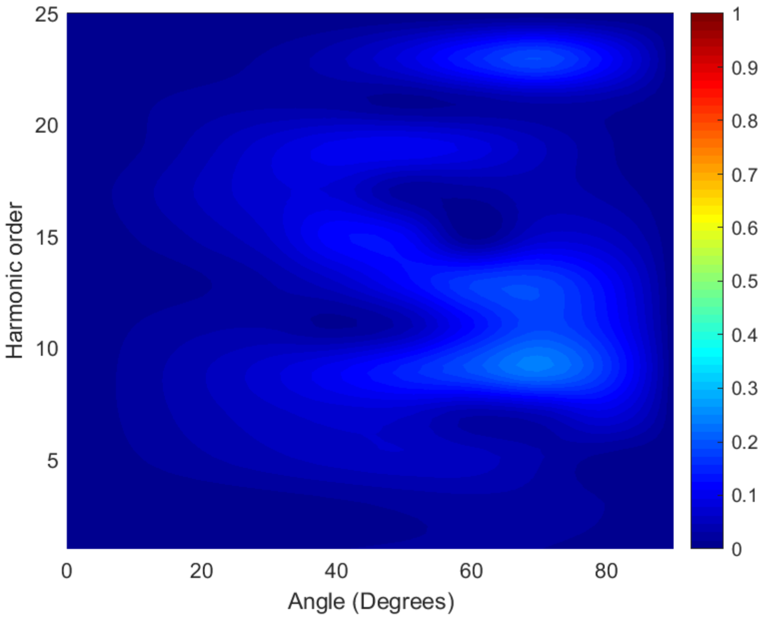

(a) $(3\sigma_g)^2(2\sigma_u)^2(4\sigma_g)^2(1\pi_u)^4(3\sigma_u)^2(1\pi_g)^4$

Figure 3.7: Ellipticity of harmonics of CO_2 as a function of harmonic order and alignment angle. Here an ensemble average is made. The applied laser field is an 800 nm linearly polarized field with intensity $1.5 \times 10^{14}\frac{W}{cm^2}$.

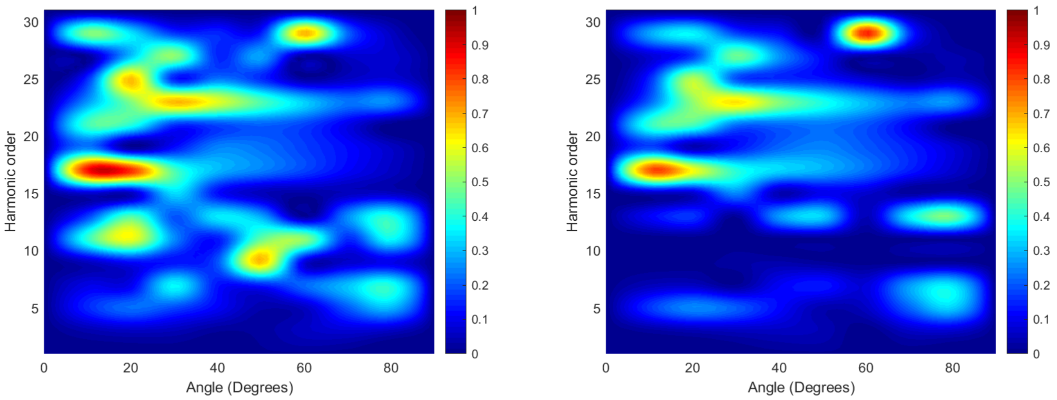

(a) $(3\sigma_g)^2(2\sigma_u)^2(4\sigma_g)^2(1\pi_u)^4(3\sigma_u)^2(1\pi_g)^4$ (b) $(2\sigma_u)^2(4\sigma_g)^2(1\pi_u)^4(3\sigma_u)^2(1\pi_g)^4$

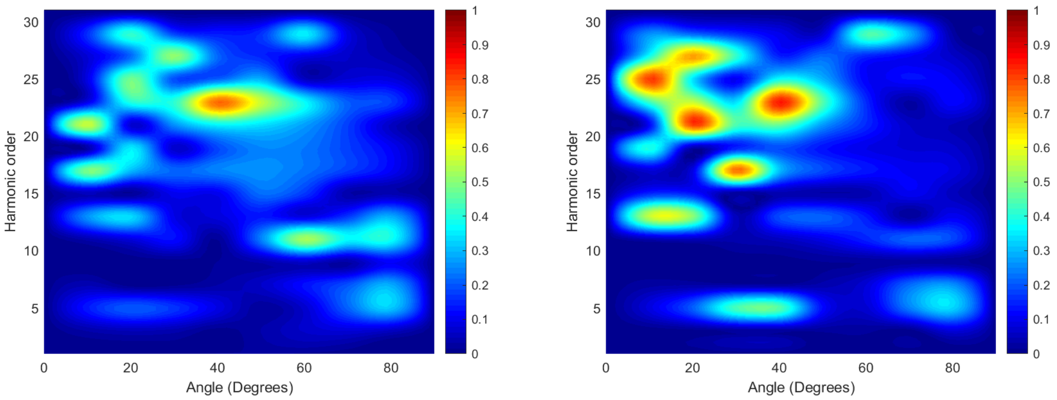

(c) $(4\sigma_g)^2(1\pi_u)^4(3\sigma_u)^2(1\pi_g)^4$ (d) $(1\pi_u)^4(3\sigma_u)^2(1\pi_g)^4$

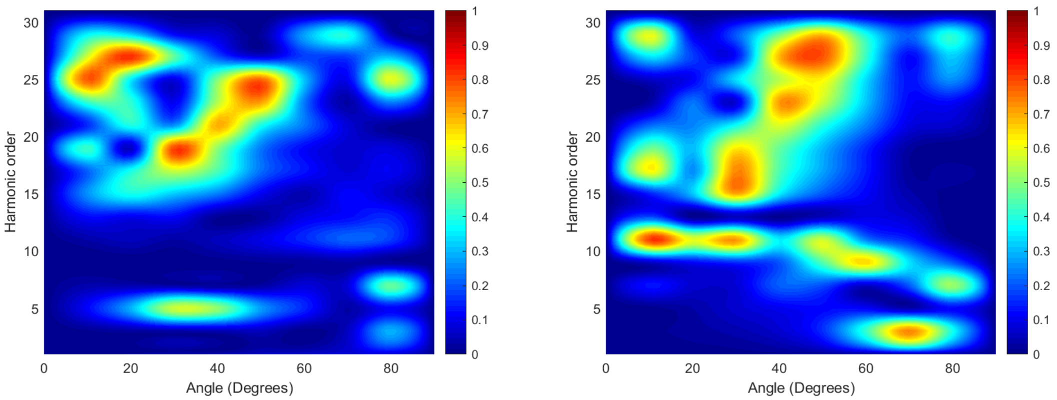

(e) $(3\sigma_u)^2(1\pi_g)^4$ (f) $(1\pi_g)^4$

Figure 3.8: Ellipticity of harmonics of CO_2 as a function of harmonic order and alignment angle for different orbital contributions added step by step. No ensemble average is made. The applied laser field is an 800 nm linearly polarized field with intensity $2 \times 10^{14} \frac{W}{cm^2}$.

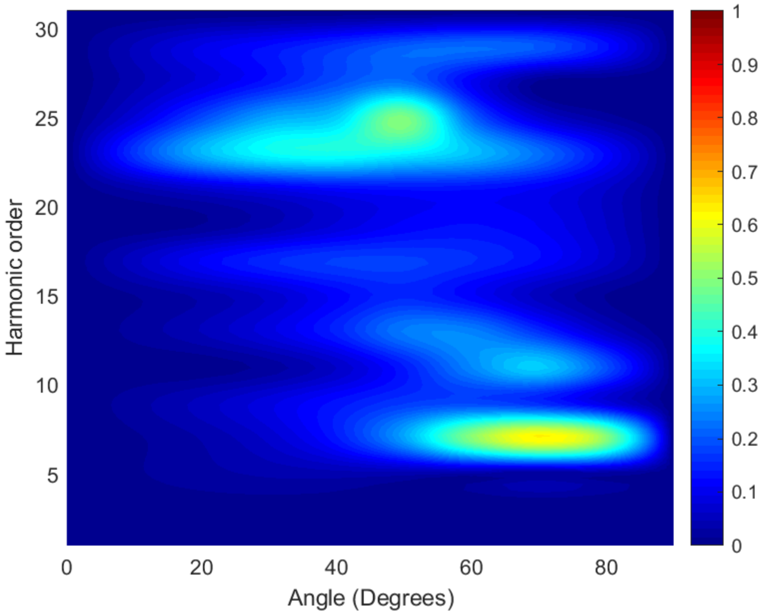

(a) $(3\sigma_g)^2(2\sigma_u)^2(4\sigma_g)^2(1\pi_u)^4(3\sigma_u)^2(1\pi_g)^4$

Figure 3.9: Ellipticity of harmonics of CO_2 as a function of harmonic order and alignment angle. Here an ensemble average is made. The applied laser field is an 800 nm linearly polarized field with intensity $2 \times 10^{14} \frac{W}{cm^2}$.

3.3 Mollow Sidebands

3.3.1 Adiabatic and Non-Adiabatic Behavior of Laser Induced Dipole Moments

There are several types of dynamics which can occur as a result of the interaction between molecules and laser pulses. One such type is regarded as adiabatic, meaning that the oscillation of the electron follows the oscillation of the electric field. Typically, this results in HHG spectra with the usual features as mentioned earlier in this chapter, at least for the case of linearly polarized pulses. The other type of dynamics which can occur is regarded as non-adiabatic, meaning that the electron does not follow the oscillation of the laser pulse. This can occur as a result of laser induced resonant couplings of orbitals. Typically this is done by setting the optical frequency of the laser pulse equal to the frequency between the orbitals. This type of dynamics gives rise to interesting phenomena that appears in HHG and electron localization, as we will see further in this thesis. Figures 3.10a-b respectively show adiabatic and non-adiabatic dipole behavior for N_2^+'s time-dependent dipole in the presence of an laser field for the cases of a 400 nm pulse with intensity $I = 2 \times 10^{14} \frac{W}{cm^2}$ and polarization (a) perpendicular to the molecular axis and (b) parallel to the molecular axis.

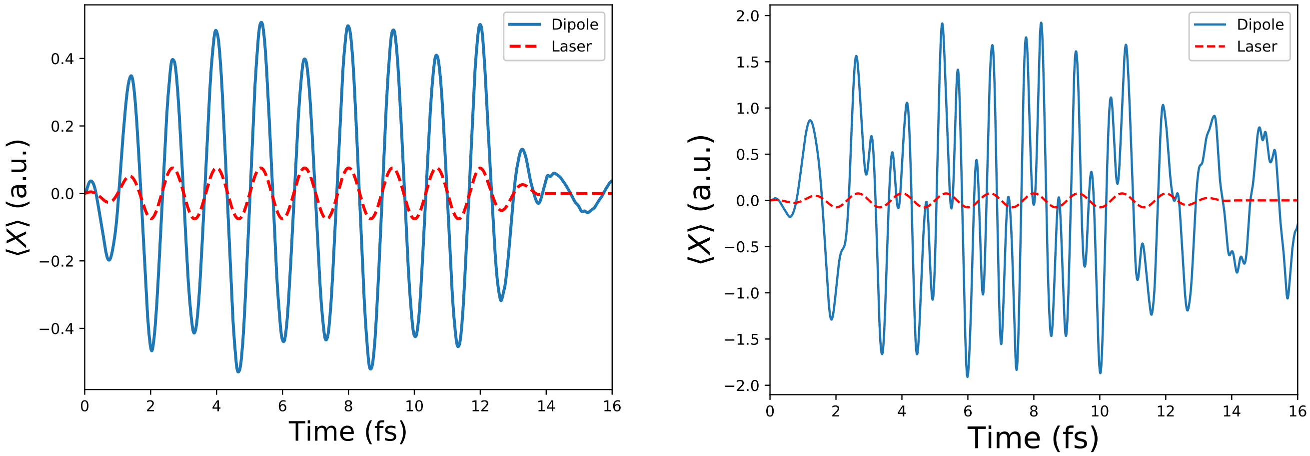

(a)

(b)

Figure 3.10: Time-dependent dipole moments of N_2^+ in the presence of a 400 nm laser field with intensity $I = 2 \times 10^{14} \frac{W}{cm^2}$. (a) Adiabatic behavior, and (b) Non-adiabatic behavior.

3.3.2 Open Shell Molecules

Within this thesis, non-adiabatic effects were studied for N_2^+ and $C_2H_4^+$, which are both open shell molecules, i.e. they contain valence shells which are not completely filled. In N_2^+ such effects happen in two cases studied. The first case is a linearly polarized laser of 400 nm with polarization oriented along the molecular axis. This case results in a laser induced resonant coupling between the $3\sigma_g$ and $2\sigma_u$ orbitals. The second case is an 800 nm linearly polarized pulse whose polarization is oriented perpendicular to the molecular axis, and for this case there is a laser induced resonant coupling between the $3\sigma_g$ and $1\pi_u$ orbitals. Figure 3.11 shows the molecular orbital diagram of N_2^+

along with the possible resonant couplings. Note, that we are able to specify in the TDDFT code OCTOPUS the orbital with the electron hole, thus making it the open-shell orbital.

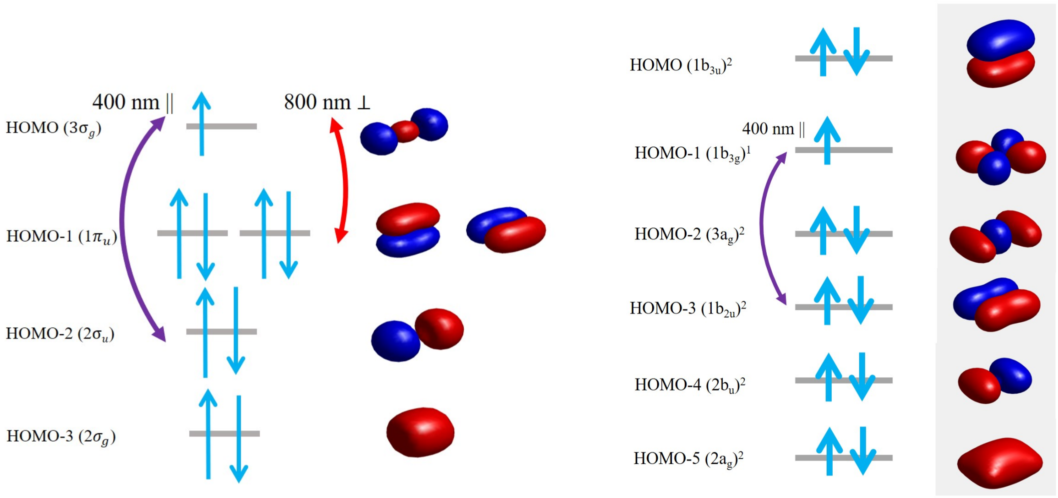

(a) (b)

Figure 3.11: Molecular orbital diagram of (a) N_2^+ and (b) $C_2H_4^+$. The purple arrow indicates a resonant coupling between the orbitals (a) $3\sigma_g$ and $2\sigma_u$ and (b) $1b_{3g}$ and $1b_{2u}$ induced by a 400 nm laser pulse with polarization parallel to the molecular axis, and the red arrow indicates a resonant coupling between the orbital $3\sigma_g$ and $1\pi_u$ induced by an 800 nm laser pulse with polarization perpendicular to the molecular axis.

While $C_2H_4^+$ is also an open shell molecule, it is far more complex than N_2^+. Still, it is worthwhile to investigate the non-adiabatic effects occurring due to a laser induced coupling of orbitals. Unlike N_2^+, where the open shell orbital is the highest occupied molecular orbital (HOMO), the open shell orbital in $C_2H_4^+$ is $1b_{3g}$, which is the HOMO-1, and a 400 nm linearly polarized laser pulse with polarization oriented parallel to the molecular axis induces a resonant coupling with the $1b_{2u}$ orbital (HOMO-3).

It is worthwhile to mention that we make a distinction between molecular orbitals and states in this thesis. While we talk about coupling orbitals, there is another picture that can give us insight into the dynamics occurring. We consider the ground state of N_2^+ labeled Σ_g and two excited states of N_2^+ labeled Π_u and Σ_u in figure 3.12, which have the respective electron configurations, $(2\sigma_g)^2(2\sigma_u)^2(1\pi_u)^4(3\sigma_g)^1$, $(2\sigma_g)^2(2\sigma_u)^2(1\pi_u)^3(3\sigma_g)^2$, and $(2\sigma_g)^2(2\sigma_u)^1(1\pi_u)^4(3\sigma_g)^2$. We make the distinction that the ground state is the lowest energy configuration, while the two latter are the higher energy configurations, hence the excited state. We can think as the orbital coupling of a superposition wavepacket of the ground and excited states during the interaction with the laser. However for the remainder of this thesis we will talk about coupling of orbitals and not the states.

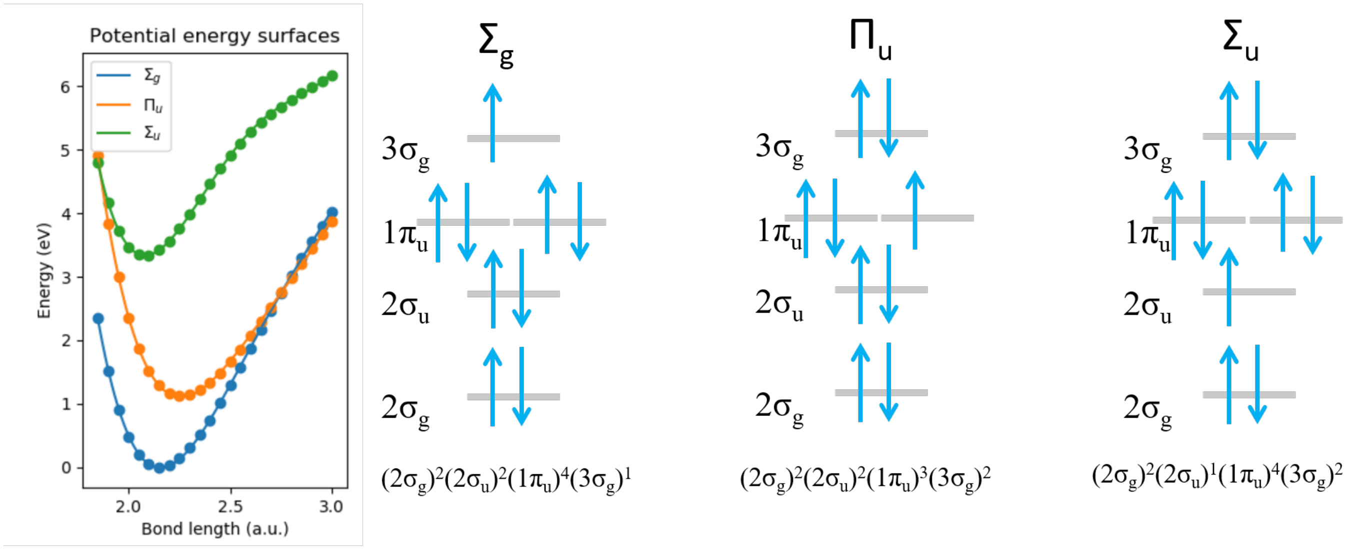

Figure 3.12: Potential energy surfaces of the ground state Σ_g and two excited states Π_u and Σ_u of N_2^+ and their respective diagrams showing the electron configuration for each state.

3.3.3 Appearance of Mollow Sidebands in High-Harmonic Generation

As a consequence of laser induced resonant coupling between orbitals, certain features appear in the respective HHG spectra of molecules. One of such features is the appearance of Mollow sidebands [43], which unlike regular harmonics they do not appear at integer multiples of the optical frequency of the laser field, but rather at a linear combination of the multiples of the laser frequency and the Rabi frequency which is given by:

$$\Omega_{Rabi} = \mu E_o, \tag{3.9}$$

where μ is the transition dipole moment between the orbitals, and E_o is the amplitude of the applied laser field. Figure 3.13 shows the respective HHG spectra for N_2^+ interacting with (a) a 400 nm laser with intensity $I = 5 \times 10^{14} \frac{W}{cm^2}$ with polarization parallel to the molecular axis and (b) an 800 nm laser with intensity $I = 2 \times 10^{14} \frac{W}{cm^2}$ polarized perpendicular to the molecular axis. As is evident from the figures, a laser induced resonance between orbitals causes additional features to appear in the HHG spectra in the form of the so-called Mollow sidebands. An interesting feature of these sidebands is that they are relatively similar in intensity to the odd harmonics. This can be attributed to the large transition dipole moment between orbitals as well as the strong coupling between the orbitals. We can identify the coupled orbitals by projecting the ground state orbital onto the excited state orbital during the simulation. The results show the population transfer between orbitals, and can be seen in figure 3.14. For the case of N_2^+ interacting with the 400 nm pulse polarized parallel to the molecular axis we can see that there is a strong coupling between the $3\sigma_g$ and $2\sigma_u$ orbitals, and that during the interaction with the laser there is a population transfer of about 80%. In contrast, for (b) the population transfer between $3\sigma_g$ and $1\pi_u$ is about 40%. We can therefore conclude that the appearance of Mollow sidebands is indeed caused by the laser induced coupling between the orbitals.

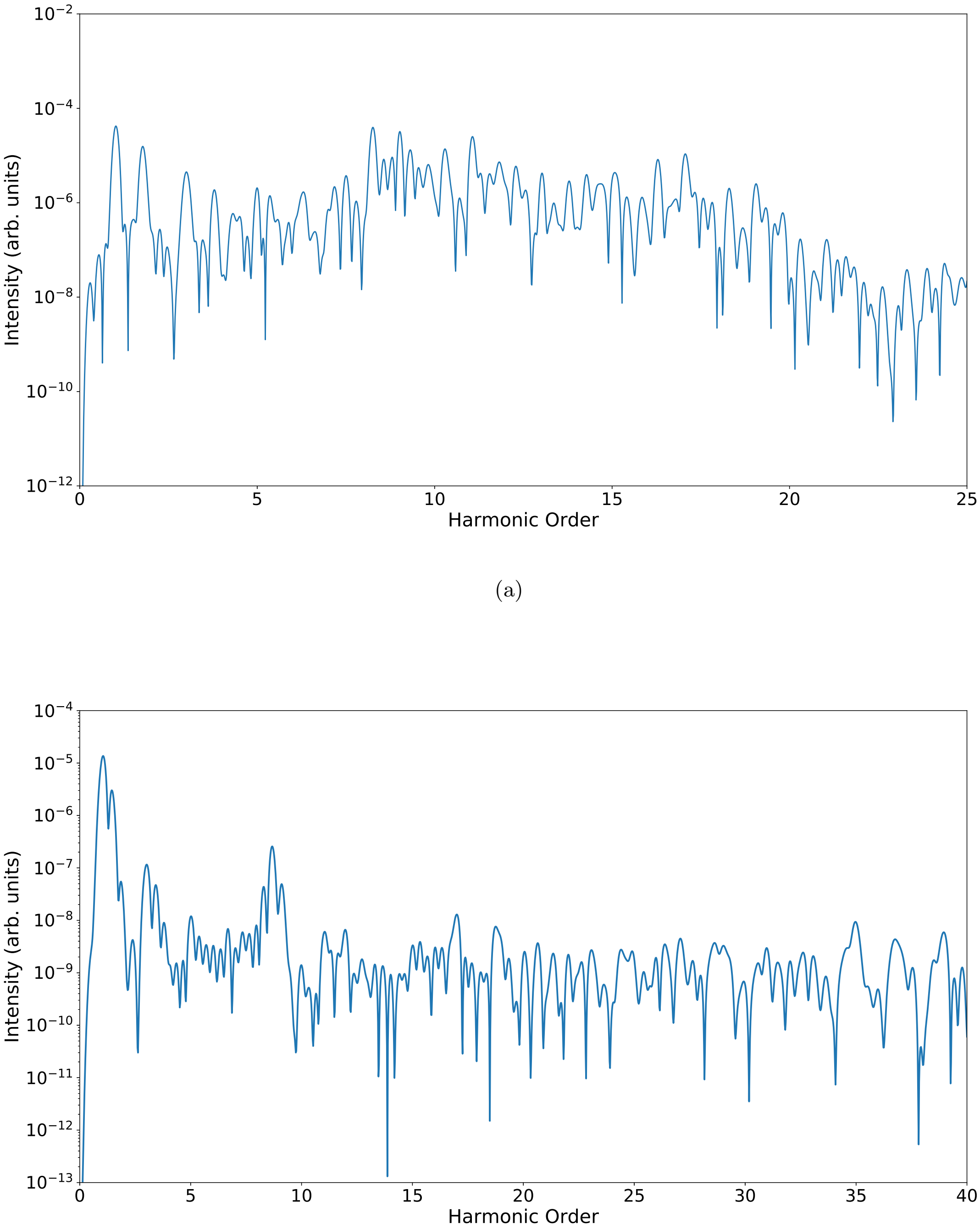

(a)

(b)

Figure 3.13: HHG spectra for N_2^+ interacting with (a) a 400 nm laser pulse of intensity $I = 5 \times 10^{14} \frac{W}{cm^2}$ with polarization parallel to the molecular axis, and (b) an 800 nm pulse of intensity $I = 2 \times 10^{14} \frac{W}{cm^2}$ with polarization perpendicular to the molecular axis. Note: figure (b) shows the spectrum before the frequency cutoff to make visualization of Mollow-sidebands easier to see.

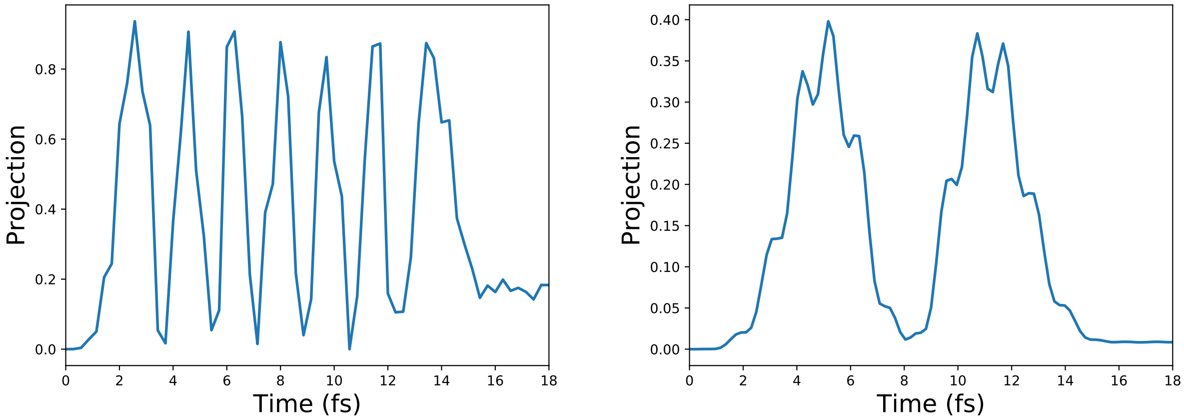

(a)

(b)

Figure 3.14: Time-dependent projections between coupled orbitals of N_2^+, for the cases of (a) coupling between $3\sigma_g$ and $2\sigma_u$ by a 400 nm pulse of intensity $I = 5 \times 10^{14} \frac{W}{cm^2}$ polarized parallel to the molecular axis, and (b) coupling between $3\sigma_g$ and $1\pi_u$ by an 800 nm pulse of intensity $I = 2 \times 10^{14} \frac{W}{cm^2}$ polarized perpendicular to the molecular axis.

It is worthwhile to mention, that due to the electron hole in the $3\sigma_g$ orbital of N_2^+, the appearance of Mollow sidebands in the ion is more prevalent than in the neutral counterpart N_2. This is largely attributed to the fact that the electron located in the $3\sigma_g$ must first be ionized in order for the electrons in inner shell orbitals to resonate between them, thus limiting the contribution to Mollow sidebands appearing in the spectra. However, if one begins with the ionic molecule, there is no need for the electron in the $3\sigma_g$ orbital to first be ionized which then allows for the electron in the coupled orbital to transition at a faster rate to the orbital where the electron hole is, thus making Mollow sidebands appear more prevalent in the HHG spectra. Figures 3.15a-b show the HHG spectra for N_2 interacting with (a) a 400 nm laser of intensity $I = 2 \times 10^{14} \frac{W}{cm^2}$ polarized along the molecular axis, and (b) an 800 nm laser of intensity $I = 2 \times 10^{14} \frac{W}{cm^2}$ polarized perpendicular to the molecular axis. We can see that for case (a) there appears to be some peaks forming next to the odd harmonics, albeit not of similar intensity as in N_2^+, while in case (b) there appear only odd harmonics with no trace of sidebands. This is largely due to the transition dipole moment being much larger in the case where one couples the $3\sigma_g$ and $2\sigma_u$ orbitals with a 400 nm pulse than when one couples the $3\sigma_g$ and $1\pi_u$ orbitals, and while the Mollow sidebands appear low in intensity, they are still noticeable for certain harmonic orders. Interestingly enough, the time-dependent projection between orbitals (see figures 3.16a-b), shows that there is indeed a strong population transfer between orbitals, in fact comparable to that of N_2^+ for the case of a 400 nm laser pulse polarized parallel to the molecular axis. However, for the case of an 800 nm pulse with perpendicular polarization, the population transfer is quite strong compared to the ionic counter part.

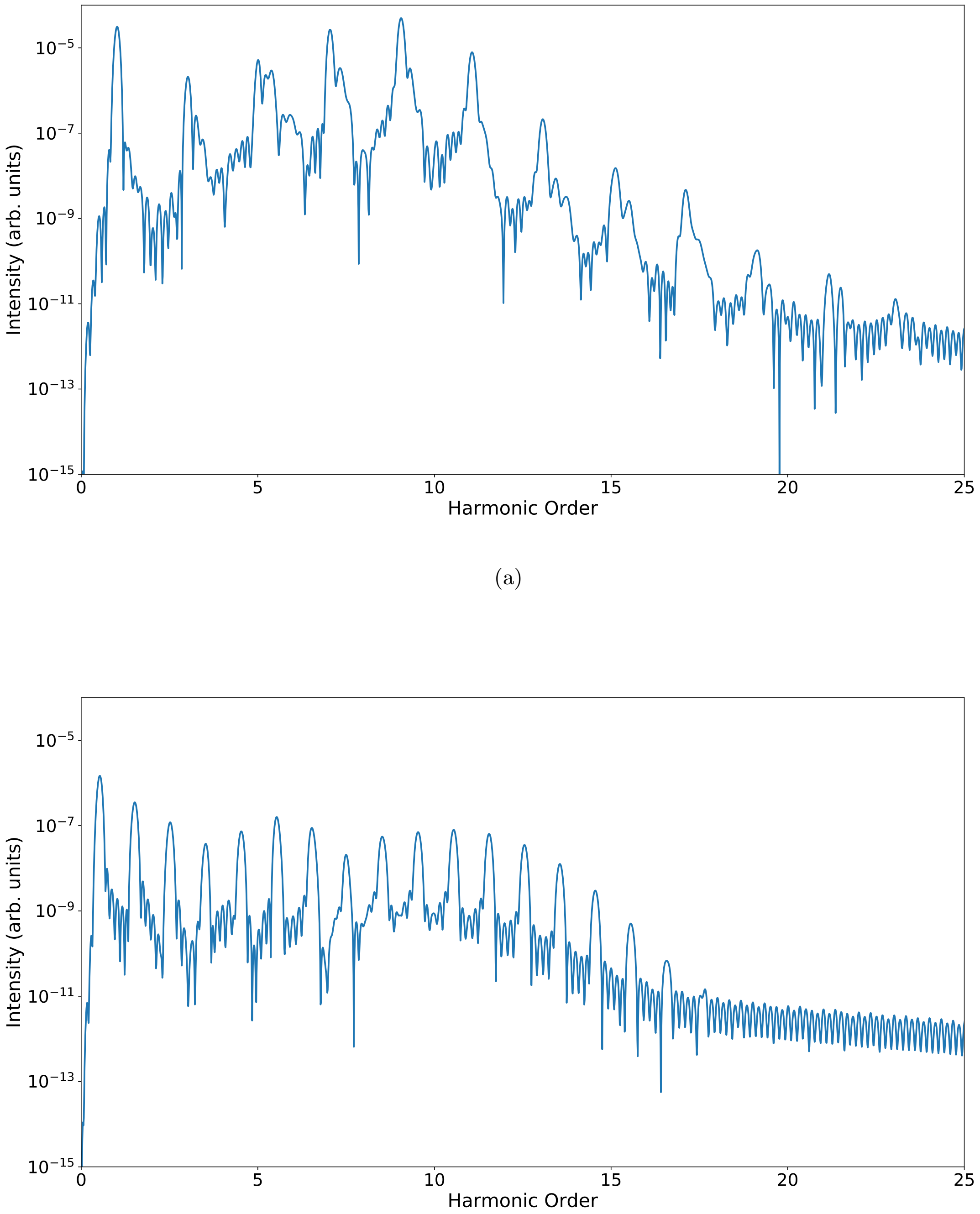

(a)

(b)

Figure 3.15: HHG spectra for N_2 interacting with (a) a 400 nm laser pulse of intensity $I = 2 \times 10^{14} \frac{W}{cm^2}$ with polarization parallel to the molecular axis, and (b) an 800 nm pulse of intensity $I = 2 \times 10^{14} \frac{W}{cm^2}$ with polarization perpendicular to the molecular axis.

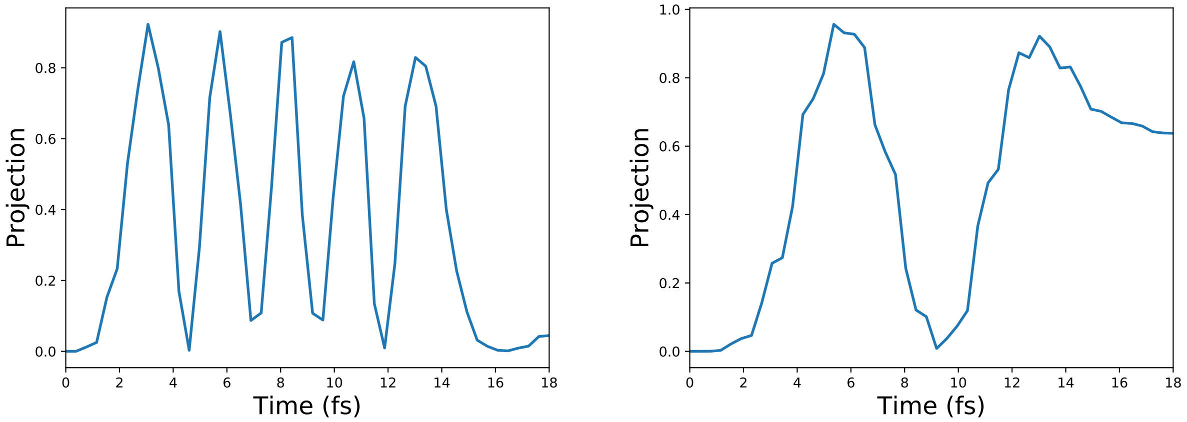

(a)

(b)

Figure 3.16: Time-dependent projections between coupled orbitals of N_2^+, for the cases of (a) coupling between $3\sigma_g$ and $2\sigma_u$ by a 400 nm pulse of intensity $I = 2 \times 10^{14} \frac{W}{cm^2}$ polarized parallel to the molecular axis, and (b) coupling between $3\sigma_g$ and $1\pi_u$ by an 800 nm pulse of intensity $I = 2 \times 10^{14} \frac{W}{cm^2}$ polarized perpendicular to the molecular axis.

3.3.4 High Harmonic Generation Dependence On Pulse Envelope

Up until now, every system we have considered has had the laser envelope be trapezoidal, figure 3.17a, i.e., a flat top pulse. Realistically speaking, such pulses cannot be realized at the femtosecond level, and mathematically the 'kink' that occurs after the ramp up brings about problems when considering the Fourier transform of the pulse. Despite that, they are useful when investigating HHG due to their continuous wave like properties, resulting in cleaner and smoother HHG spectra. Simply put, the electrons feel the peak intensity of the pulse for a majority of the interaction. Fortunately enough we are not limited to this pulse envelope when using TDDFT. In fact, we have complete freedom to choose what envelope we use throughout a simulation. We present the laser field obtained by using a $sin^2(.)$ envelope in figure 3.17c and from a first glance it is evident that the electrons in the system experience different intensities throughout the interaction, rather than a peak intensity for a longer period of time as in the trapezoidal case. Looking at the

Fourier transform of the $sin^2(.)$ envelope, figure 3.17d, also shows that the spectrum about the peak frequency, which in this case corresponds to $\lambda = 400$ nm, is broader when using the $sin^2(.)$ envelope rather than the trapezoidal one and as a result the HHG can vary greatly as shown in figure 3.18, where we present HHG for the case where $C_2H_4^+$ interacts with a 400 nm laser polarized parallel to the molecular axis and couples the $1b_{3g}$ and $1b_{2u}$ orbitals. We observe that when using the trapezoidal pulse the overlap between Mollow sidebands and the odd harmonics is such that the peaks are distinguishable, however when using the $sin^2(.)$ pulse the overlap between Mollow sidebands is increased so one cannot identify the structures caused by the laser coupling of orbitals. In the context of this thesis however, we are interested in distinguishing such features that arise from non-adiabatic behavior, so we will consider trapezoidal pulses for most of the results presented.

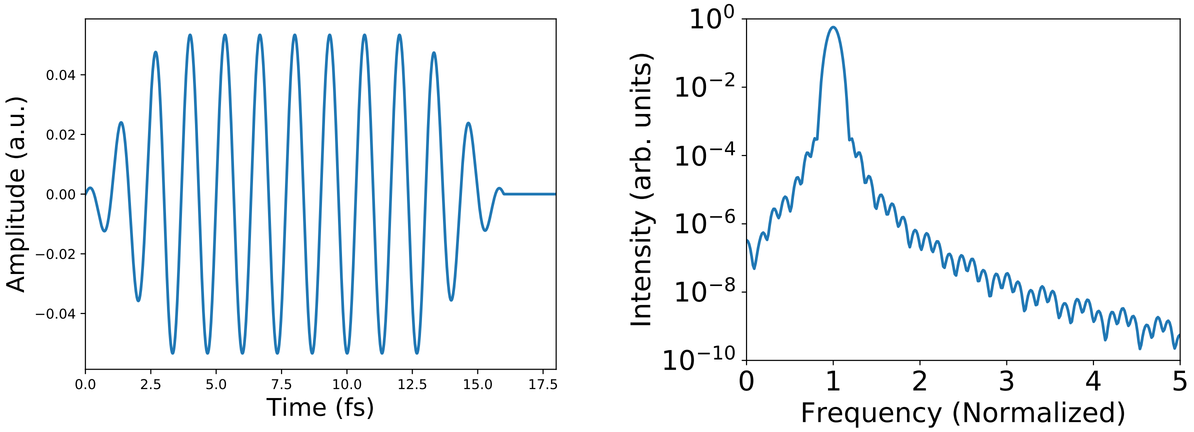

(a) Trapezoidal Envelope Time-Domain

(b) Trapezoidal Envelope Frequency-Domain

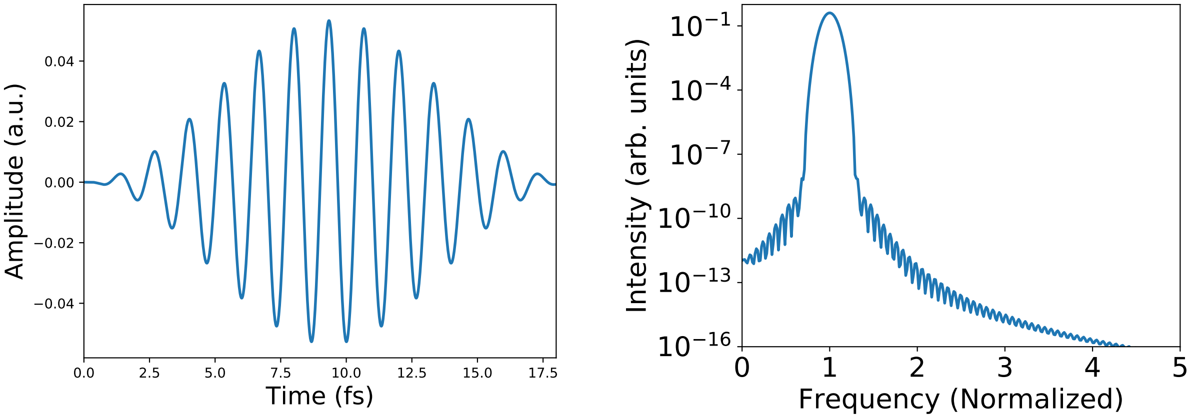

(c) sin^2 Envelope Time-Domain

(d) sin^2 Envelope Frequency-Domain

Figure 3.17: Plots of the laser fields with different pulse envelopes of wavelength $\lambda = 400$ nm in the time and frequency domains.

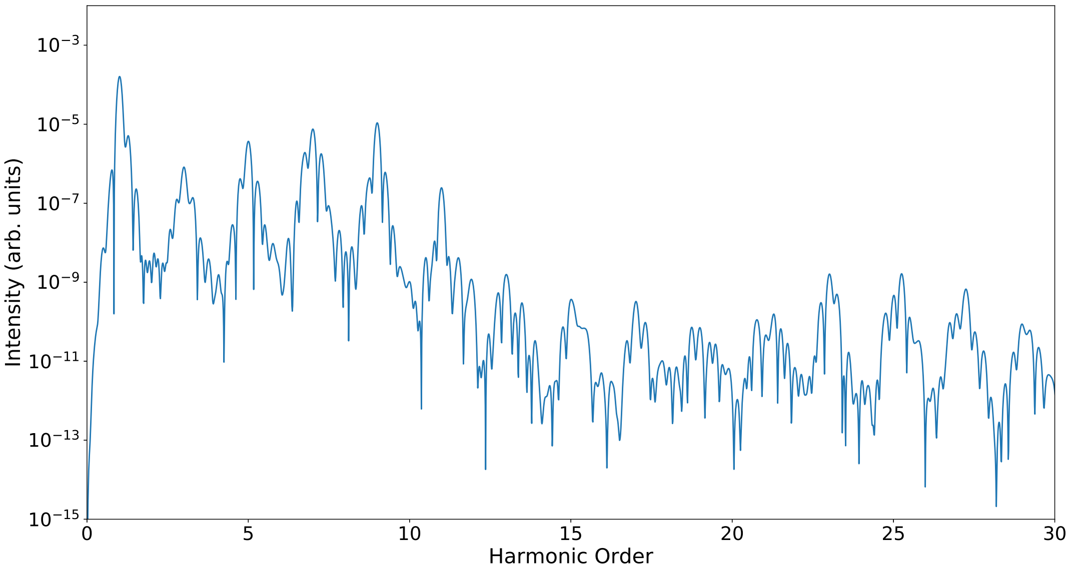

(a) Trapezoidal envelope.

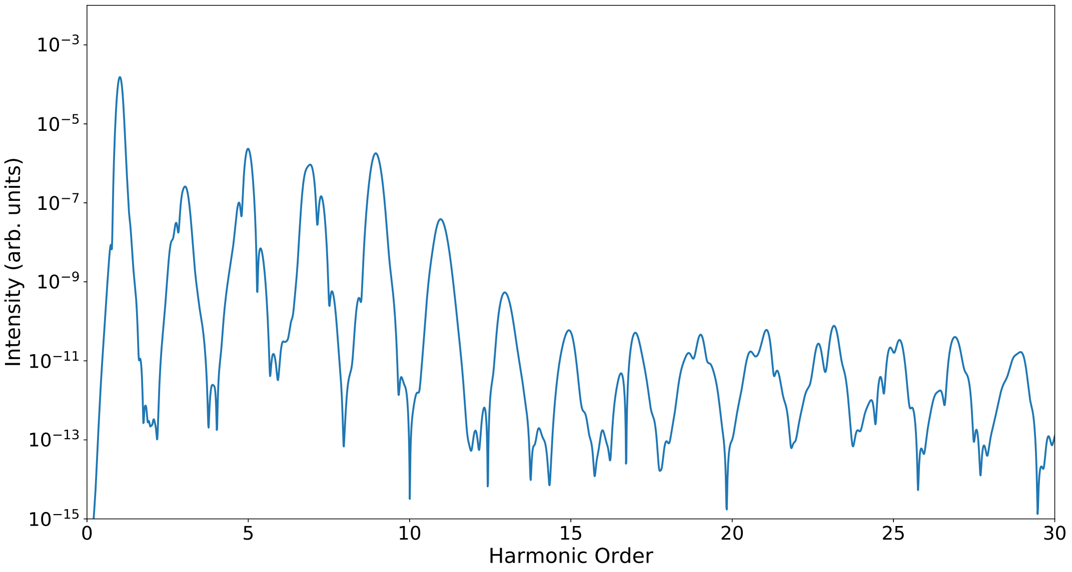

(b) sin^2 envelope.

Figure 3.18: HHG spectra for $C_2H_4^+$ interacting with a 400 nm pulse of peak intensity $I = 1 \times 10^{14} \frac{W}{cm^2}$.

3.3.5 Mollow Sidebands in Optical Bloch Equations

While the use of TDDFT allows us to capture full 3-dimensional multielectron dynamics in molecules interacting with a laser field and get a good quantitative and qualitative description of the features of HHG, it can computationally be quite time consuming. As a result we turn to other methods, which give us insight into what is occurring during HHG. One such way is based on optical Bloch equations, as described in chapter 2. While not as effective as TDDFT in capturing the full effects occurring in HHG, it paints a simple picture of the effect related to the appearance of Mollow sidebands in HHG.

We begin by considering the wavefunction of a two-level system given by a superposition state:

$$|\psi(t)\rangle = a_1(t)|\psi_1\rangle + a_2(t)|\psi_2\rangle, \tag{3.10}$$

where $a_1(t)$ and $a_2(t)$ are determined by solving the system of equations obtained from the TDSE, given by: (assuming that $\langle\psi_1|\psi_2\rangle = 0$)

$$i\dot{a}_1(t) = -\frac{\omega_o}{2}a_1(t) + V(t)a_2(t), \tag{3.11}$$

$$i\dot{a}_1(t) = \frac{\omega_o}{2}a_2(t) + V(t)a_1(t), \tag{3.12}$$

where ω_o is the frequency corresponding to the energy difference between states, $V(t) = \mu E(t)$, and μ is the transition dipole moment between states. The optical Bloch equations are for this case defined as equations for x(t), y(t), and z(t):

$$x(t) = a_1 a_2^* + a_2 a_1^*, \tag{3.13}$$

$$y(t) = i(a_2 a_1^* - a_1 a_2^*), \tag{3.14}$$

$$z(t) = |a_1|^2 - |a_2|^2, \tag{3.15}$$

which upon combination with the equations for the coefficients a_1 and a_2 lead to the following equations:

$$\dot{x}(t) = -\omega_o y(t), \tag{3.16}$$

$$\dot{y}(t) = \omega_o x(t) + 2V(t)z(t), \tag{3.17}$$

$$\dot{z}(t) = -2V(t)y(t). \tag{3.18}$$

Solving the set of equations gives us the induced dipole moment $d(t) = \mu x(t)$ and the population inversion $z(t)$.

Previous studies conducted by Bandrauk have shown that symmetric molecular ions have charge resonant states that are coupled by a laser field with optical frequency equal to the energy difference between the orbitals. However depending on wavelength and potential energy surface, it is also possible to couple orbitals when the internuclear distance R is enlarged. Such is the case for H_2^+, as shown by Bandrauk and Zuo [27,28], where they created charge resonant (CR) pairs from the superposition of the $1\sigma_u$ and $1\sigma_g$ orbitals. They considered three different excitation regions where the CR pairs could be created: (1) small R corresponding to multiphoton excitation, (2) intermediate R which is near resonant excitation, and (3) large R corresponding to the strong coupling regime.

We consider similar conditions to those considered by Bandrauk and show that such simple models like the optical Bloch equations do in fact predict Mollow sidebands. We consider the three following cases of H_2^+ interacting with a continuous wave laser of the form $E(t) = E_o cos(\omega t)$: (1) $R = 2.12$ a.u. with laser parameters $\lambda = 1064$ nm, $I = 10^{14}\frac{W}{cm^2}$, (2) $R = 5$ a.u. with $\lambda = 1064$ nm at $I = 4 \times 10^{13}\frac{W}{cm^2}$ and (3) $R = 10$ a.u. with $\lambda = 1064$ nm and $I = 10^{13}\frac{W}{cm^2}$. The HHG spectra corresponding to these cases are shown in figures 3.19a-c, respectively. In each of the HHG spectra we can see that Mollow sidebands are indeed appearing, though their intensities vary depending on the internuclear distance of H_2^+ and also each of the three coupling regimes we considered.

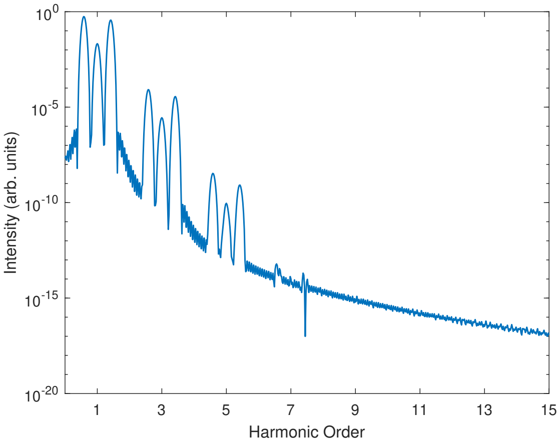

(a) $R = 2.12$ a.u.

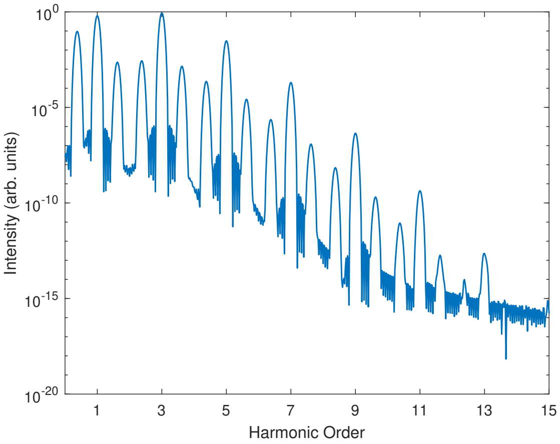

(b) $R = 5$ a.u.

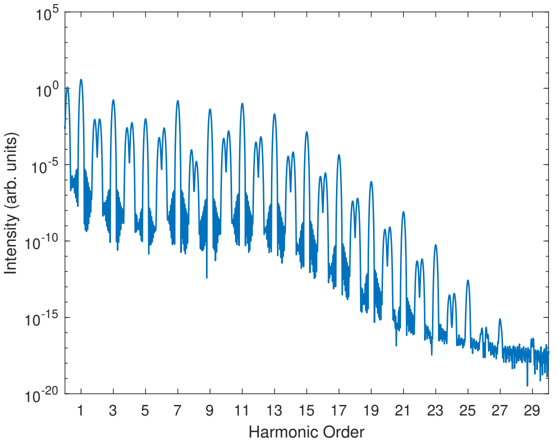

(c) $R = 10$ a.u.

Figure 3.19: HHG spectra for H_2^+ obtained via the optical Bloch equations. Three cases are shown: (a) $R = 2.12$ a.u. with laser parameters $\lambda = 1064$ nm, $I = 10^{14}\frac{W}{cm^2}$, (b) $R = 5$ a.u. with $\lambda = 1064$ nm at $I = 4 \times 10^{13}\frac{W}{cm^2}$ and (c) $R = 10$ a.u. with $\lambda = 1064$ nm and $I = 10^{13}\frac{W}{cm^2}$.

While we do observe Mollow sidebands in the HHG of H_2^+ for different internuclear distances we must consider that this system is quite simple compared to the others we have been investigating in this thesis so the question we now ask is if the optical Bloch equations can indeed predict Mollow sidebands in multielectron molecules such as N_2^+.

We begin by considering the case were we couple $3\sigma_g$ and $2\sigma_u$ with a 400 nm laser pulse. We utilize the transition dipole moment $\mu = 1.558 a.u$ obtained from TDDFT calculations, and obtain the respective HHG from cases where we vary the intensity from $I = 1 \times 10^{13} \frac{W}{cm^2}$ to $I = 5 \times 10^{15} \frac{W}{cm^2}$. The HHG spectra are shown in figure 3.20a-f. At the lowest intensity we observe odd harmonics ranging from order 0 to 5 with small peaks forming on the left and right side of each odd harmonic. These are indeed Mollow sidebands caused by the coupling of orbitals. As the intensity is increased the overlap between odd harmonics and Mollow sidebands decreases which is expected due to the Rabi frequency being directly proportional to the field strength. Another noticeable feature is that the harmonic order increases as the intensity is raised, however due to the perturbative nature of the optical Bloch equations, the cutoff is not where one would expect it.

The second case considered is when an 800 nm pulse couples the $3\sigma_g$ and $1\pi_u$ orbitals. Figure 3.21a-f shows the HHG spectra with intensities once again varying from $I = 1 \times 10^{13} \frac{W}{cm^2}$ to $I = 5 \times 10^{15} \frac{W}{cm^2}$. We again observe odd harmonics as well as Mollow sidebands whose overlap increases as the intensity is raised. However, unlike the full 3-dimensional calculations, the cutoff appears to occur at low harmonic orders. This is due to the fact that the continuum is not considered in optical Bloch equations, hence there is no acceleration acceleration and recombination of the ionized wave-packet resulting in a cutoff at higher orders.

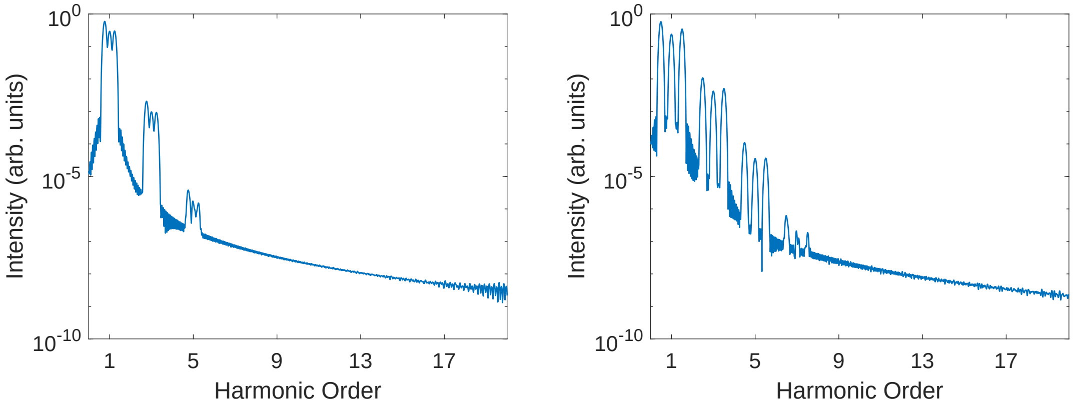

(a) $I = 1 \times 10^{13} \frac{W}{cm^2}$

(b) $I = 5 \times 10^{13} \frac{W}{cm^2}$

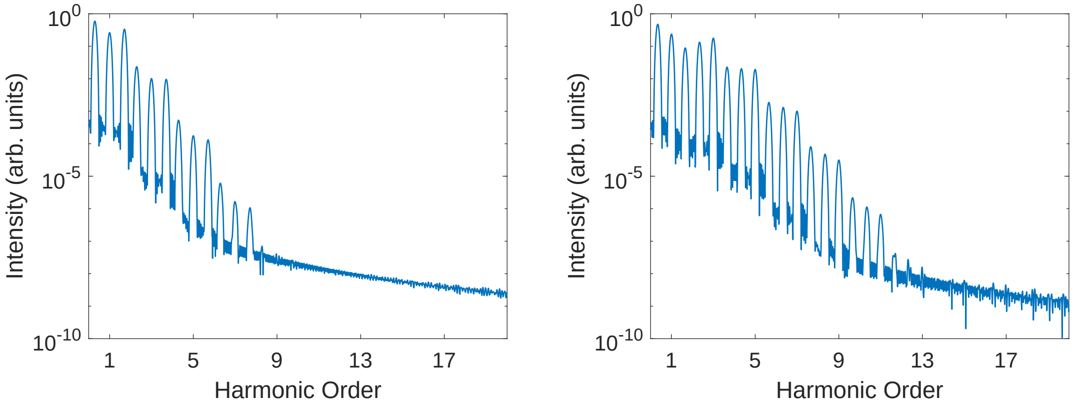

(c) $I = 1 \times 10^{14} \frac{W}{cm^2}$

(d) $I = 5 \times 10^{14} \frac{W}{cm^2}$

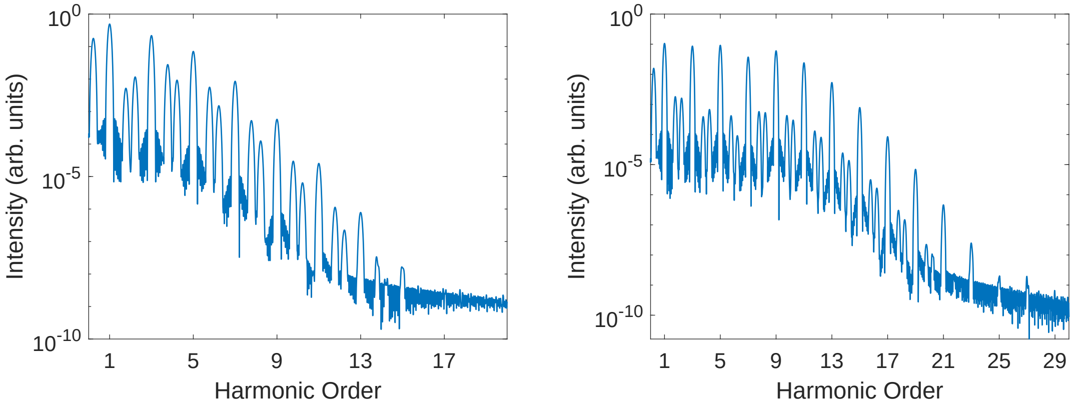

(e) $I = 1 \times 10^{15} \frac{W}{cm^2}$

(f) $I = 5 \times 10^{15} \frac{W}{cm^2}$

Figure 3.20: HHG spectra for N_2^+ obtained via the optical Bloch equations. The laser pulse has a wavelength of 400 nm and the intensity of the pulse is increased for each panel.

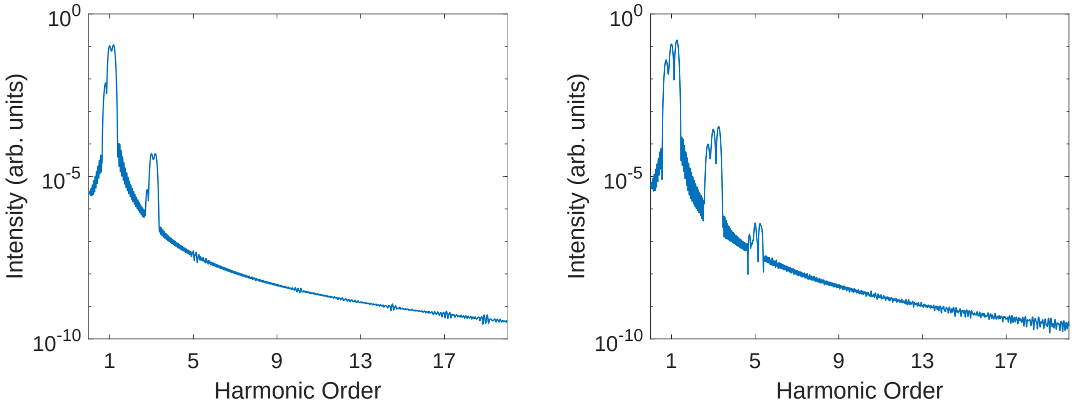

(a) $I = 1 \times 10^{13}\frac{W}{cm^2}$ (b) $I = 5 \times 10^{13}\frac{W}{cm^2}$

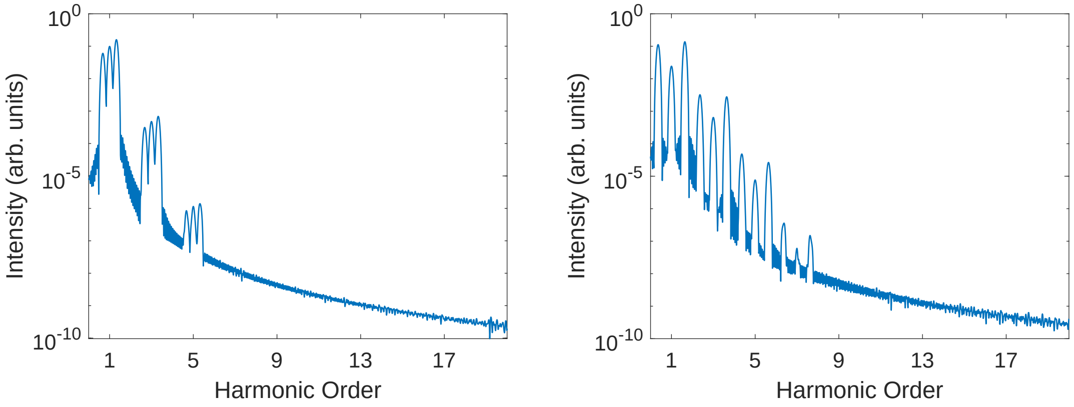

(c) $I = 1 \times 10^{14}\frac{W}{cm^2}$ (d) $I = 5 \times 10^{14}\frac{W}{cm^2}$

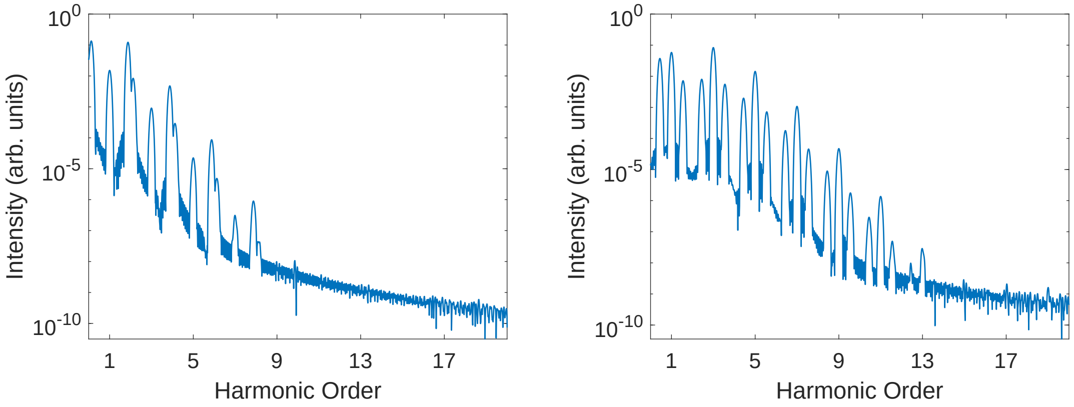

(e) $I = 1 \times 10^{15}\frac{W}{cm^2}$ (f) $I = 5 \times 10^{15}\frac{W}{cm^2}$

Figure 3.21: HHG spectra for N_2^+ obtained via the optical Bloch equations. The laser pulse has a wavelength of 800 nm and the intensity of the pulse is increased for each panel.

3.3.6 Comparison Between Theoretical Methods in the Appearance of Mollow Sidebands

The appearance of Mollow sidebands is clearly seen in HHG spectra obtained from both TDDFT and optical Bloch equations, however many differences arise when comparing both. When performing the full 3-dimensional calculation via TDDFT one is considering multi-electron effects as well as the electrons being ionized into the continuum and then recombining with the parent ion, which gives rise to an extension of harmonics to higher orders of frequency, whereas in optical Bloch equations the continuum is not included, thus the cutoff for harmonic generation occurs at lower frequencies than that obtained in TDDFT.

In addition, HHG spectra obtained from optical Bloch equations appear to be cleaner and so it is easier to distinguish Mollow sidebands from the odd harmonics. In TDDFT multielectron effects give rise to many interferences and overlaps between harmonics so obtaining a cleaner HHG spectra is sometimes more difficult.

For example, problems can arise when using TDDFT to model Rabi oscillations, as is the case in laser induced orbital coupling. When one utilizes adiabatic functionals the potential energy surfaces will change as the electron density changes, and so the system will be driven out of resonance. In other words, Rabi oscillations cannot be fully captured when using the adiabatic approximation as the instantaneous dependence of the state brings about a time-dependent detuning.

We look at the predicted versus measured Rabi frequencies given by the following equation:

$$\Omega_{Mollow} = n\omega \pm \Omega_{rabi}. \tag{3.19}$$

where $n\omega$ is the $n-th$ odd harmonic in the corresponding HHG spectra, and the second term is the Rabi frequency. Figures 3.22a-d show the comparisons for both the optical Bloch equations and TDDFT. We see that for both theories the measured frequencies agree with what is predicted with the given equation above. In conclusion we see that both theories do in fact capture the effects of the Rabi oscillations occurring as a result of the laser induced coupling between orbitals.

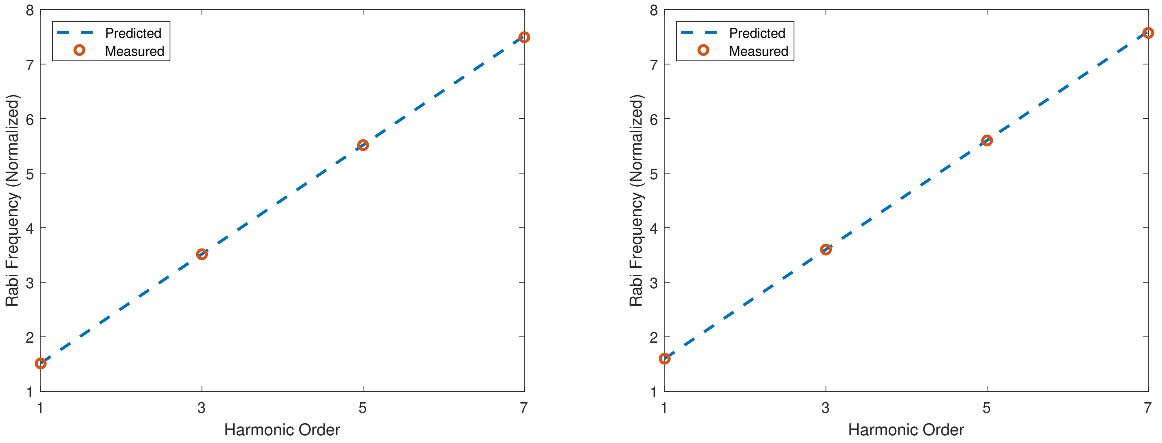

(a) Optical Bloch 400 nm

(b) Optical Bloch 800 nm

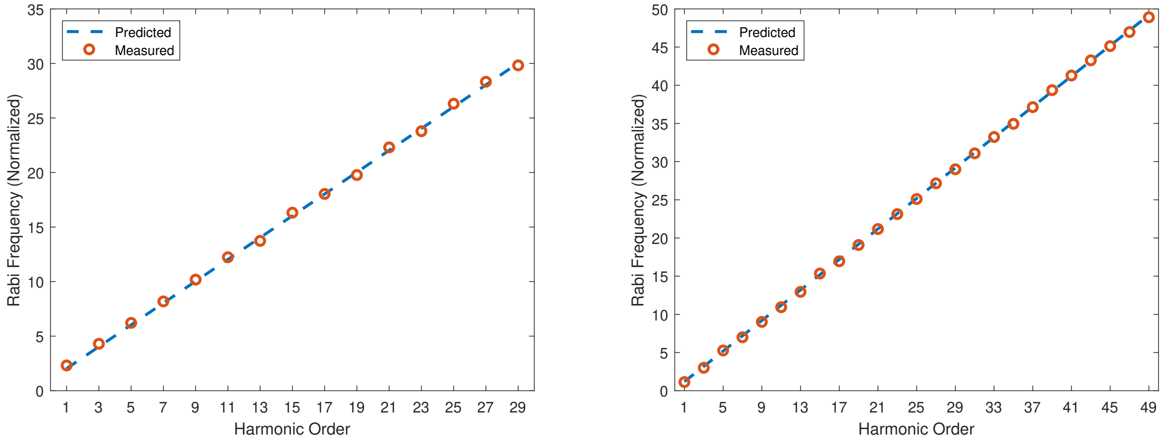

(c) TDDFT 400 nm

(d) TDDFT 800 nm

Figure 3.22: Predicted (blue dashed line) vs. Numerically obtained (red circles) frequencies of Mollow sidebands appearing in HHG spectra obtained from optical Bloch equations (panels a and b) and TDDFT (panels c and d) for the cases were the laser wavelength is 400 nm and 800 nm.

3.3.7 Time-Frequency Analysis of High-Harmonic Generation.

When we obtain HHG spectra by performing a Fourier transform of the time-dependent dipole moment we lose all information in the time-domain, per the Heisenberg uncertainty principle. Fortunately, there exist a tool by which we are able to examine how HHG changes with time known as time-frequency analysis, or wavelet analysis. The time-frequency spectra is obtained using the transform equation below:

$$\mathbf{d}(\omega, t) = \int \mathbf{d}(t) exp(-(t-\tau)^2/2\sigma^2) exp(-i\omega\tau) dt, \tag{3.20}$$

where the Gaussian function is a time window which constraints the FFT of the dipole to be applied only in the size defined by the function.

We begin by looking at a nonresonant case of N_2^+ interacting with a 400 nm laser pulse of intensity $I = 2 \times 10^{14} \frac{W}{cm^2}$ with polarization direction oriented perpendicular to the molecular axis, which does not induce a resonance between orbitals. The corresponding wavelet spectrum is shown in figures 3.23a-b , where (a) shows the total spectrum and (b) shows the spectrum zoomed in from 5 to 10 femtoseconds.

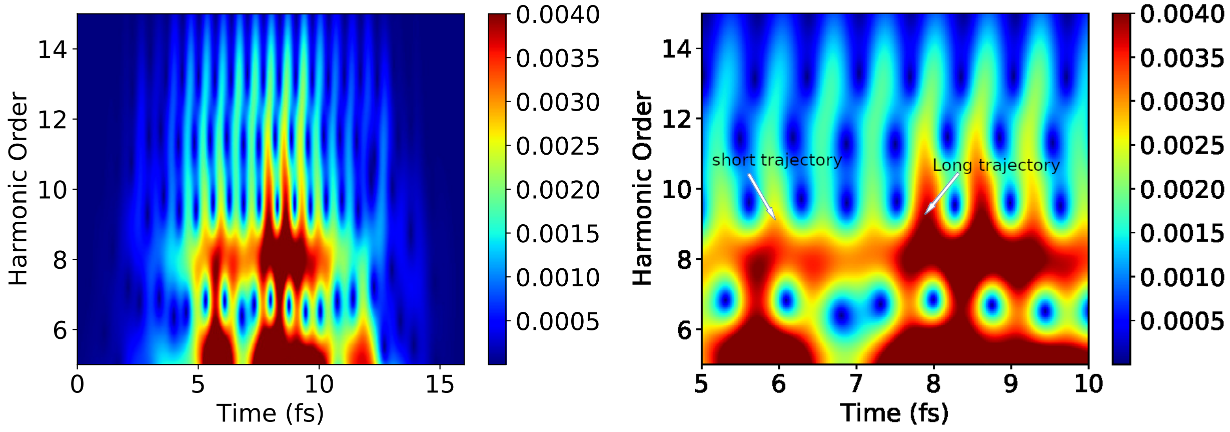

(a)

(b)

Figure 3.23: Wavelet spectrum for N_2^+ interacting with a 400 nm laser pulse of intensity $I = 2 \times 10^{14} \frac{W}{cm^2}$ with polarization direction oriented perpendicular to the molecular axis. Panel (a) shows the spectrum over the total length of the laser propagation, and (b) shows a zoom in from 5 to 10 femtoseconds and has labels showing where the trajectory of the electron is short or long during the propagation of the laser.

From the spectrum we can see where there is an HHG burst during the propagation of the laser pulse. We can also tell for each harmonic order the recombination times which are related to classical trajectories of electrons. We see in figure 3.23b that at about 6 and 8 femtoseconds the electron recombines with the parent ion resulting in an HHG burst of the 9th harmonic. While, this harmonic is emitted at multiple times, the smaller time corresponds to a shorter electron trajectory as a result of the interaction with the laser pulse, and the later time to the long trajectory.

For the nonresonant case there are modifications to the semi-classical description of HHG which are also present in the time-frequency analysis. We consider the case where N_2^+ interacts with a 400 nm laser of intensity $I = 2 \times 10^{14} \frac{W}{cm^2}$ with polarization direction oriented parallel to the molecular axis, shown in figure 3.24. We know from previous discussion that this induces a coupling between the $3\sigma_g$ and $2\sigma_u$ orbitals, and as a result we expect this nonadiabatic behavior to be present in the wavelet spectrum. Unlike the nonresonant case presented above, the generation of harmonics in the resonant case is far more complex, and the use and interpretation of classical trajectories become difficult when describing what is occurring in the spectrum. Instead, we see modulation due to the nonadiabatic behavior induced by the laser coupling and the spectrum does not exhibit the same periodic nature of the nonresonant case.

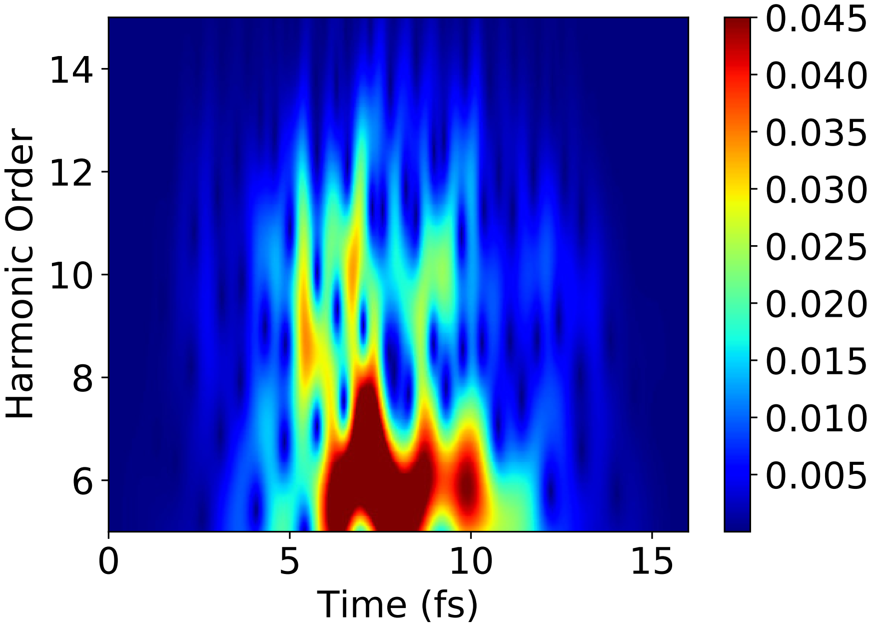

Figure 3.24: Wavelet spectrum for N_2^+ interacting with a 400 nm laser pulse of intensity $I = 2 \times 10^{14} \frac{W}{cm^2}$ with polarization direction oriented parallel to the molecular axis.

3.4 Two-Color High-Harmonic Generation

The interaction of molecular ions with a single color linearly polarized pulse brings about interesting features in HHG spectra in the cases of a laser induced resonant coupling between orbitals. However what happens when one considers adding another laser to the system? Will the effects we have encountered before in the single color linearly polarized case still be present, and if so will they be enhanced or diminished? What about changing the polarization of the fields, will there be noticeable changes to the HHG spectra? We consider each of these cases in this part of the thesis.

3.4.1 Two-Color Linearly Polarized Laser Pulses

We begin by considering two cases, (a) N_2^+ interacting with a 400 nm pulse with polarization fixed parallel to the molecular axis, and an 800 nm pulse with polarization varied from 0^o to 90^o

with respect to the molecular axis, and (b) N_2^+ interacting with an 800 nm pulse with polarization fixed perpendicular to the molecular axis, and a 400 nm pulse with polarization varied from 0^o to 90^o with respect to the molecular axis. Figure 3.25 shows a schematic diagram of both cases (a) and (b). Recall that for case (a) the 400 nm pulse will induce a coupling between $3\sigma_g$ and $2\sigma_u$, and for (b) an 800 nm pulse will induce a coupling between $3\sigma_g$ and $1\pi_u$. Will the addition of the other pulses to the system affect coupling between orbitals thus drastically changing the HHG spectra?

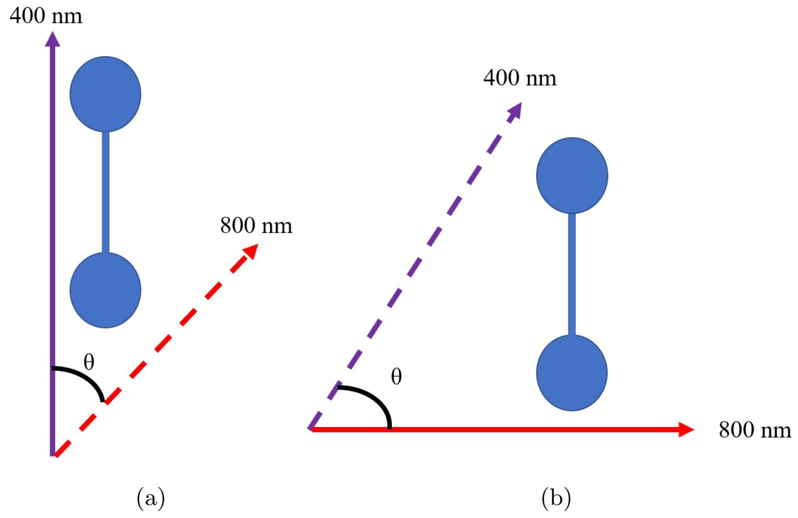

Figure 3.25: Schematic diagram for the N_2^+ interacting with (a) a 400 nm pulse with fixed polarization parallel to the molecular axis and an 800 nm pulse varied in angle $\theta = 0^o$ to $\theta = 90^o$ with respect to the molecular axis, and (b) an 800 nm pulse with polarization fixed perpendicular to the molecular axis and a 400 nm pulse with polarization varied from $\theta = 0^o$ to $\theta = 90^o$ with respect to the molecular axis.

The HHG spectra for case (a) and all angles θ are shown in figure 3.26. If we compare case (a) to a single color case where N_2^+ interacts with a 400 nm laser pulse of intensity $I = 2 \times 10^{14} \frac{W}{cm^2}$, as shown in figure 3.27 we can see that the HHG spectra show similar signatures and behavior, however there are slight differences. For example, the 3rd harmonic in the single color case seems to have a larger magnitude than harmonics of lower order, whereas in the two-color case the 3rd harmonic is lower in magnitude than those before. In addition, the Mollow sidebands seem to become more broad in the two-color case, which is due to the second 800 nm pulse interfering with the resonant effects. A noticeable difference occurs in the plateau regime of HHG for the two-color case. We see that unlike the single color case the harmonics of higher magnitude extend further in harmonic order, which is a result of the 800 nm pulse, that leads to longer harmonic spectrum than the single 400 nm pulse.

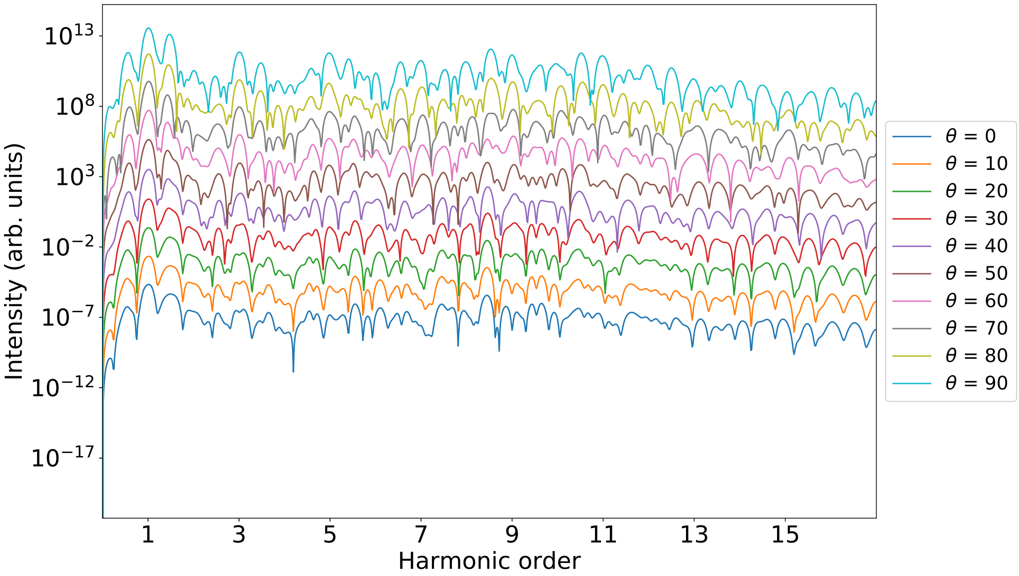

Figure 3.26: HHG spectra for a 400 nm pulse at $2 \times 10^{14} \frac{W}{cm^2}$ polarized along the molecular axis with an 800 nm pump pulse at $1 \times 10^{13} \frac{W}{cm^2}$ with polarization direction rotated from 0^o to 90^o with respect to the molecular axis. Note: Intensities are scaled for comparison.

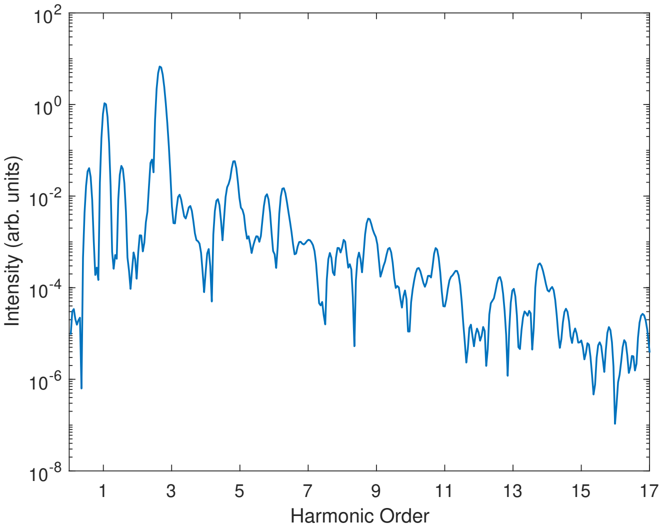

Figure 3.27: HHG spectra for a 400 nm pulse at $2 \times 10^{14} \frac{W}{cm^2}$ polarized along the molecular axis.

We then consider case (b) where the 800 nm pulse of intensity $I = 2 \times 10^{14} \frac{W}{cm^2}$ is the one with polarization direction fixed perpendicular to the molecular axis. When comparing the spectrum to the single color 800 nm case of intensity $I = 2 \times 10^{14} \frac{W}{cm^2}$ and polarization direction perpendicular to the molecular axis, as shown in figure 3.13b, we see many notable differences. The sidebands due to the resonant coupling are more defined for the lower order harmonics, but become smaller in magnitude as the angle of the polarization direction of the 400 nm is varied from $\theta = 0^o$ to $\theta = 90^o$. Also, as the harmonic order is increased, the resolution of the sidebands becomes worse and so it is not clear if there are indeed Mollow sidebands occurring as a result of the resonant coupling by the 800 nm pulse, or if they are even harmonics resulting from a breaking of inversion symmetry due to the second laser being present. Regardless of the details, it is safe to assume that the addition of a second pulse does not enhance the emission of Mollow sidebands, but rather suppresses them. Also, while some features of HHG for a single color are present in case (a) we see that it is not so in case (b) so we can say that features in HHG spectra are indeed modified when adding a second pulse to interact with our system.

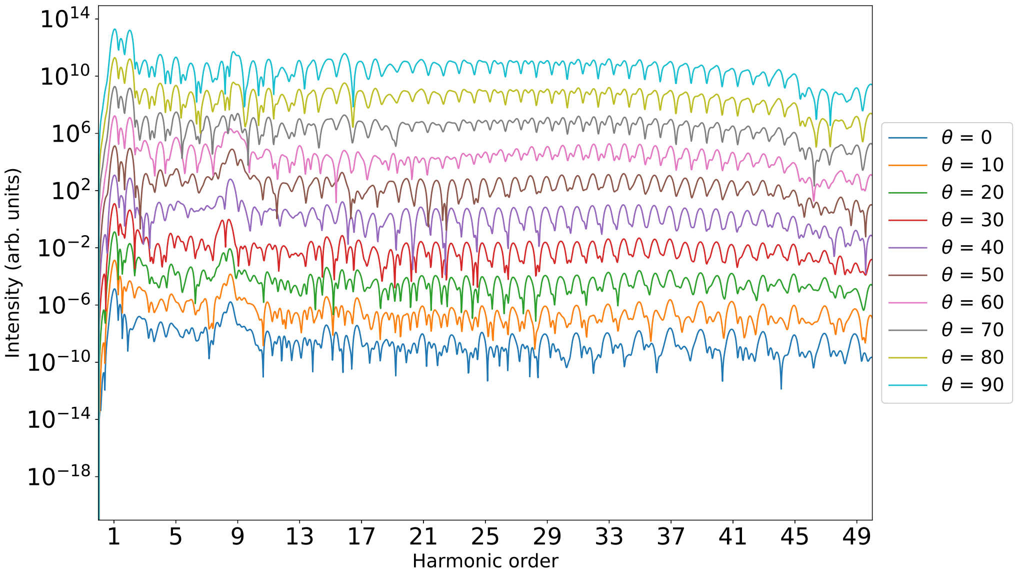

Figure 3.28: HHG spectra for an 800 nm at $2 \times 10^{14} \frac{W}{cm^2}$ probe pulse polarized along the molecular axis with an 400 nm pump pulse at $1 \times 10^{13} \frac{W}{cm^2}$ with polarization direction rotated from 0^o to 90^o with respect to the molecular axis. Note: Intensities are scaled for comparison.

3.4.2 Two-Color Circularly Polarized Laser Pulses

As we have seen molecules interacting with strong linearly polarized pulses exhibit interesting phenomena such as the appearance of Mollow sidebands in HHG spectra as a result of resonant coupling, and the generation of ellipticaly polarized harmonics when the symmetry of the system is broken. However, we ask the question of what occurs when the laser field has a circular polarization? Will the generated harmonics be circularly polarized as well? The answer to this question is actually quite straight forward, no harmonics will be generated. The reason being that a strong single circularly polarized pulse will ionize the wavepackets and cause no recombination with the parent ion, hence no generated harmonics. However, if a second circularly polarized pulse is added to the system, then there will in fact be harmonic generation as was shown by Eichmann et al. [29] in which two cases were considered, the first being two circularly polarized pulses of frequencies ω and 2ω, respectively, with the electric field vectors co-rotating in the same plane. In this case it was seen that all harmonics of frequency $n\omega$ $(n = 0, 1, 2, ...)$ were emitted with elliptical polarization. The second case considered the same fields but counter-rotating and it was seen that harmonics of frequency $(3n \pm 1)\omega$ were emitted with circular polarization with their helicity changing signs from one harmonic to the next. This is in fact quite different to the case of atoms and molecules interacting with a linearly polarized pulse, where only odd harmonics appear in the respective HHG spectrum.

In this thesis we consider the cases of neutral H_2 and ionic H_2^+ interacting with bi-chromatic co- and counter- rotating fields of wavelengths 400 nm and 800 nm at intensity $I = 1 \times 10^{13} \frac{W}{cm^2}$. The fields are shown in figure 3.29a-b where (a) corresponds to the co-rotating case, and (b) the counter-rotating case.

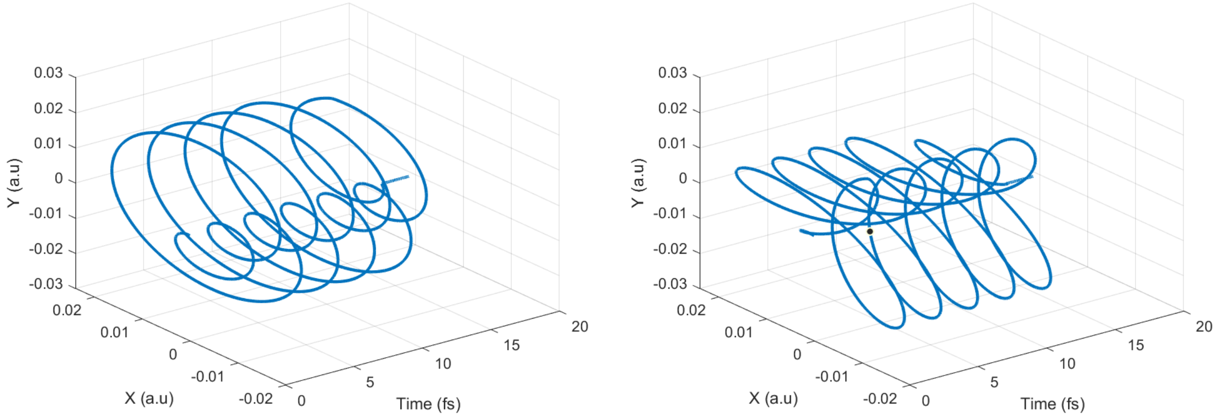

(a)

(b)

Figure 3.29: Plots of bichromatic laser fields of wavelengths 400 nm and 800 nm with intensity $I = 1 \times 10^{13} \frac{W}{cm^2}$ for cases where the fields are (a) co-rotating and (b) counter-rotating.

We first consider H_2 under the presence of bichromatic pulses for both the cases mentioned above. We obtain HHG spectra by performing calculations using TDDFT. Figure 3.30a-b shows the HHG spectra for the cases of (a) co-rotating and (b) counter-rotating bichromatic fields. By inspection of the respective spectra, we can see that harmonic generation is greatly suppressed when the fields are co-rotating and the intensity of harmonics diminishes greatly as harmonic order increases, however, harmonics of order $n\omega$ seem to be present as discussed in [30]. When the fields are counter-rotating the intensity of generated harmonics falls off slower than in the co-rotating case and higher orders of harmonics are present in the HHG spectra. In addition, we observe that harmonics generated are of order $(3n \pm 1)\omega$ as discussed in [30].

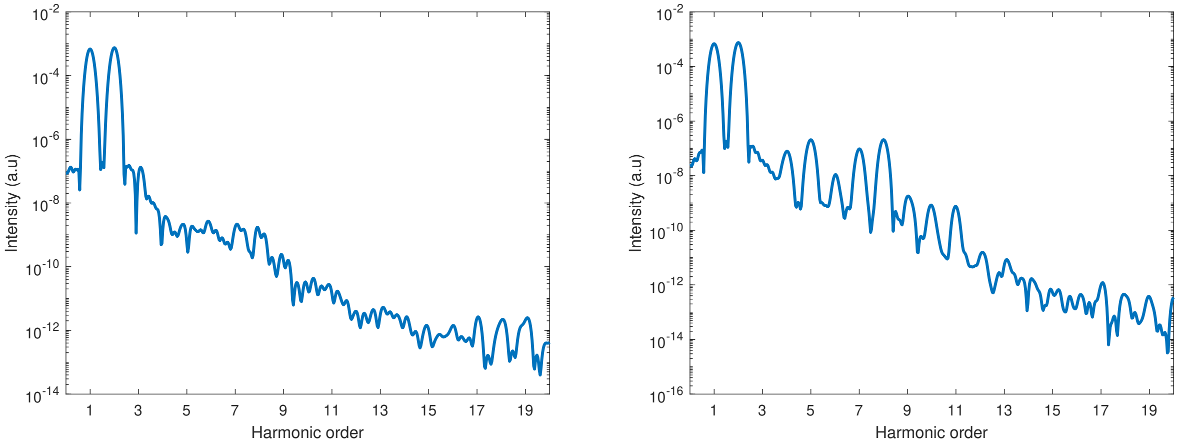

(a)

(b)

Figure 3.30: HHG spectra of H_2 interacting with bichromatic circularly polarized pulses of wavelengths 400 nm and 800 nm with intensity $I = 1 \times 10^{13} \frac{W}{cm^2}$ for the cases where the fields are (a) co-rotating and (b) counter-rotating.

In conclusion, HHG spectra obtained from molecules are highly dependent on the type of laser used. As we saw the differences between linearly and circularly polarized pulses producing HHG vary drastically. This tells us the three-step semi-classical model can be heavily modified depending on the laser used, and that in molecules the prediction of HHG patterns is not as simple as in atomic systems.

3.5 Summary

In this chapter we investigated the appearance of Mollow sidebands appearing in HHG spectra of open shell molecules such as N_2^+ and $C_2H_4^+$. We found that the sidebands were caused by a laser induced coupling between orbitals. We illustrated the appearance of the phenomena for both parallel (σ-σ) transitions and perpendicular (σ-π) transitions. We further analyzed the appearance of Mollow triplets by considering a simple two level system given by the optical Bloch equations and showed that Rabi oscillations could indeed be captured by both theories, though certain differences arise in HHG due to the complexity and approximations of the theories. We also considered how different pulse envelopes affect the appearance of Mollow sidebands and showed that the resolution of the sidebands in HHG spectra are highly dependent on the envelope used. We then looked at the time frequency analysis to give insight in the generation of harmonics during the interaction with the pulse, which we connected to the timescale of the trajectories of the electron due to the interaction with the pulse.

We also considered the effects of HHG when molecules interact with two linearly polarized pulses. We considered the following two cases: (a) a 400 nm pulse with polarization fixed parallel to the molecular axis and (b) an 800 nm pulse with polarization varied at angles $\theta = 0^o$ to $\theta = 90^o$ with respect to the molecular axis. We found that while some features of single color HHG remain in case (a), the features are greatly modified for case (b), and the addition of the second laser does indeed interfere with the nonadiabatic effects which we observed for the single color case.

Furthermore, we investigated how ellipticaly polarized harmonics can be formed from the interaction between CO_2 and linearly polarized pulses with orientation varied from $\theta = 0^o$ to $\theta = 90^o$ with respect to the laser polarization. We considered the single orbital contributions to ellipticity and compared to experiments reported in [24,25]. We showed that results from experiments and theory agree.

Lastly, we looked at the cases where H_2 and H_2^+ interact with bichromatic circularly polarized pulses at optical frequencies ω and 2ω respectively for the cases of co- and counter rotating pulses.

We compared to previous theoretical results performed in [30] and confirmed that the respective HHG spectra are indeed different than those resulting from interactions with linearly polarized pulses, which in turn leads to the question of whether the three-step semi-classical model of HHG must be modified in the case of pulses with non-linear polarization, and that such pulses lead to interesting features in HHG spectra.

Chapter 4

Multi-Electron Effects in Strong-Field Ionization

Ionization is a fundamental process that is often studied in AMO, and it can act as a way to obtain information about the dynamics of atomic and molecular systems. While methods such as attosecond streaking and reconstruction of attosecond harmonic beating by interference of two-photon transitions (RABBITT) [31,32,33,34,35,36] allow for the experimental measurement of ionization of electrons at their fundamental timescale, and give insight into the dynamics occurring during the interaction of ultrafast, high intensity laser pulses with atoms and molecules it is useful to use theories such as TDDFT to see if we can extract the same information as in the experiments. While the tunneling ionization model helps paint a picture of the dynamics involved in strong-field ionization of atoms, it lacks the modifications necessary to describe the mechanism in molecules, which implies that there are fundamental differences in the strong-field ionization mechanism of atoms and molecules.

Earlier experimental studies showed that atoms and molecules with similar ionization potentials exhibit similar behavior, *e.g.* their ionization yields were similar when hit with laser pulses of equal peak intensities [37,38,39]. Later experiments discovered that it is not always the case. Ionization experiments using O_2 and Xe, which have similar ionization energies, differed greatly, and this was greatly due to the orbital structure in O_2 [40]. This in fact showed that the tunneling formula was not enough to describe ionization in molecules due to the more complex properties present and or complex dynamics occurring.

In this chapter, we study the ionization effects of molecules in the cases where a laser induces resonant couplings between orbitals, which as shown in previous chapters can lead to non-adiabatic behavior of electron dynamics, also seen in HHG via the occurrence of Mollow sidebands. In addition we study the effects of ionization when multiple lasers interact with a molecule, in particular, if ionization can be enhanced or suppressed.

4.1 Strong-Field Ionization

Since the early days of quantum mechanics, people have studied ionization in such systems, but it was not until 1979 that Agostini *et al.* [41] observed ionization in the non-perturbative light-matter interaction regime. Before this, data obtained by ionization experiments was well described by low-order perturbation theory. However, in the strong-field regime, i.e the non-perturbative regime, it was observed that an atomic or molecular system could in fact absorb multiple photons above the ionization threshold with comparable probabilities and thus the result is called Above-Threshold Ionization (ATI). Typically such a process as ATI occurs in the intensity regime above $10^{13}\frac{W}{cm^2}$. In this intensity regime atoms and molecules are significantly or even completely ionized before the pulse reaches its maximum. To avoid this, it is typical that systems with high ionization potentials, or in the case of this thesis, ultrashort pulses, in the femtosecond regime are used.

Up to this point, strong-field ionization in atoms has been well understood, in particular, in the high-intensity and long-wavelength regimes as described by the so called Keldysh parameter $\gamma < 1$ [42] given by:

$$\gamma = \frac{\omega}{\omega_t}, \tag{4.1}$$

where ω is the laser frequency and ω_t is given by the equation:

$$\omega_t = \frac{E_o}{\sqrt{2I_p}}, \tag{4.2}$$

where E_o is the amplitude of the laser field, and I_p is the ionization potential. With this, strong-field ionization of atoms can be described as the electron tunnel-ionizing out of the Coulomb potential as a result of the interaction with the laser pulse. This process is the same as the first step in the semi-classical three-step model mentioned earlier in this thesis in the chapter devoted to HHG.

However, due to the multi-electron nature of molecules, the ionization mechanisms differ from that in atoms.

4.1.1 Multiphoton Ionization

When the Keldysh parameter is small, $\gamma < 1$, we expect tunneling ionization to occur, however when $\gamma >> 1$, meaning that the ionization potential is much greater than the ponderomotive energy U_p given in equation (3.3), which is common for low intensity fields, or high frequencies then the dominant form of ionization is multiphoton ionization (MPI). In such a process, n photons are absorbed by the electron in the ground state interacting with the field, and the electron transitions via some virtual state (see figure 4.1b) into an excited state or into the continuum (see figure 4.1a). If we increase the strength of the field, many more photons are absorbed and we expect effects such as HHG and ATI to occur.

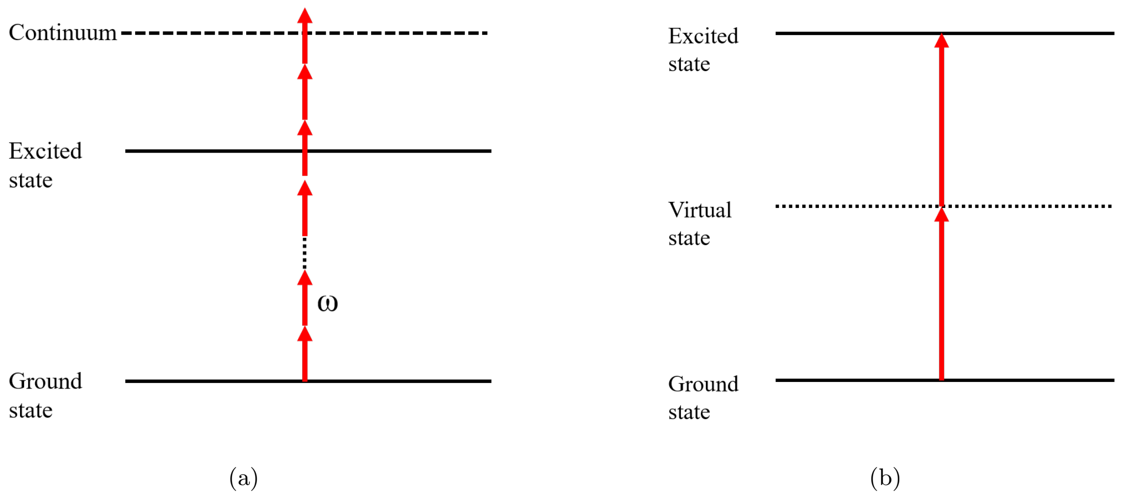

(a)

(b)

Figure 4.1: Figures depicting multiphoton ionization where (a) an electron is ionized into the continuum, and (b) an electron is excited into a higher energy state via multiphoton absorption.

4.2 Charge-Resonance Enhanced Ionization

One fundamental difference between ionization of atoms and molecules is charge-resonance enhanced ionization (CREI). First observed in 1995 for H_2^+ at an internuclear distance R_c, larger than its equilibrium bond length [43]. At this critical internuclear distance R_c the $1\sigma_g$ and $1\sigma_u$ orbitals in H_2^+ become close in energy, as shown in figure 4.2b, and a charge resonant pair of states is created. Figure 4.2a shows the ionization rate as a function of internuclear distance for this study. We can see that at large internuclear distances, especially at $R_c = 10$ a.u. the rate of ionization reaches a maximum, and as a result of the study, it was determined that at this internuclear distance there is in fact a charge resonance occurring between the orbitals, which in turn leads to an enhancement in ionization.

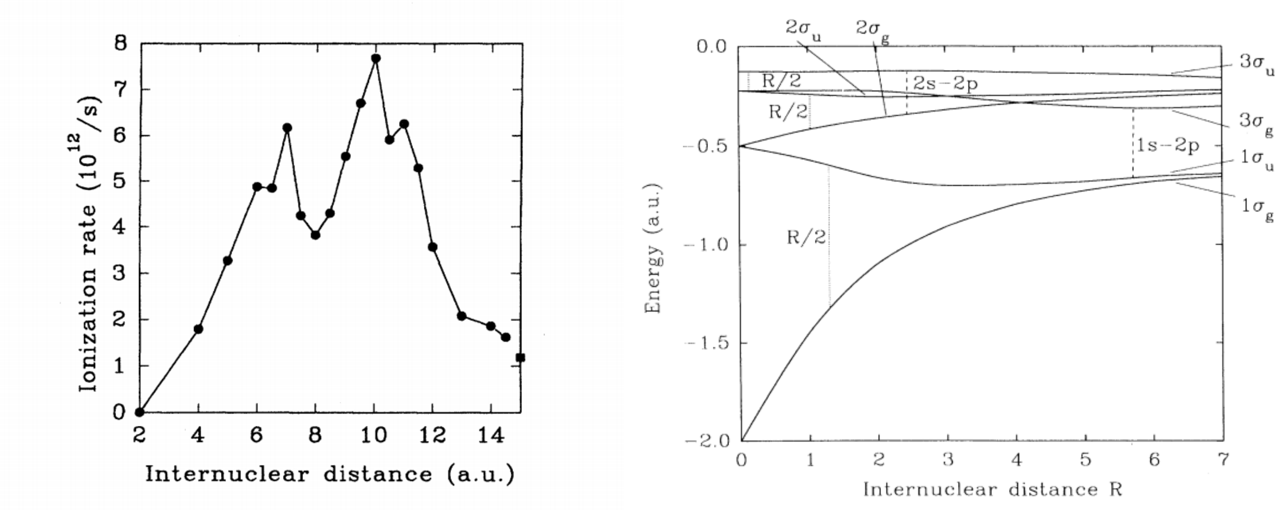

(a)

(b)

Figure 4.2: (a) Ionization rate of H_2^+ as a function of internuclear distance, when interacting with a linearly polarized 1064 nm laser with intensity $I = 10^{14}\frac{W}{cm^2}$ and (b) the energy levels of H_2^+ as a function of internuclear distance. Adapted from [43] and [28].

4.2.1 Charge-Resonance Enhanced Ionization in Multi-Electron Molecules

While the study conducted in [39] gave insight into differences in strong-field ionization of atoms and molecules, it was still limited due to the one electron nature of H_2^+. It is worthwhile to study strong-field ionization and CREI in multi-electron molecules.

Using TDDFT, we solved the time-dependent Kohn-Sham equations (2.31), and obtained the probability density in the i^{th} orbital. From there we obtain the population of a given orbital using:

$$n_i^{ks}(t) = \int d^3\mathbf{r} |\phi_i(\mathbf{r}, t)|^2, \tag{4.3}$$

where $\phi_i(\mathbf{r}, t)$ is the i^{th} Kohn-Sham orbital, and $n_i^{ks}(t)$ is the time dependent population of the given orbital. The resulting ionization probability of the i^{th} orbital is given by:

$$P_i^{ks}(t) = 1 - n_i^{ks}(t). \tag{4.4}$$

Typically, one would expect that the highest occupied molecular orbital would in fact contribute the most towards ionization due to the smaller ionization potential. This is in fact the case for closed shell molecules, as well as those in which there is no laser induced coupling between orbitals. Such examples are shown below in figure 4.3, where a 400 nm pulse at $I = 2 \times 10^{14}\ \frac{W}{cm^2}$ with polarization along the molecular axis interacts with N_2 (left), and a 600 nm pulse at $I = 2 \times 10^{14}$ $\frac{W}{cm^2}$ with polarization also along the molecular axis (right) interacts with N_2^+. Due to N_2 being a closed shell molecule we expect the HOMO to contribute the most to ionization due to the smaller ionization energy, and this is in fact the case, albeit the fact that the laser parameters cause a resonant coupling between HOMO and HOMO-2 in N_2^+ thus resulting in CREI. In the second case we see that even though the molecule is open-shell we do not observe CREI since to the optical frequency of the laser is not equal to the frequency corresponding to the energy difference between orbitals, therefore not inducing a resonant coupling of orbitals.

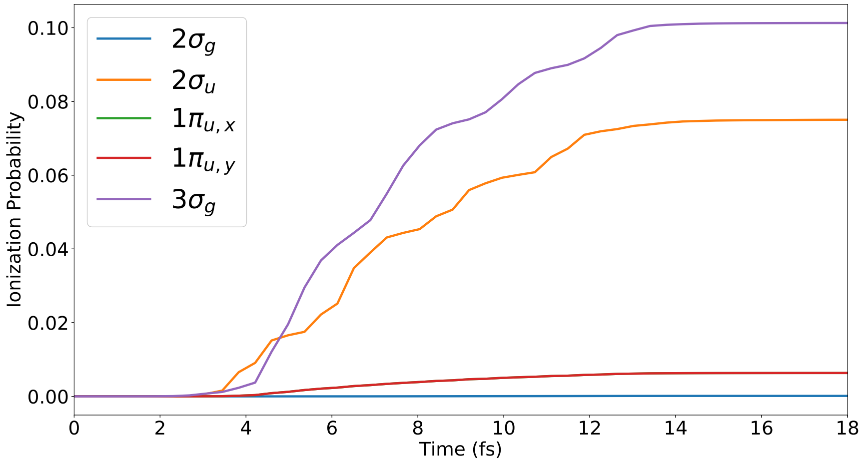

(a)

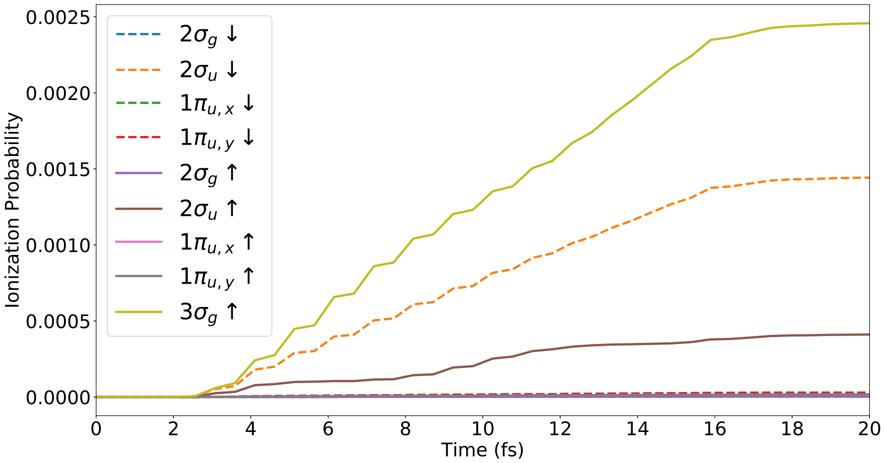

(b)

Figure 4.3: Ionization probability for two cases: (a) N_2 in the presence of a 400 nm laser pulse with intensity $I = 2 \times 10^{14}\ \frac{W}{cm^2}$ and polarization along the molecular axis, and (b) N_2^+ in the presence of a 600 nm laser pulse with intensity $I = 2 \times 10^{14}\ \frac{W}{cm^2}$ and polarization along the molecular axis.

In both cases we can see that the HOMO is the orbital that contributes the most to ionization. Interestingly enough, we would expect the other orbitals ionization probability to be almost negligible, this is in fact not what we see. For both cases the HOMO-2 still has a significant contribution to the ionization. This brings in the following question: is the ionization potential the only factor we must consider? Well, the answer to this question is no, other factors such as orbital symmetry and molecular orientation with respect to the laser pulse play a role in the ionization process. Consider the HOMO-2 which is a $2\sigma_u$ orbital and the HOMO-1 which is a $1\pi_u$ orbital in N_2 and N_2^+. The HOMO-2 extends along the molecular axis, so when the polarization of the pulse is oriented along the molecular axis, the ionized wavepacket interferes constructively along the polarization direction, thus enhancing the ionization of the HOMO-2, while if the polarization of the pulse was aligned perpendicular, the ionized wavepacket would destructively interfere and hence suppress ionization. A similar phenomenon happens for the case of 800 nm in which a resonant coupling occurs between HOMO and HOMO-1 when the polarization is perpendicular to the molecular axis. The HOMO-1 as a π orbital extends perpendicular to the molecular axis, hence it is more easily ionized when the polarization is perpendicular to the molecular axis. In addition, in N_2 it is possible that the HOMO-1 contributes more to ionization than the HOMO as can be seen in figure 4.4.

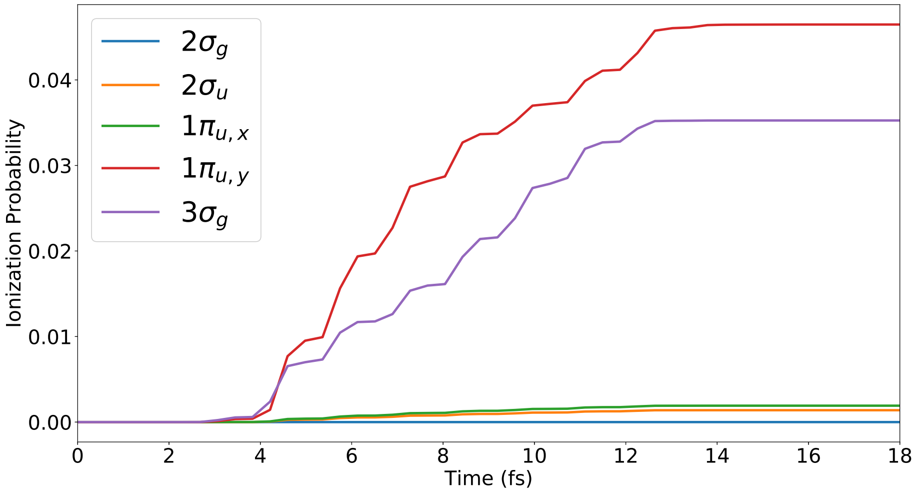

Figure 4.4: Ionization probability for N_2 while under the presence of an 800 nm laser pulse with intensity $I = 2 \times 10^{14} \frac{W}{cm^2}$ and polarization perpendicular to the molecular axis.

4.2.2 Single-Color Ionization

We begin by first investigating ionization when a single laser field is applied to a system of N_2^+ and $C_2H_4^+$. In prior discussion we established that there is a laser induced resonance coupling in N_2^+ between the $3\sigma_g$ and $2\sigma_u$ orbitals when the laser pulse is at 400 nm and has a polarization parallel to the molecular axis, and between the $3\sigma_g$ and $1\pi_u$ orbitals when the laser pulse is at 800 nm and has a polarization perpendicular to the molecular axis. Similarly, in $C_2H_4^+$ a coupling between the $1b_{3g}$ and $1b_{2u}$ orbitals occurs when the laser pulse is at 400 nm and polarized parallel to the molecular axis. As a result of such laser induced resonances we expect that there will be an enhancement of ionization.

The first case we look at is the application of a 400 nm laser pulse polarized in the direction of the molecular axis of N_2^+ at intensity $I = 2\times10^{14}\frac{W}{cm^2}$. The orbital contributions to ionization are shown in figure 4.5. We saw before that for the cases of neutral N_2 and nonresonant laser frequencies that the $3\sigma_g$ orbital would contribute the most to ionization, shown in figures 4.3a-b. However we now see that as a result of the laser induced coupling of orbitals the $2\sigma_u$ orbital contributes the most to ionization. This however brings about another question which is why does the spin down electron in $2\sigma_u$ ionize more than the spin up electron in $2\sigma_u$? The answer to this question is actually quite simple, the presence of a spin down hole makes the transition by the spin down electron more probable, whereas for the spin up electron in the $2\sigma_u$ orbital to excite into the $3\sigma_g$ orbital, the spin up electron occupying it would have to be ionized, first due to the Pauli exclusion principle. Hence we expect the ionization to be greater for the electron with the same spin as the electron hole. The effect is the same for the case of N_2^+ interacting with an 800 nm pulse with polarization perpendicular to the molecular axis. Indeed the $1\pi_u$ orbital contributes the most to ionization as a result of the laser induced resonance between $3\sigma_g$ and $1\pi_u$. Again we see one spin state contributing more to ionization than the other.

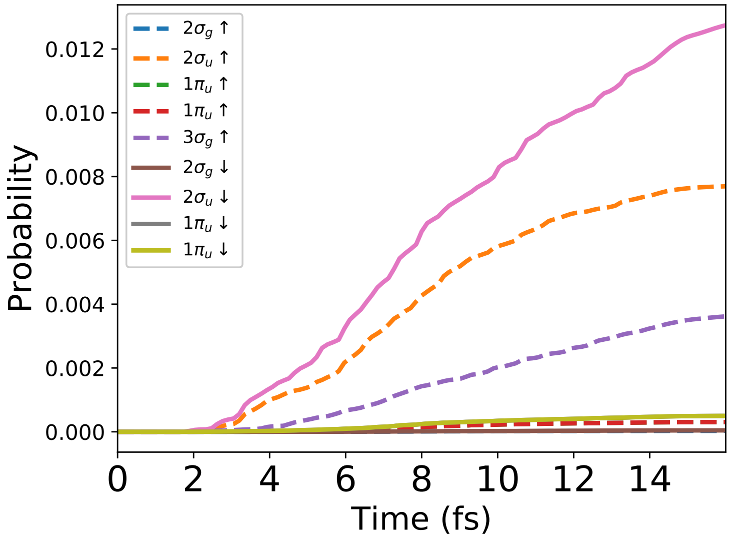

Figure 4.5: Ionization probability for N_2^+ while under the presence of a 400 nm laser pulse with intensity $I = 2 \times 10^{14}\ \frac{W}{cm^2}$ and polarization parallel to the molecular axis.

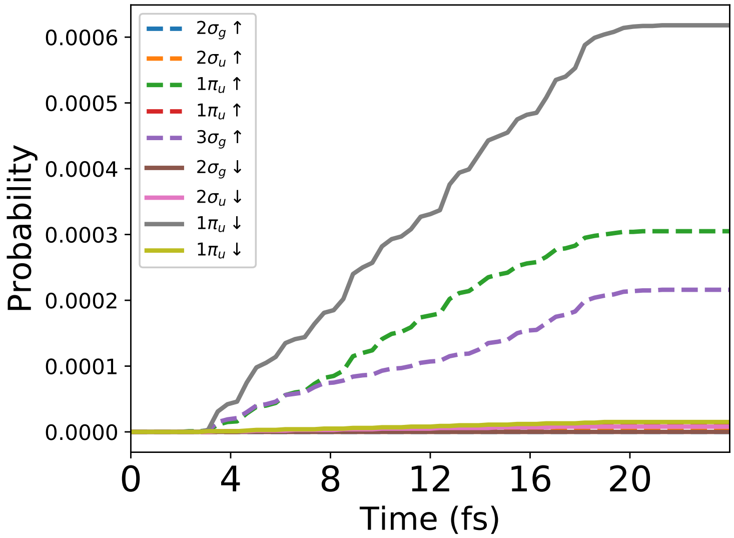

Figure 4.6: Ionization probability for N_2^+ while under the presence of an 800 nm laser pulse with intensity $I = 2 \times 10^{14}\ \frac{W}{cm^2}$ and polarization perpendicular to the molecular axis.

In $C_2H_4^+$ we saw that there is a laser induced resonance transition between the $1b_{3g}$ and $1b_{2u}$

orbitals by a 400 nm laser pulse with polarization parallel to the molecular axis when there is an electron-hole present in the $1b_{3g}$ orbital. We then expect that as a result of this coupling that the $1b_{3g}$ would contribute the most to ionization, and indeed this is what we observe as shown in figure 4.7, and the explanation is the same as for N_2^+.

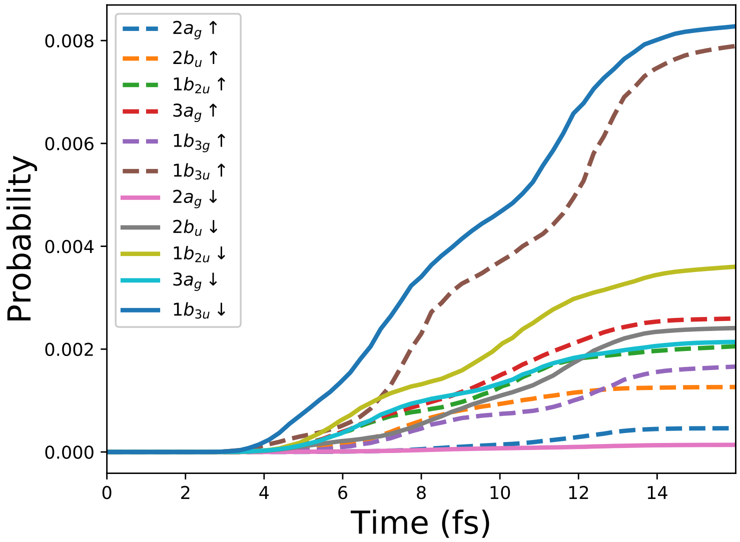

Figure 4.7: Ionization probability for $C_2H_4^+$ while in the presence of a 400 nm laser pulse with intensity $I = 1 \times 10^{14}\ \frac{W}{cm^2}$ and polarization perpendicular to the molecular axis.

4.2.3 Two-Color Ionization

As we saw, CREI is indeed present when there is a laser induced resonance between orbitals. However, it is worthwhile to investigate the effects of ionization when an additional laser is made to interact with the system. We first consider two cases: (1) a 400 nm laser with fixed polarization parallel to the molecular axis with intensity $I_1 = 2 \times 10^{14} \frac{W}{cm^2}$, and an 800 nm laser with polarization varying from 0^o to 90^o with respect to the molecular axis with intensity $I_2 = 1 \times 10^{14} \frac{W}{cm^2}$, and (2) an 800 nm laser with fixed polarization perpendicular to the molecular axis with intensity $I_1 = 2 \times 10^{14} \frac{W}{cm^2}$, and a 400 nm laser with polarization varying from 0^o to 90^o with respect to the molecular axis with intensity $I_2 = 1 \times 10^{14} \frac{W}{cm^2}$. Figure 4.8 shows the total ionization for both cases

(1) and (2), respectively.

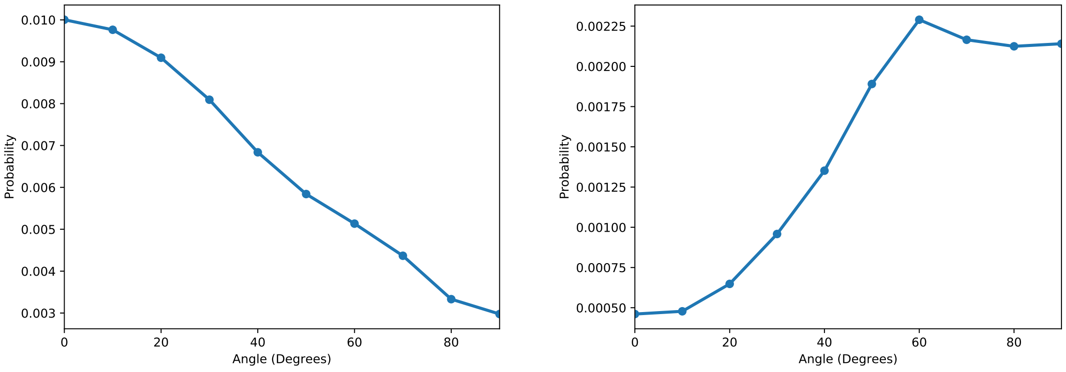

(a)

(b)

Figure 4.8: Total ionization probability as a function of polarization alignment for cases (1) and (2) respectively. In (a) the polarization of the 800 nm pulse is varied from 0^o to 90^o with respect to the molecular axis, and in case (b) the polarization of the 400 nm pulse is varied from 0^o to 90^o with respect to the molecular axis.

We can see that for case (1) the ionization probability is maximized when both the 400 nm and 800 nm laser pulses have polarization parallel to the molecular axis, and minimized when the polarization of the 800 nm pulse is oriented perpendicular to the molecular axis. For case (2) it is not so straightforward, ionization is minimized when the 400 nm pulse is parallel to the molecular axis, as in case (1), but we see that ionization is maximized when the 400 nm pulse is oriented at 60^o with respect to the molecular axis, and not when it is 90^o. In order to fully understand why this is occurring we must look at the single orbital contributions to ionization.

4.2.3.1 Orbital Contributions to Ionization

As we saw, for case (1) ionization was enhanced when the polarization of the 800 nm pulse was parallel to the molecular axis, and became further suppressed as we increased the polarization angle to $\theta = 90^o$. Analyzing the single orbital contributions tells us which orbitals contribute most, but it still does not give us the insight as to why suppression of ionization occurs as we increase the angle θ. We must then consider the time dependent projections between coupled orbitals, which initially begin as orthogonal orbitals but become coupled during the interaction with the field. Figures 4.9a-b show the projections between the orbitals $3\sigma_g$ and $2\sigma_u$ as well as $3\sigma_g$ and $1\pi_u$ for the cases where the polarization angles of the 800 nm pulse are (a) $\theta = 0^o$ and (b) $\theta = 90^o$. We see that for case (a) where the 800 nm pulse has polarization parallel to the molecular axis the projection between $3\sigma_g$ and $2\sigma_u$ has more irregular oscillations than in case (b), which can be interpreted that the projected orbitals, which are typically orthogonal, being more in resonance during the interaction with the laser field and so ionization is enhanced, whereas in case (b) we see that the oscillations occurring in the time dependent projections of orbitals behave in a more periodic manner with values ranging from 0 to 0.9, meaning that there are more times in which the orbitals become orthogonal, i.e. nonresonant, resulting in a suppression of ionization. From here we can interpret that as the polarization angle of the 800 nm pulse is changed from $\theta = 0^o$ to $\theta = 90^o$ there are more instances of the coupled orbitals going out of resonance during the pulse, hence reducing the total ionization. We also see, based on the projections, that the major contribution to ionization for case (1) should be coming from the $2\sigma_u$ even as the angle θ is increased. We can confirm this by looking at the peak ionization for each orbital as a function of angle θ, as shown in figure 4.10. We see that for all angles the $2\sigma_u$ is ionized the most just like in the single color case. However the probability of ionization of each orbital is less than that in the single color case, which can mean that the addition of the second pulse is indeed suppressing total and partial ionization of orbitals.

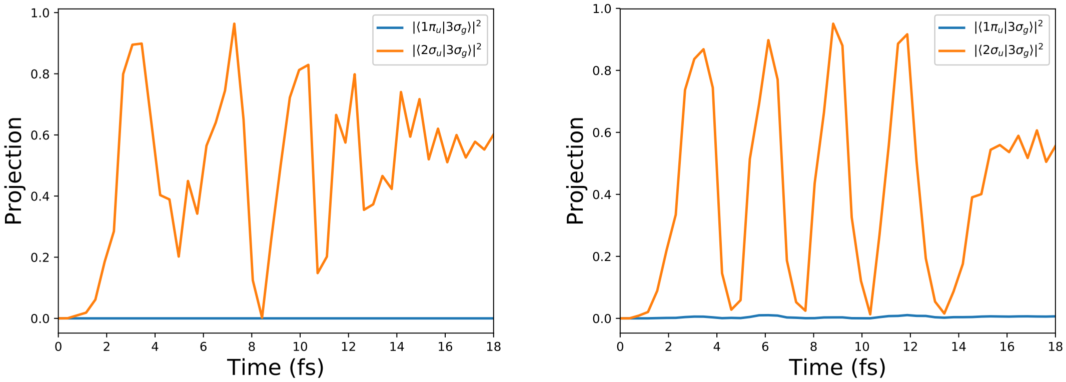

(a) $\theta = 0^o$ (b) $\theta = 90^o$

Figure 4.9: Ground state orbital projections onto time-dependent orbitals for the cases of N_2^+ interacting with a 400 nm pulse of intensity $I = 2 \times 10^{14} \frac{W}{cm^2}$ with fixed polarization along the molecular axis and an 800 nm pulse of intensity $I = 1 \times 10^{14} \frac{W}{cm^2}$ with polarization (a) at angle $\theta = 0^o$ and (b) polarization at an angle $\theta = 90^o$ with respect to the molecular axis.

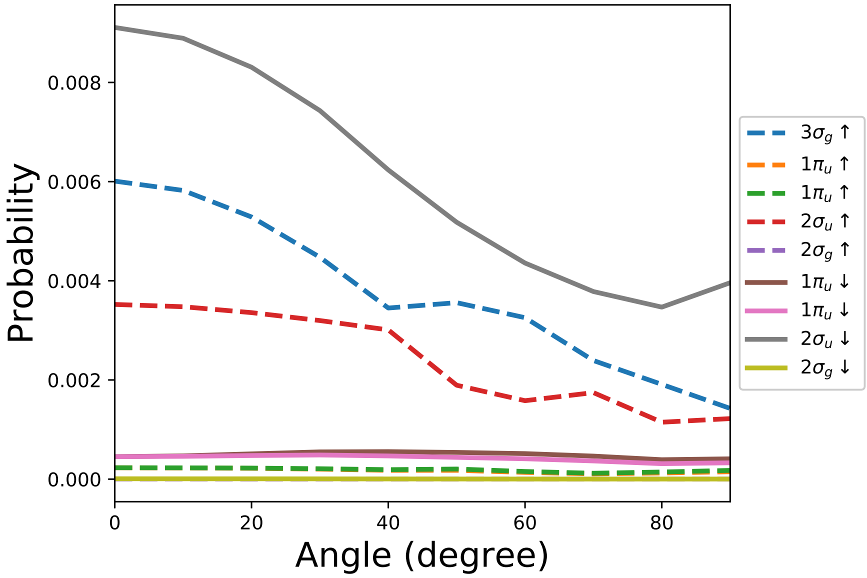

Figure 4.10: Total ionization for each orbital as a function of angle θ for the case where N_2^+ interacts with two pulses, a 400 nm one with polarization fixed parallel to the molecular axis and intensity $I = 2 \times 10^{14} \frac{W}{cm^2}$, and an 800 nm one of intensity $I = 1 \times 10^{14} \frac{W}{cm^2}$ with polarization angle varied from 0^o to 90^o with respect to the molecular axis.

In case (2) we fixed the polarization of the 800 nm pulse and varied the polarization of the 400 nm pulse, and as we saw ionization becomes more complicated than in case (1). Figure 4.8b tells us that there is minimum total ionization when the polarization angle of the 400 nm pulse is $\theta = 0^o$. We would expect that the explanation to this is analogous to case (1) where the angle of the 800 nm pulse is at $\theta = 90^o$ where we see that the projection between coupled orbitals resonates between 0 and 1 meaning that at points during the pulse there is no resonance between orbitals so CREI is not occurring at times, however that is not what we are seeing when looking at the time dependent projections, shown in figure 4.11a-b . In fact we see that there is strong coupling between $3\sigma_g$ and $2\sigma_u$ as well as $3\sigma_g$ and $1\pi_u$. The electrons in both the $2\sigma_u$ and $1\pi_u$ orbitals want to excite into the $3\sigma_g$ however due to Pauli blocking, only one is able to be ionized at a given time. Therefore ionization coming from both orbitals is suppressed as CREI only occurs at shorter time periods during the laser pulse. We also see from figure 4.12 that there is a small difference between the contributions of ionization from the $1\pi_u$ and $2\sigma_u$ orbitals unlike in the single color case where almost no ionization came from $2\sigma_u$. Again, this is explained by looking at the time dependent projections between orbitals which tells us that there is a strong coupling between $3\sigma_g$ and $2\sigma_u$ meaning that ionization from that orbital will be enhanced. When the polarization angle of the 400 nm pulse is $\theta = 90^o$ we see that there is only a resonance between $3\sigma_g$ and $1\pi_u$ which is expected because the 400 nm pulse does not couple any orbitals when the polarization is perpendicular to the molecular axis. We also see that when the angle is $\theta = 90^o$ this becomes more like the single color case of an 800 nm pulse polarized perpendicular to the molecular axis, and the ionization is coming mostly from the $1\pi_u$ orbital and the ionization from the $2\sigma_u$ goes almost to zero.

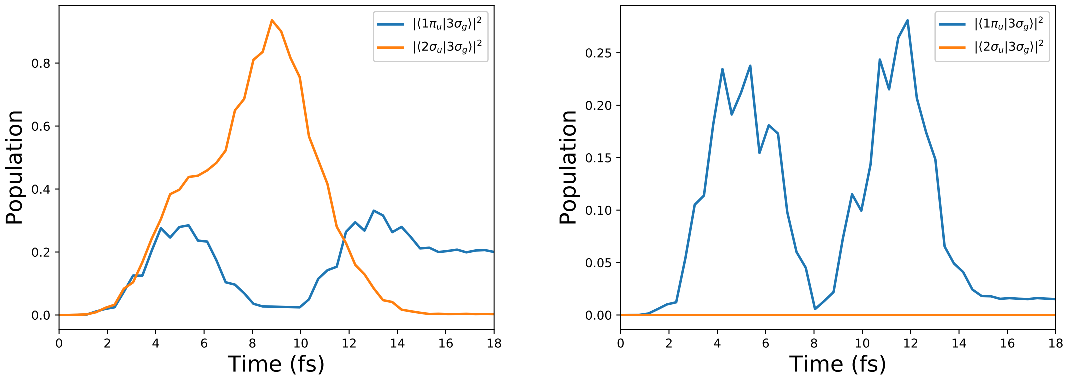

(a) $\theta = 0^o$

(b) $\theta = 90^o$

Figure 4.11: Ground state orbital projections onto time-dependent orbitals for the cases of N_2^+ interacting with an 800 nm pulse of intensity $I = 2 \times 10^{14} \frac{W}{cm^2}$ with fixed polarization perpendicular to the molecular axis and a 400 nm pulse of intensity $I = 1 \times 10^{14} \frac{W}{cm^2}$ with polarization (a) at angle $\theta = 0^o$ and (b) polarization at an angle $\theta = 90^o$ with respect to the molecular axis.

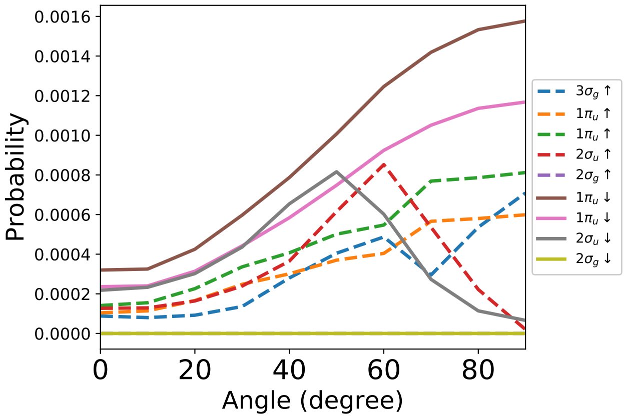

(a)

Figure 4.12: Ionization probability for each orbital as a function of angle θ for the case where N_2^+ interacts with two pulses, a 800 nm one with polarization fixed perpendicular to the molecular axis and intensity $I = 2 \times 10^{14} \frac{W}{cm^2}$, and a 400 nm one of intensity $I = 1 \times 10^{14} \frac{W}{cm^2}$ with polarization angle varied from 0^o to 90^o with respect to the molecular axis.

As we saw case (2) had a maximum ionization when the polarization angle of the 400 nm pulse was $\theta = 60^o$ with respect to the molecular axis. This is unlike case (1) where the ionization has a maximum and minimum at $\theta = 0^o$ and $\theta = 90^0$ respectively. In figure 4.12 we see that at this angle there is also a large contribution to ionization from the spin up electron in the $2\sigma_u$ orbital. This indicates that there is strong coupling between the spin up states of $3\sigma_g$ and $2\sigma_u$. In fact for all angles up to $\theta = 60^o$ there seems to be a large contribution from the $2\sigma_u$ orbital, which is contrary to what we have seen because a laser induced coupling between $3\sigma_g$ and $2\sigma_u$ should only occur when the 400 nm laser is polarized parallel to the molecular axis. This is an indicator that the addition of a second pulse is breaking the symmetry of the system such that we are able to still couple $3\sigma_g$ and $2\sigma_u$ even at polarization not parallel to the molecular axis, in turn the ionization is enhanced due to charge resonance. Indeed we can further confirm this by looking at the time dependent projections of the coupled orbitals shown in figure 4.13, and we see that the $3\sigma_g$ and $2\sigma_u$ for both spin up and down remain coupled at this angle which in turn should enhance ionization from those orbitals and contribute to the total ionization.

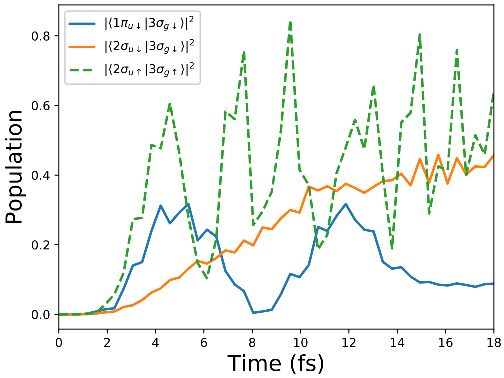

(a)

Figure 4.13: Ground state orbital projections onto time-dependent orbitals for the cases of N_2^+ interacting with an 800 nm pulse of intensity $I = 2 \times 10^{14} \frac{W}{cm^2}$ with fixed polarization perpendicular to the molecular axis and a 400 nm pulse of intensity $I = 1 \times 10^{14} \frac{W}{cm^2}$ with polarization at angle $\theta = 60^o$ with respect to the molecular axis for both the spin up and down orbitals.

4.3 Summary

In this chapter we investigated the effects of strong field ionization in multielectron systems such as N_2^+ and $C_2H_4^+$. We considered the scenarios where a linearly polarized pulse couples two orbitals, and observed that the coupling leads to a charge resonance enhanced ionization. We first studied the case where our system interacts with a single linearly polarized laser pulse.

Later on we looked at how the addition of a second linearly polarized case affects the ionization of our systems. We again considered the two following cases: (1) a 400 nm pulse with polarization fixed parallel to the molecular axis and an 800 nm pulse with polarization varied at angles $\theta = 0^o$ to $\theta = 90^o$ with respect to the molecular axis. We saw that for case (1) the behavior of ionization was almost analogous to that of the single color 400 nm case observed earlier. We then showed that for case (2) the addition of a second laser pulse further complicates the dynamics, and that resonant induced coupling between orbitals remains present even as the polarization angle of one of the pulses was changed, which is unlike the single color case and case (1), leading to enhancement and suppression of ionization from certain orbitals.

Chapter 5

Electron Localization in Molecules

An indication of multielectron effects occurring in molecules can be seen by studying the behavior of electrons within them while under the influence of a laser pulse. A useful way to investigate such effects is to look at the electron localization, which provides a way to study how said electrons respond to the laser field.

With TDDFT it is possible to visualize electron localization. We do this by solving the time-dependent Kohn-Sham equation (2.31), and by obtaining either the total time-dependent density given by equations (2.33) and (2.35) for the cases in which no spin polarization or spin polarization are implemented in TDDFT, respectively. It is also possible to look at the individual orbital contributions to the electron localization, which gives further insight into how each given electron in a molecule responds to the applied laser field.

This can be done using one of the following equations for spin unpolarized and spin polarized cases, respectively:

$$\rho(\mathbf{r},t) = \sum_{i=1}^{N} |\phi_i(\mathbf{r},t)|^2, \tag{5.1}$$

$$\rho(\mathbf{r},t) = \sum_{\sigma=\uparrow,\downarrow} \rho_\sigma(\mathbf{r},t) = \sum_{\sigma=\uparrow,\downarrow} \sum_{i=1}^{N} |\phi_{i,\sigma}(\mathbf{r},t)|^2, \tag{5.2}$$

where the index i corresponds to the i^{th} molecular orbital.

Upon solving for the total and/or individual orbital density, the three-dimensional densities are then integrated over the spatial dimensions except that along the molecular axis.

$$\rho(z,t) = \int dxdy\rho(\mathbf{r},t). \tag{5.3}$$

One thing to note is that this specific dimension is chosen because it allows us to see the dynamics clearly, in any other dimension chosen it might be difficult to visualize.

After integrating onto the desired spatial dimension and obtaining $\rho(z,t)$, the ground state density $\rho(z,t=0)$ is subtracted:

$$\Delta\rho(z,t) = \rho(z,t) - \rho(z,t=0). \tag{5.4}$$

The resulting density difference is then plotted and the electron localization visualized using surface plots. In certain cases the density difference is small so the time propagated density is shown.

In this chapter we will first consider electron localization in the presence of a one-color laser pulse for both N_2^+ and $C_2H_4^+$. We will then consider the case were a second laser is added to our system and investigate the differences observed in comparison to the one-color case. We then finish by looking at a different description of electron localization by Floquet Theory and connect to that obtained by TDDFT.

5.1 Electron Localization in the Presence of One-Color Laser Pulses

We begin by looking at the case in which a molecule interacts with a single linearly polarized laser pulse. As before the molecules considered in our study are N_2^+ and $C_2H_4^+$. Recall that for N_2^+ there is a resonant coupling of the $3\sigma_g$ and $2\sigma_u$ orbitals by a 400 nm pulse, and a resonant coupling of the $3\sigma_g$ and $1\pi_u$ orbitals by an 800 nm pulse. Figures 5.1a-b show the electron localization obtained from the total density for two separate cases: (a) a 400 nm laser pulse, and (b) an 800 nm laser pulse, all with polarization oriented along the molecular axis and with peak intensity $I = 2 \times 10^{14} \frac{W}{cm^2}$. We begin by considering the total electron density, and later look at the orbital contributions to the nonadiabatic effects arising in electron localization. Recall that within our field, nonadiabatic behavior corresponds to the electron not following the oscillation of the electric field during the time propagation and adiabatic behavior means that the electron follows the oscillation of the electric field.

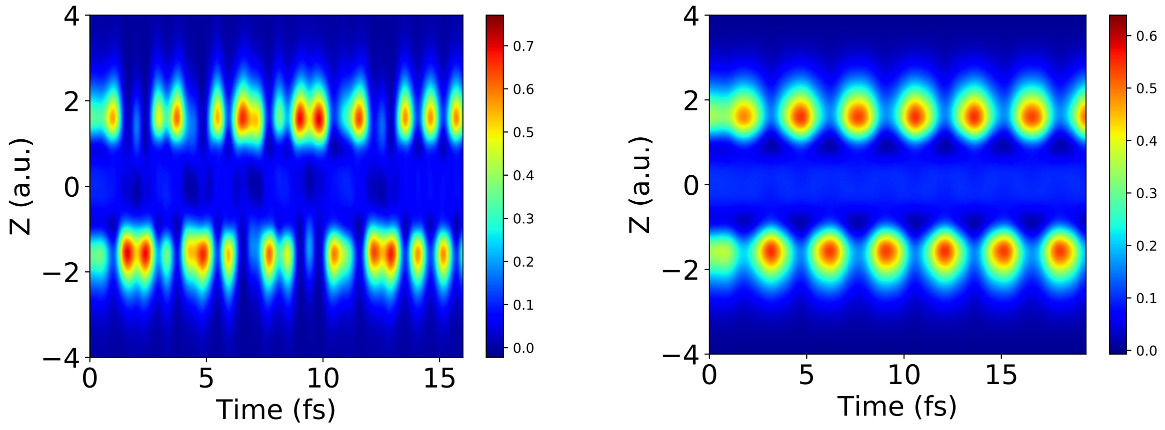

(a)

(b)

Figure 5.1: Visualization of total electron localization of N_2^+ along the molecular axis at different laser wavelengths as a function of time: (a) 400 nm laser field of intensity I $= 2 \times 10^{14} \frac{W}{cm^2}$, and (b) 800 nm laser field of intensity I $=2 \times 10^{14} \frac{W}{cm^2}$. In all cases the orientation of the polarization is parallel to the molecular axis.

It is evident that as the optical frequency gets closer to the resonant frequency between orbitals, then the appearance of non-adiabatic dynamics becomes more visible. In the cases shown in figure 5.1, the interaction with the 400 nm pulse makes the localization of the electron behave more non-adiabatically, hence not following the laser field. As we increase the wavelength to 800 nm, the electron dynamics behaves adiabatically. Visualizing electron localization gives insight into the non-adiabatic behavior brought upon when coupling the $3\sigma_g$ and $2\sigma_u$ orbitals of N_2^+.

Such behavior is also evident in $C_2H_4^+$. Recall that the laser coupled orbitals are $1b_{3g}$ and $1b_{2u}$ by a 400 nm pulse with polarization parallel to the molecular axis. As a result we expect electron localization to be nonadiabatic, and indeed it is as seen in figure 5.2.

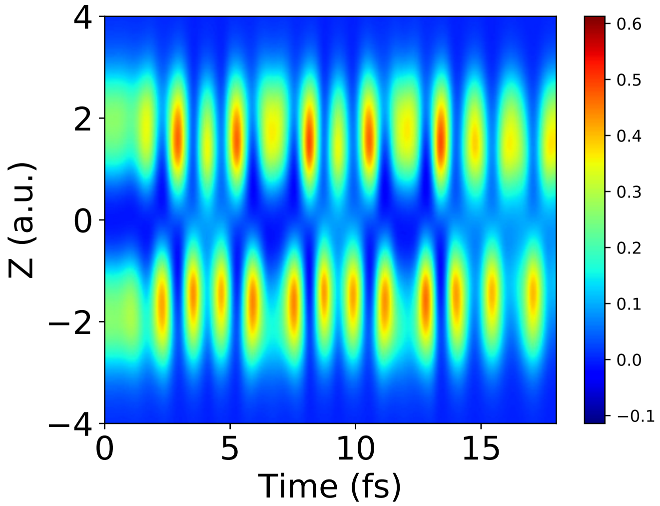

Figure 5.2: Visualization of total electron localization of $C_2H_4^+$ interacting with a 400 nm laser field of intensity I $= 1 \times 10^{14} \frac{W}{cm^2}$ with polarization parallel to the molecular axis. The direction is parallel to the C-C bond.

This nonadiabatic process occurring as a result of the laser induced coupling can be broken down into two competing processes: first, there is an adiabatic response by the electrons to the laser field, second the 400 nm laser couples the two orbitals which leads to an oscillation of the electrons at the Rabi frequency Ω_r resulting in nonadiabatic electron localization at certain times during the laser pulse.

5.1.1 Single-Color Orbital Contributions to Electron Localization in Molecules

While the electron localization for the total density shows that non-adiabatic effects are indeed occurring when there is a laser induced resonant coupling of orbitals it is necessary to look at the individual orbital contributions to see if the coupled orbitals are indeed the ones that are contributing the most to this effect, or if other orbitals are also involved.

We first consider the case of N_2^+ interacting with a 400 nm laser pulse at intensity $I = 2 \times 10^{14} \frac{W}{cm^2}$. Figures 5.3a-d show the independent orbital contribution to electron localization for spin down electrons and figure 5.4a-d for the spin up electrons.

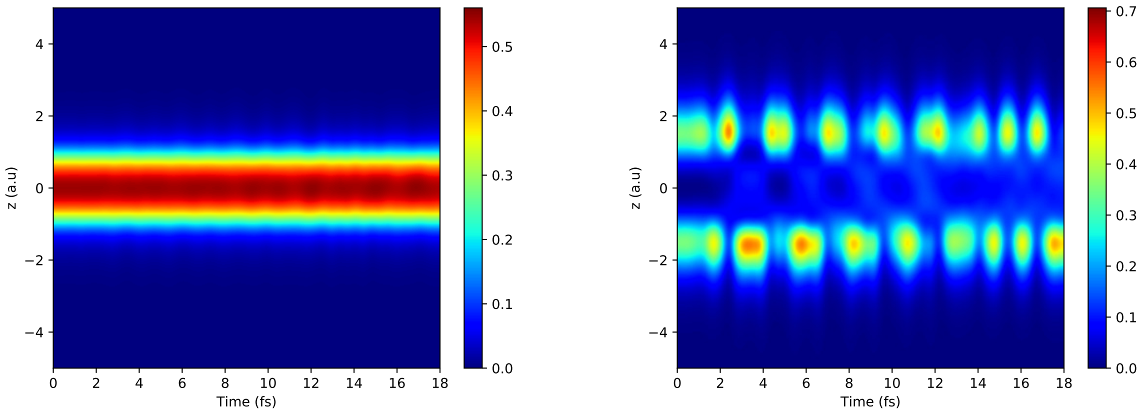

(a) $2\sigma_g \downarrow$

(b) $2\sigma_u \downarrow$

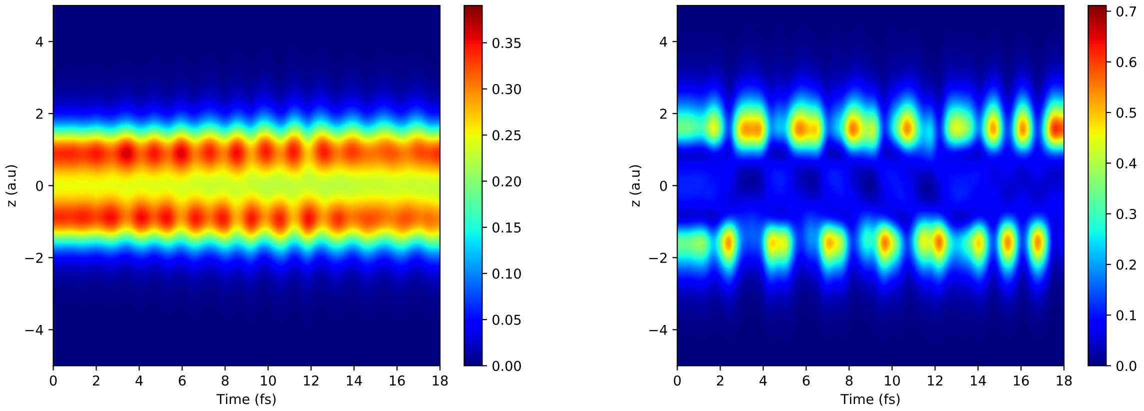

(c) $1\pi_u \downarrow$

(d) $3\sigma_g \downarrow$

Figure 5.3: Visualization of orbital contributions to electron localization of N_2^+ in the presence of a 400 nm laser pulse with intensity $I = 2 \times 10^{14} \frac{W}{cm^2}$ and polarization along the molecular axis. The orbitals are ordered, (a) $2\sigma_g$, (b) $2\sigma_u$, (c) $1\pi_u$, and (d) $3\sigma_g$.

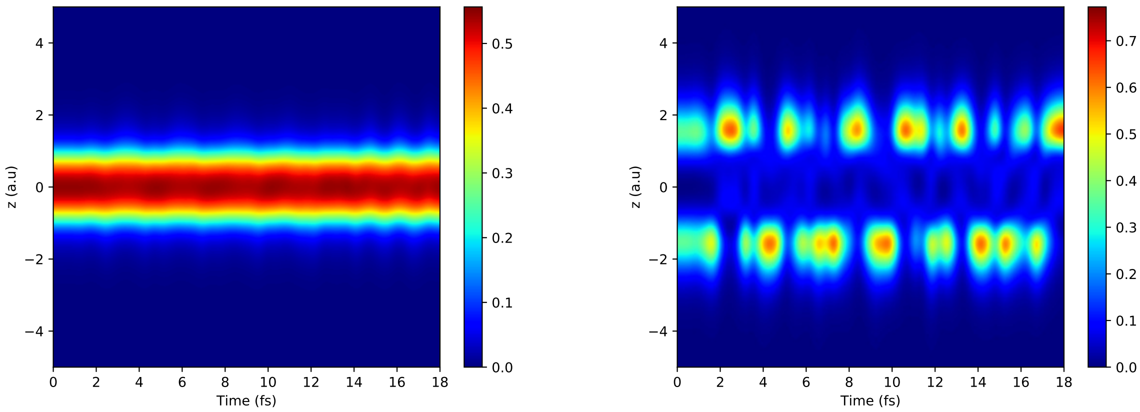

(a) $2\sigma_g \uparrow$ (b) $2\sigma_u \uparrow$

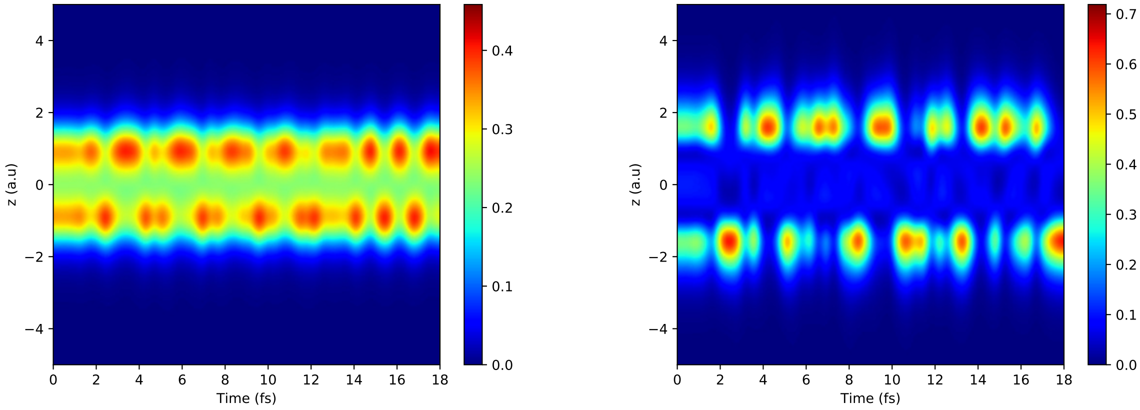

(c) $1\pi_u \uparrow$ (d) $3\sigma_g \uparrow$

Figure 5.4: Visualization of electron localization for the independent orbitals of N_2^+ in the presence of a 400 nm laser pulse with intensity $I = 2 \times 10^{14} \frac{W}{cm^2}$ and polarization along the molecular axis. The orbitals are ordered, (a) 2_g, (b) $2\sigma_u$, (c) $1\pi_u$ and (d) $3\sigma_g$ for the spin up electrons.

Figures 5.3 and 5.4 (b) and (d) correspond to the $2\sigma_u$ and $3\sigma_g$ orbitals for both the spin down and spin up electrons respectively which are coupled by the 400 nm laser pulse. We can see that the nonadiabatic effects are present in those two orbitals while all the others exhibit more adiabatic dynamics. This confirms the idea that there are two competing processes occurring in nonadiabatic electron localization as mentioned before. Interestingly enough we see in figure 5.4c that the $1\pi_u$

orbital exhibits some nonadiabatic signature during certain instances of time. We can explain this by looking at the time-dependent energy expectation values $\langle \phi_i(0)|H(t)|\phi_i(0)\rangle$ of each molecular orbital ϕ_i during the propagation with the pulse shown in figure 5.5. We see that there are instances in which there is an energy crossing by the $1\pi_u$ and $3\sigma_g$ orbital energies, which indicate that at those times there is a short lived orbital coupling, giving rise to nonadiabatic dynamics in the electron localization of the $1\pi_u$ orbital.

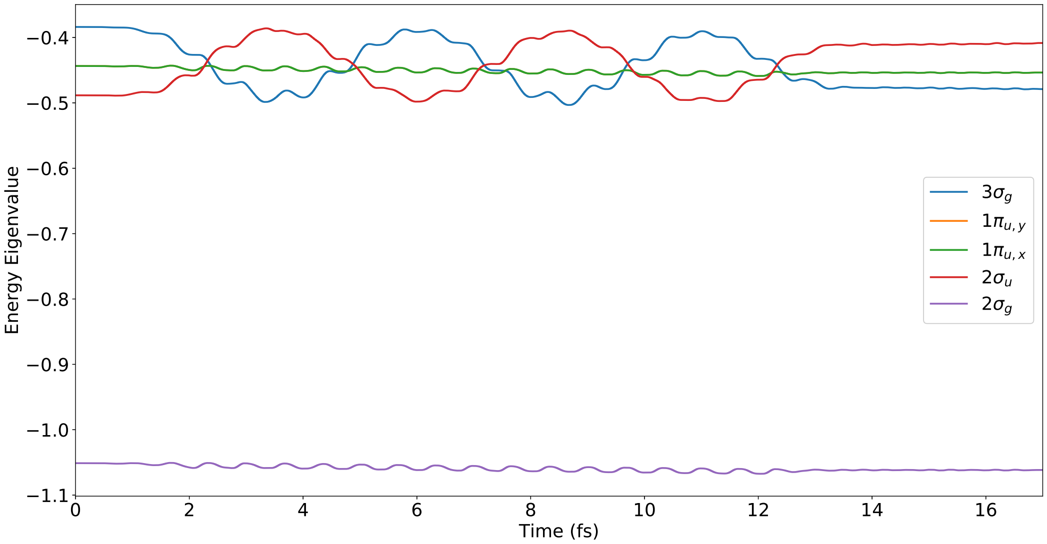

(a)

Figure 5.5: Time-dependent energy expectation values of each molecular orbital of N_2^+ during the interaction with a 400 nm laser pulse.

By the same argument as for N_2^+, we then expect similar dynamics to occur in $C_2H_4^+$, however when looking at the independent orbital contributions for both spin down and spin up, figures 5.7 and 5.8a-f respectively, we see that nonadiabatic effects are present not only in the coupled orbitals $1b_{3g}$ and $1b_{2u}$ but also in other orbitals. This brings about the question of whether or not nonadiabatic electron localization is indeed only caused by laser induced coupling of orbitals. By similar analysis to that in N_2^+ we consider the time-dependent energy expectation values of $C_2H_4^+$

during the interaction of the laser pulse to provide us with an explanation of this phenomena as shown in figure 5.6. We see that during the pulse there are many crossings of the energy values for many orbitals meaning that at certain times during the pulse there exist couplings between other orbitals which will in turn result in the appearance of nonadiabatic behavior for different orbitals.

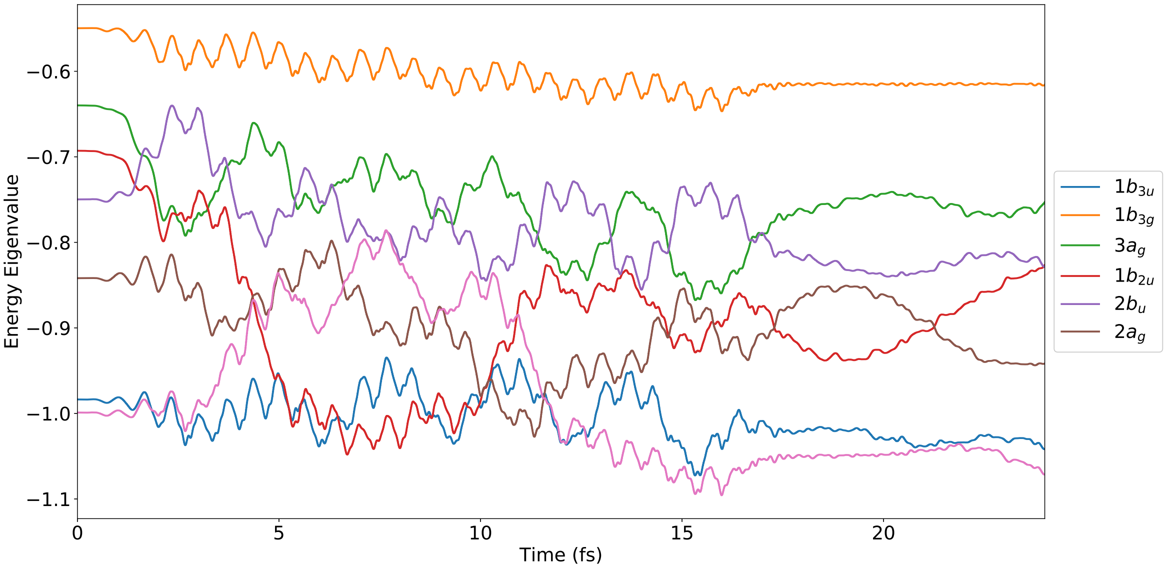

(a)

Figure 5.6: Time-dependent energy expectation values of each molecular orbital of $C_2H_4^+$ during the interaction with a 400 nm laser pulse.

The conclusion is then that other features such as orbital geometry and energy spacing between orbitals must be considered when investigating such effects so it is expected that nonadiabatic response in electron localization for $C_2H_4^+$ can indeed appear from orbitals that one would not expect to be coupled by the laser pulse.

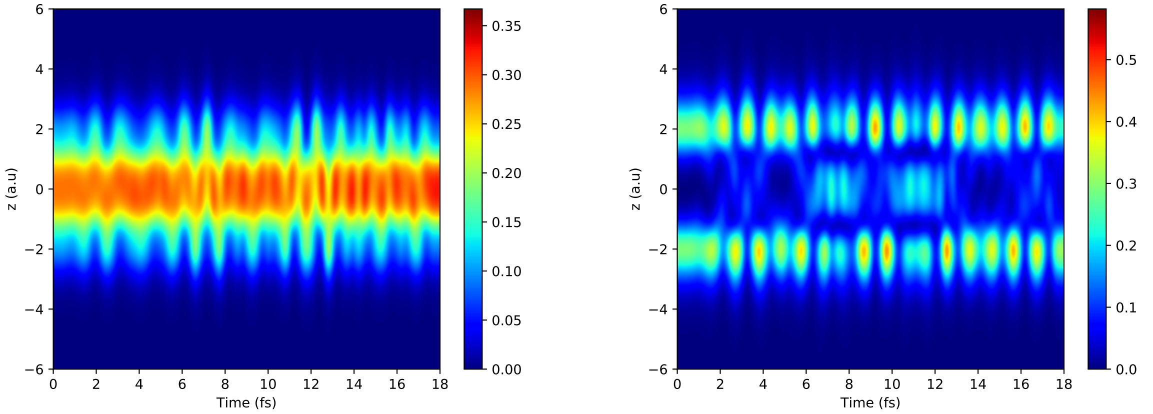

(a) $2a_g \downarrow$ (b) $2b_u \downarrow$

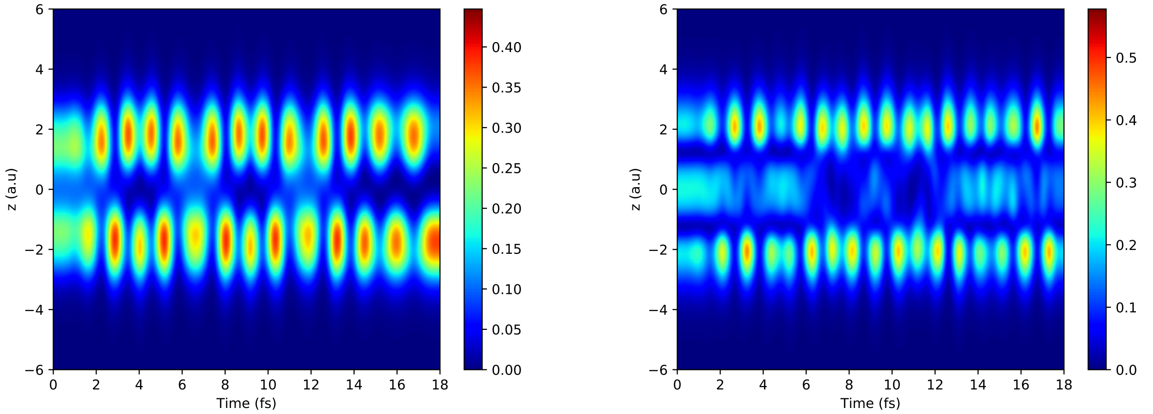

(c) $1b_{2g} \downarrow$ (d) $3a_g \downarrow$

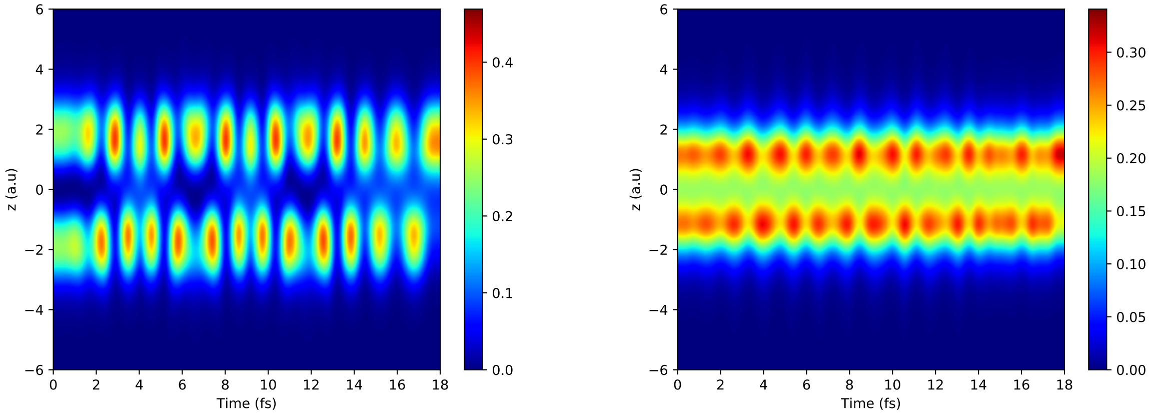

(e) $1b_{3g} \downarrow$ (f) $1b_{3u} \downarrow$

Figure 5.7: Visualization of electron localization for the individual orbitals of $C_2H_4^+$ while in the presence of a 400 nm laser pulse with intensity $I = 1 \times 10^{14} \frac{W}{cm^2}$ and polarization along the molecular axis spin down electrons.

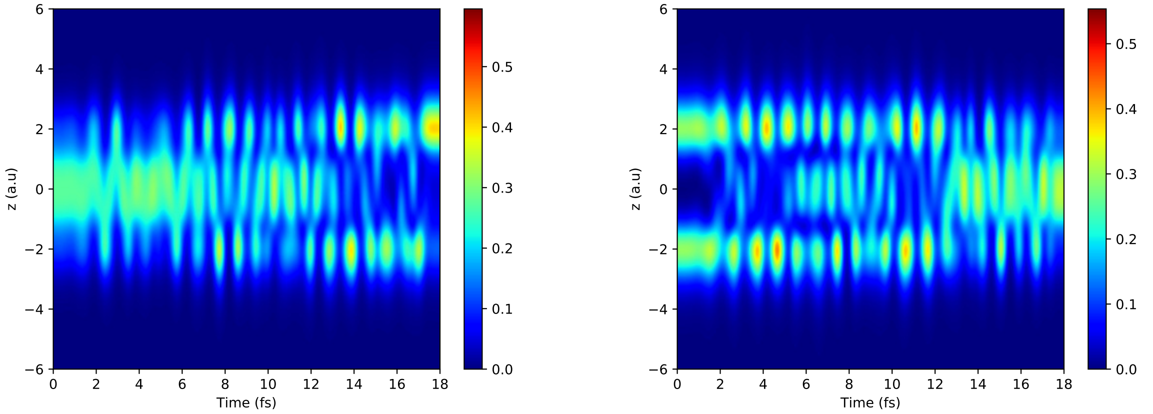

(a) $2a_g \uparrow$ (b) $2b_u \uparrow$

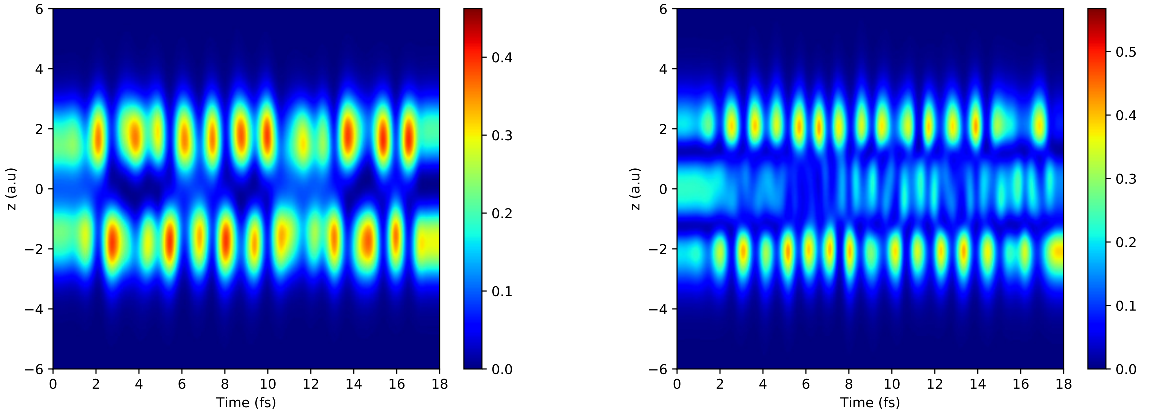

(c) $1b_{2u} \uparrow$ (d) $3a_g \uparrow$

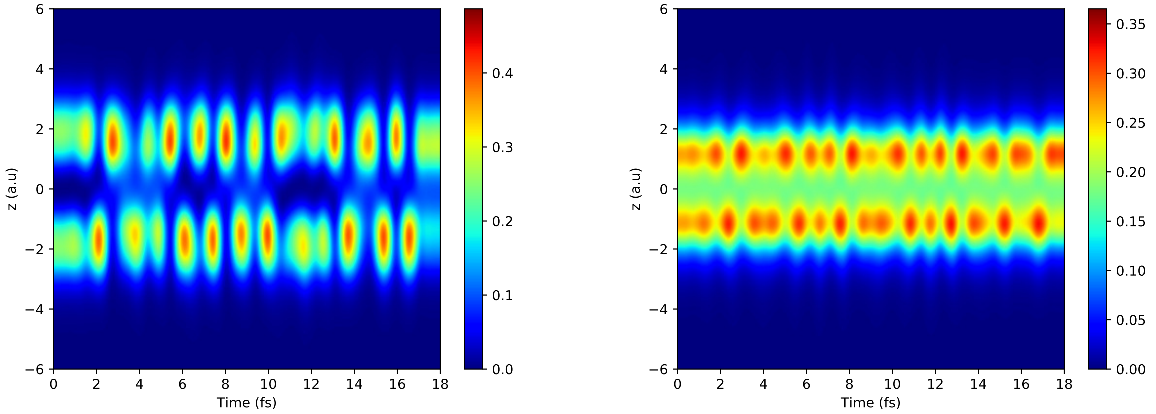

(e) $1b_{3g} \uparrow$ (f) $1b_{3u} \uparrow$

Figure 5.8: Visualization of electron localization for the individual orbitals of $C_2H_4^+$ while in the presence of a 400 nm laser pulse with intensity $I = 1 \times 10^{14} \frac{W}{cm^2}$ and polarization along the molecular axis for spin up electrons.

While the interaction of molecules with ultrashort laser pulses showed interesting behavior occurring in electron localization we now ask the question of what will happen to electron localization if another laser pulse is added to our system.

5.2 Electron Localization in the Presence of Two-Color Laser Pulses

While one color interactions bring about interesting nonadiabatic features in electron localization as a result of two competing processes, it is worthwhile to ask if one can control these effects by the addition of a second laser pulse. We consider the case shown in figure 3.25a where we have N_2^+ interacting with a 400 nm pulse with polarization fixed along the molecular axis, and an 800 nm pulse with polarization varied along the molecular axis with angle $\theta = 0^o$ to $\theta = 90^o$ in increments of $\theta = 10^o$. For this case the pulse with the fixed polarization is designed to control the coupling effects while the one whose polarization varies is designed to either enhance or suppress such effects. We only consider the case with the 400 nm pulse with fixed polarization because as mentioned, electron localization is difficult to see if we consider projecting along dimensions that are not the same as the molecular axis. We present the total electron localization for each angle θ in figures 5.9a-j. It is evident that nonadiabatic electron localization is neither suppressed nor enhanced, in fact it seems to remain the same for all angles presented. This could be due to the intensities we have chosen for the pulses. For the 400 nm pulse the intensity was $I = 2 \times 10^{14} \frac{W}{cm^2}$, while for the 800 nm pulse the intensity was $I = 1 \times 10^{14} \frac{W}{cm^2}$, which are not too different, however because the intensity of the 400 nm pulse and the transition dipole moment are stronger we expect the orbital coupling between the $3\sigma_g$ and $2\sigma_u$ to be stronger than anything coupled by the 800 nm pulse. Indeed this is the case as seen in figures 4.9a-b, where for $\theta = 0^o$ we expect that only the $3\sigma_g$ and $2\sigma_u$ are coupled and for the case of $\theta = 90^o$ where we also expect a coupling between the $3\sigma_g$ and $1\pi_u$ orbitals in addition to the other one. Thus we can confirm that the greatest contribution to the nonadiabatic effects is a result of the interaction with the 400 nm laser pulse.

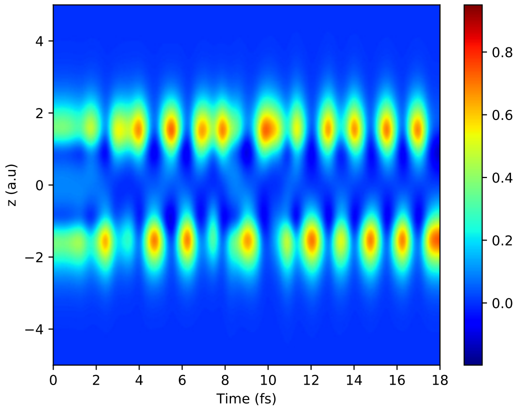

(a) $\theta = 0^o$

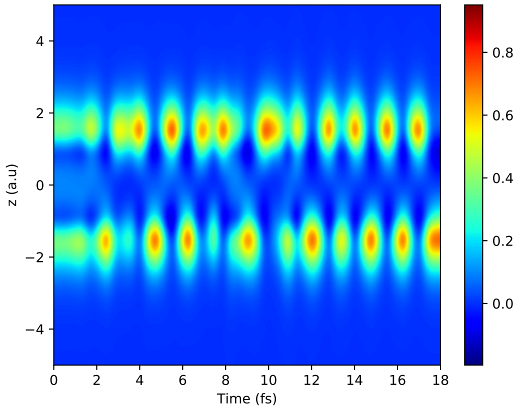

(b) $\theta = 10^o$

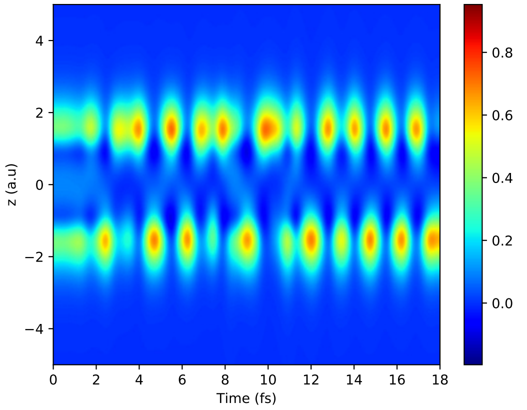

(c) $\theta = 20^o$

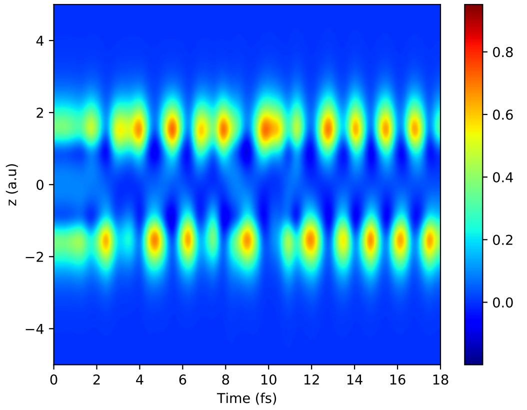

(d) $\theta = 30^o$

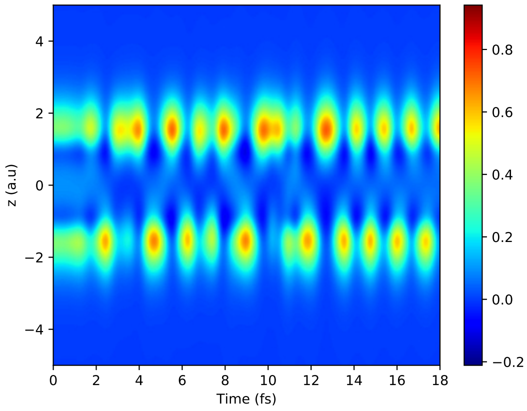

(e) $\theta = 40^o$

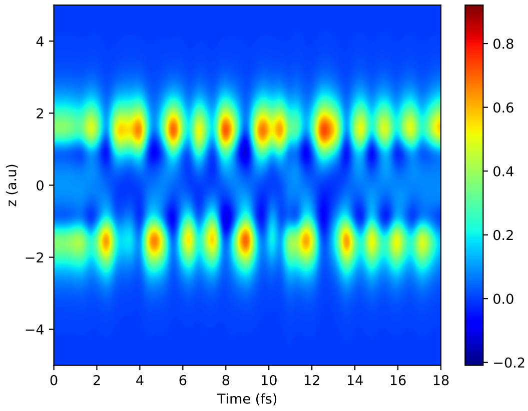

(f) $\theta = 50^o$

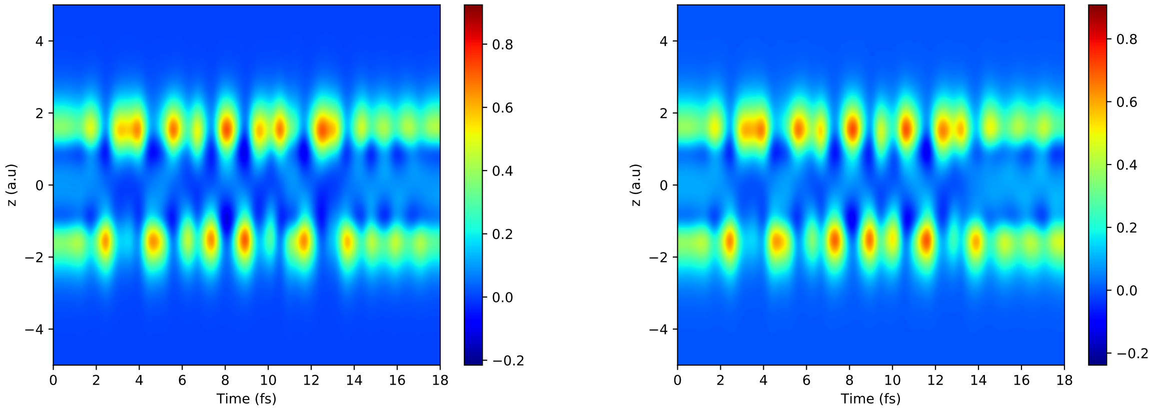

(g) $\theta = 60^o$

(h) $\theta = 70^o$

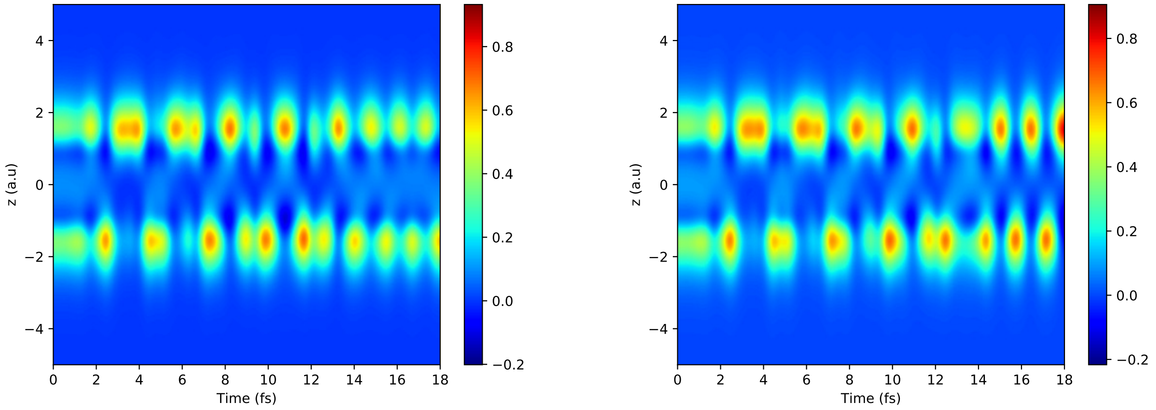

(i) $\theta = 80^o$

(j) $\theta = 90^o$

Figure 5.9: Visualization of electron localization of the total density of N_2^+ interacting with a 400 nm pulse of intensity $I = 2 \times 10^{14} \frac{W}{cm^2}$ with polarization fixed along the molecular axis, and an 800 nm pulse of intensity $I = 1 \times 10^{14} \frac{W}{cm^2}$ with polarization varied from $\theta = 0^o$ to $\theta = 90^o$ with respect to the molecular axis.

5.2.1 Individual Orbital Contributions to Two-Color Electron Localization

As we saw the presence of a second laser pulse does not enhance or suppress nonadiabatic dynamics in electron localization for the total electron density. However it is still worthwhile to investigate the individual orbitals and see if it is only the coupled ones that are exhibiting such effects or if others are indeed playing a role. We begin by looking at the case where the 800 nm pulse of intensity $I = 1 \times 10^{14} \frac{W}{cm^2}$ is oriented at an angle $\theta = 0^o$, figure 5.10. This case is identical to the single color case when only the $2\sigma_u$ and $3\sigma_g$ orbitals bring about the nonadiabatic dynamics. This is expected because the 400 nm pulse is the only one inducing a resonant coupling between orbitals while the 800 nm pulse does not induce a coupling when the polarization is oriented along the molecular axis.

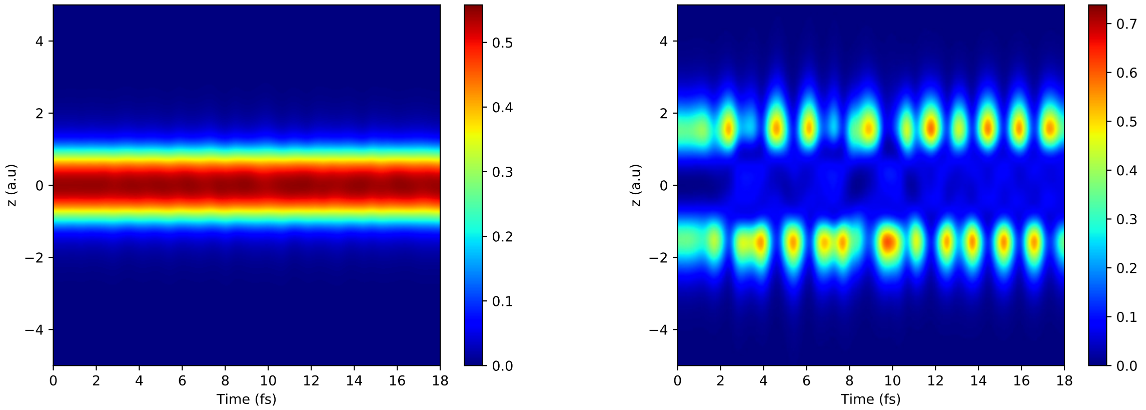

(a) $2\sigma_g$ $\theta = 0^o$

(b) $2\sigma_u$ $\theta = 0^o$

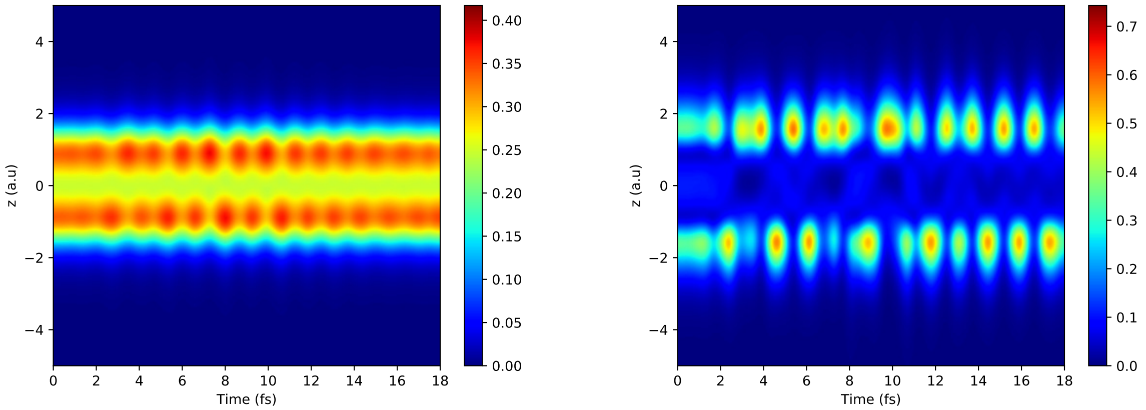

(c) $1\pi_u$ $\theta = 0^o$

(d) $3\sigma_g$

Figure 5.10: Visualization of orbital contributions to electron localization of N_2^+ in the presence of a 400 nm laser pulse with intensity $I = 2{\times}10^{14}\frac{W}{cm^2}$ and an 800 nm pulse with intensity $I = 1{\times}10^{14}\frac{W}{cm^2}$ both with polarization along the molecular axis. The orbitals are ordered, (a) $2\sigma_g$, (b) $2\sigma_u$, (c) $1\pi_u$, and (d) $3\sigma_g$.

We must turn back to the question of whether or not other orbitals exhibit such an effect when the angle θ of polarization is nonzero. We present results for the following angles: $\theta = 50^o$ and $\theta = 90^o$. We only consider these angles because presenting all of the figures for each angle would be in fact quite cumbersome and will not bring much into our discussion of what is occurring.

We consider the case where the angle is $\theta = 50^o$ shown in figure 5.11. We know that at this angle there is no induced coupling from the 800 nm laser however, we indeed see that the electron localization from the $1\pi_u$ orbital behaves adiabatically except near the end of the pulse where we begin to observe electron densities overlapping, and again this might not be a result of an induced coupling but rather perturbations from the ramping down of the laser pulse. The $3\sigma_g$ and $2\sigma_u$ orbitals still exhibit the most nonadiabatic behavior as is expected due to the resonant coupling by the 400 nm pulse. We can say that we do not expect the behavior from those two orbitals to change as we vary the angle of polarization of the 800 nm pulse.

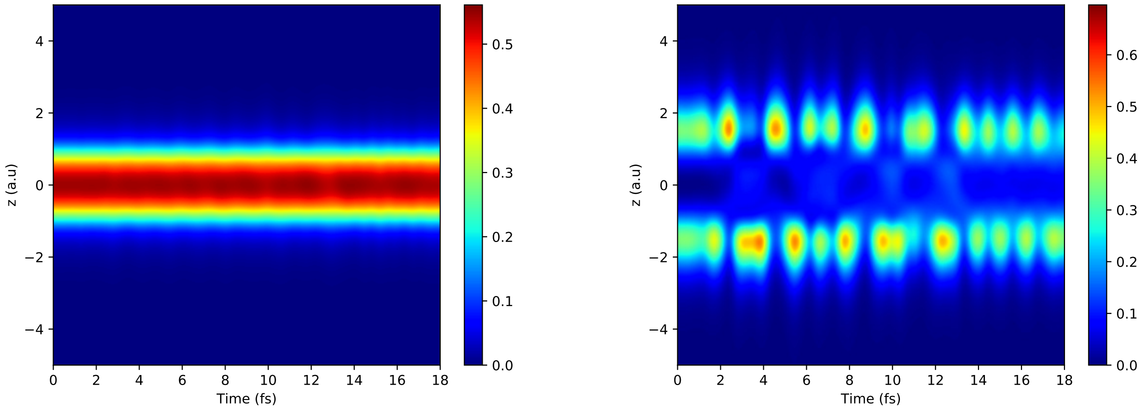

(a) $2\sigma_g$ $\theta = 50^o$

(b) $2\sigma_u$ $\theta = 50^o$

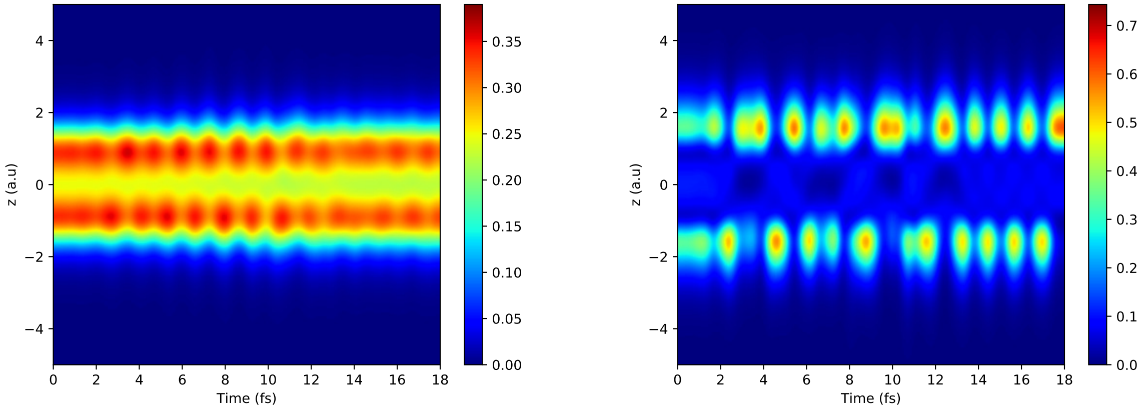

(c) $1\pi_u$ $\theta = 50^o$

(d) $3\sigma_g$ $\theta = 50^o$

Figure 5.11: Visualization of orbital contributions to electron localization of N_2^+ in the presence of a 400 nm laser pulse with intensity $I = 2 \times 10^{14} \frac{W}{cm^2}$ polarized along the molecular axis and an 800 nm pulse with intensity $I = 1 \times 10^{14} \frac{W}{cm^2}$ with polarization at an angle $\theta = 50^o$ with respect to the molecular axis. The orbitals are (a) $2\sigma_g$, (b) $2\sigma_u$, (c) $1\pi_u$, and (d) $3\sigma_g$.

On the other hand we know that there is an induced coupling between $3\sigma_g$ and $1\pi_u$ by an 800 nm pulse with polarization oriented perpendicular to the molecular axis. Oddly enough, we do not observe strong nonadiabatic effects arising in the electron localization of the $1\pi_u$ orbital when the angle is $\theta = 90^o$ with respect to the molecular axis. However this could be due to projecting the three-dimensional time-dependent electron density along the axis of the molecular axis. We stated before that this was the ideal axis onto which to project as it would allow us to observe the full features of electron localization, however this is not entirely true since the $1\pi_u$ orbital is not oriented along the molecular axis like the σ orbitals but rather perpendicular. Therefore, we consider the projection onto an axis perpendicular to the molecular axis and look at just the electron localization of the $1\pi_u$ orbital. Figures 5.13a-b presents such cases and indeed we can see that there is non-adiabatic electron localization present from the $1\pi_u$ orbital as a result of the second 800 nm laser pulse oriented (b) perpendicular to the molecular axis, compared to (a) when the 800 nm laser is oriented parallel to the molecular axis. Interestingly enough, while the case in which the 800 nm pulse has parallel polarization (a) exhibits adiabatic effects, the amount of electron density does not stay uniform. This could be a result of interferences occurring due to the other laser being present.

The results we presented confirm that both pulses are inducing separate resonant couplings, albeit of different strengths when the 400 nm pulse is parallel to the molecular axis and the 800 nm pulse is perpendicular. We then conclude that two-color interactions do indeed enhance nonadiabatic effects in electron localization, however with the caveat that certain effects can only be observed when projecting along specific dimensions as we have shown.

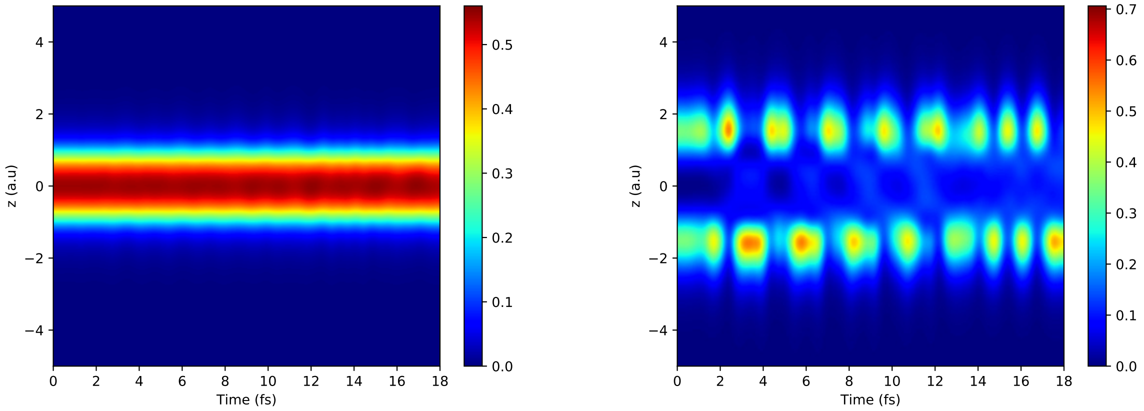

(a) $2\sigma_g$ $\theta = 90^o$ (b) $2\sigma_u$ $\theta = 90^o$

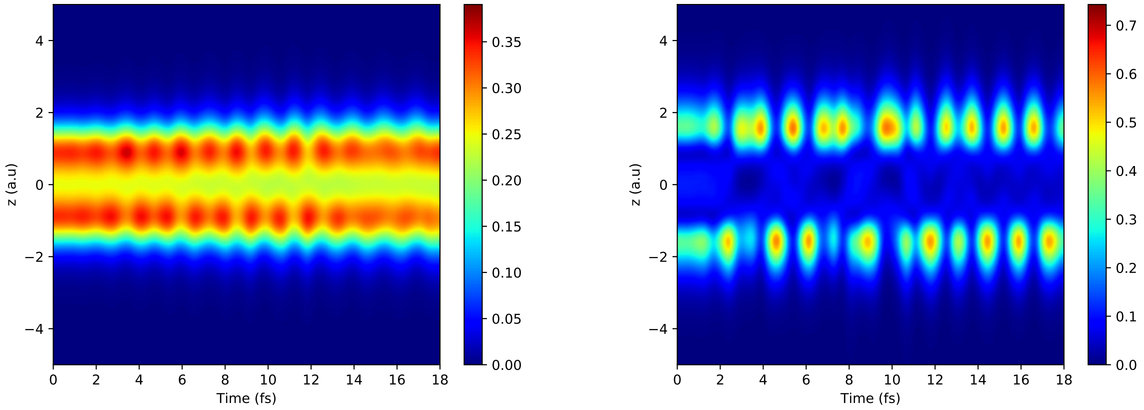

(c) $1\pi_u$ $\theta = 90^o$ (d) $3\sigma_g$ $\theta = 90^o$

Figure 5.12: Visualization of orbital contributions to electron localization of N_2^+ while in the presence of a 400 nm laser pulse with intensity $I = 2 \times 10^{14} \frac{W}{cm^2}$ polarized along the molecular axis and an 800 nm pulse with intensity $I = 1 \times 10^{14} \frac{W}{cm^2}$ with polarization at an angle $\theta = 90^o$ with respect to the molecular axis. The orbitals are (a) $2\sigma_g$, (b) $2\sigma_u$, (c) $1\pi_u$, and (d) $3\sigma_g$.

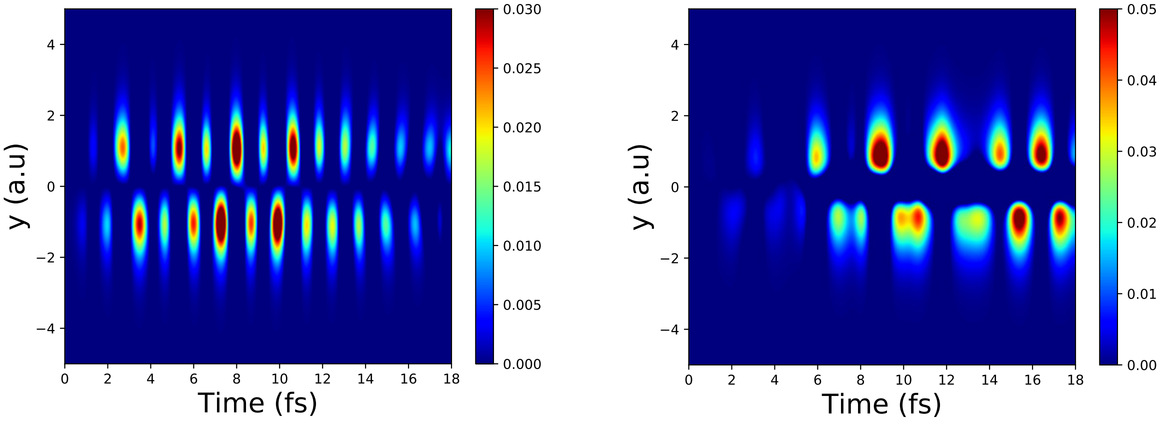

(a) $1\pi_u$, $\theta = 0^o$

(b) $1\pi_u$, $\theta = 90^o$

Figure 5.13: Visualization of electron localization for the $1\pi_u$ orbital projected along the direction of the orbitals rather than the molecular axis for the cases when the 800 nm pulse of intensity $1 \times 10^{14} \frac{W}{cm^2}$ is oriented at angles (a) $\theta = 0^o$ and (b) $\theta = 90^o$ with respect to the molecular axis.

5.3 Floquet Picture of Electron Localization

Aside from full 3-d calculations performed with Octopus, Floquet theory can provide a simple picture of localization. We do so by approximating the laser field as a CW field, and by considering a Hamiltonian for a two-level system that has the form:

$$H(t) = \frac{\Delta_0}{2}[\sigma_{uu} - \sigma_{gg}] - \mu_{gu}E(t)[\sigma_{gu} + \sigma_{ug}], \tag{5.5}$$

where Δ_0 is the energy difference between orbitals $|g\rangle$ and $|u\rangle$, $\sigma_{ij} = |i\rangle\langle j|$ (i,j $\in$ u,g), respectively, μ_{gu} is the transition dipole moment between orbitals, and E(t) is the applied laser field.
We consider an electric field that has a vector potential given by:

$$A(t) = A_o sin(\omega t + \phi) + \tilde{A}, \tag{5.6}$$

where A_o is the amplitude of the vector potential, ω is the optical frequency of the field, ϕ is some phase shift, and $\tilde{A}$ is an arbitrary shift to the vector potential that has no effect on the physical observables. This vector potential has a corresponding electric field given by:

$$E(t) = -\frac{dA(t)}{dt} = -E_o cos(\omega t + \phi), \tag{5.7}$$

where the field strength is given by $E_o = \omega A_o$. We then rewrite the above equations with a dimensionless coordinate $\tau = \omega t + \phi$, and obtain a TDSE given by:

$$i\frac{\partial}{\partial \tau}|\Psi(\tau)\rangle = \tilde{H}(\tau)|\Psi(\tau)\rangle, \tag{5.8}$$

where $\tilde{H}(\tau) = H(t(\tau))/\omega$. As is required by Floquet theory, we impose that the Hamiltonian be 2π periodic, so we can then say that this TDSE has a solution of the form:

$$|\Psi(\tau)\rangle = e^{-i\epsilon_j \tau}|\phi_j^F(\tau)\rangle,\ j = 1, 2. \tag{5.9}$$

where ϵ_j are the quasienergies of the Floquet states $|\phi_j^F\rangle$ which are eigenstates of the Floquet Hamiltonian described in equation (2.63). We can expand the quasienergies by making the approximation that the optical frequency of the field ω is much larger than the energy difference Δ_0 between states and/or the coupling between states is strong. The expansion is as follows:

$$\epsilon_1 = -\frac{\Delta_0}{2\omega}J_0(\zeta), \tag{5.10}$$

$$\epsilon_2 = \frac{\Delta_0}{2\omega}J_0(\zeta), \tag{5.11}$$

where $J_0(\zeta)$ is the zeroth-order Bessel function of the first kind, and $\zeta = \frac{2\mu_{gu}E_o}{\omega}$, which is a ratio of the Rabi frequency and the optical frequency of the field. With this we can then approximate the corresponding Floquet states given by (see [45] for a complete and detailed derivation):

$$\begin{aligned} |\phi_1^F(\tau)\rangle =& [cos(\phi(\tau)) + i\frac{\Delta_0}{\omega}cos(\phi(\tau))\xi_s(\tau) + i\frac{\Delta_0}{\omega}sin(\phi(\tau))\xi_a(\tau)]|g\rangle + \\ & [i\,sin(\phi(\tau)) + \frac{\Delta_0}{\omega}cos(\phi(\tau))\xi_a(\tau) - \frac{\Delta_0}{\omega}sin(\phi(\tau))\xi_s(\tau)]|u\rangle, \end{aligned} \tag{5.12}$$

$$\begin{aligned}|\phi_2^F(\tau)\rangle =&[i\,sin(\phi(\tau)) + i\frac{\Delta_0}{\omega}cos(\phi(\tau))\xi_a(\tau) + \frac{\Delta_0}{\omega}sin(\phi(\tau))\xi_s(\tau)]|g\rangle+ \\ &\big[cos(\phi(\tau)) - i\frac{\Delta_0}{\omega}cos(\phi(\tau))\xi_s(\tau) - i\frac{\Delta_0}{\omega}sin(\phi(\tau))\xi_a(\tau)]|u\rangle,\end{aligned} \tag{5.13}$$

where

$$\phi(\tau) = -\mu_{gu}[A(\tau) - \tilde{A}], \tag{5.14}$$

$$\xi_a = \sum_{k=0}^{\infty} J_{2k+1}(\zeta)\frac{cos[(2k+1)\tau]}{2k+1}, \tag{5.15}$$

$$\xi_s = \sum_{k=1}^{\infty} J_{2k}(\zeta)\frac{sin[2k\tau]}{2k}. \tag{5.16}$$

With all of the above the solution to equation (5.8) can be be expressed as a superposition of the Floquet states (5.12) and (5.13) given by:

$$|\Psi(\tau)\rangle = c_1 e^{-i\epsilon_1\tau}|\phi_1^F(\tau)\rangle + c_2 e^{-i\epsilon_2\tau}|\phi_2^F(\tau)\rangle, \tag{5.17}$$

where c_1 and c_2 are coefficients that are constant in time.

5.3.1 Two-Color Charge-Resonance Localization

As we have discussed, ionic diatomic molecules in the presence of a laser field can undergo a laser induced coupling when the optical frequency of the pulse is close to the resonant frequency between orbitals and the resulting electron density can oscillate between the two protons. We can extract the populations of the charge-resonant states given by the solution $|\Psi\rangle$ either from full 3-D calculations performed in Octopus or by using the two-state model described above in equation 5.5. We consider the superposition which describes the electron localization at one of the protons as:

$$|L\rangle = \frac{1}{\sqrt{2}}(|g\rangle + |u\rangle), \tag{5.18}$$

$$|R\rangle = \frac{1}{\sqrt{2}}(|g\rangle - |u\rangle), \tag{5.19}$$

we can then obtain the time-dependent local populations using:

$$P_L = \frac{|\langle L|\Psi\rangle|^2}{|\langle L|\Psi\rangle|^2 + |\langle R|\Psi\rangle|^2}, \tag{5.20}$$

$$P_R = \frac{|\langle R|\Psi\rangle|^2}{|\langle L|\Psi\rangle|^2 + |\langle R|\Psi\rangle|^2}. \tag{5.21}$$

We know that in H_2^+ we observe charge resonance pairs between $1\sigma_u$ and $2\sigma_g$ orbitals at large internuclear distances R. We then expect to see nonadiabatic effects in electron localization, and indeed this was shown by Takemoto and Becker [44] where they considered the internuclear distance of H_2^+ to be $R = 7$ a.u.. Figure 5.14 shows their results for electron localization for both the (c) full 3-D TDSE and (d) Floquet theory. We see that Floquet theory indeed captures the essence of nonadiabatic electron localization. However many of the features included in the full 3-D calculations are lost such as ionization of the electron into the continuum, similar to what occurs when using the optical Bloch equations to study HHG. Nevertheless, Floquet theory gives us some insight as to how the populations of electrons move around a molecule when there is a laser induced coupling between orbitals.

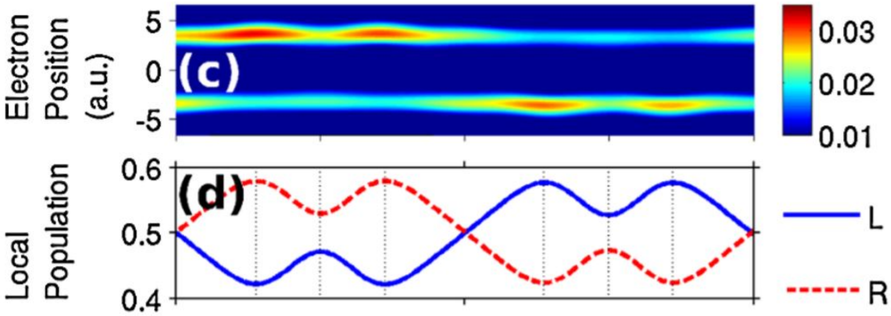

Figure 5.14: Electron localization for H_2^+ with internuclear distance $R = 7$ a.u. for the cases of (c) full 3-D TDSE, and (d) Floquet theory. Adapted from [44].

While the full 3-D TDSE and Floquet picture of electron localization seem to agree for the case of H_2^+ we must remind ourselves that this is a one electron system and that we are really interested in looking at the multielectron effects in nonadiabatic dynamics in molecules. Unfortunately such simple models as the one considered by the Hamiltonian in equation (5.5) fail to capture effects from electrons not in the orbitals we consider. However, even a simple model can provide some information about what is occurring and provide a simple picture that is otherwise too complicated to explain when looking at full 3-D TDDFT calculations.

We compare the dynamics of the two-level system to those obtained by performing full 3-D calculations on Octopus for N_2+ and $C_2H_4^+$. We begin by first extracting the transition dipole moments shown in table 5.1 by performing a DFT calculation in Octopus. This is done by taking the ground state wavefunctions and using the integral below to calculate the transition dipole moment.

$$\mu = \int \Psi_2^*(\vec{\mathbf{r}})\vec{\mathbf{r}}\Psi_1(\vec{\mathbf{r}})d^3\vec{\mathbf{r}}. \tag{5.22}$$

Laser Wavelength (nm)	Transition dipole moment	spin down (a.u)	spin up (a.u)
400	$\langle 3\sigma_g \vert x \vert 2\sigma_u \rangle$	1.558	1.5691
800	$\langle 3\sigma_g \vert y \vert 1\pi_u \rangle$	0.28682	0.23659
400	$\langle 1b_{2u} \vert x \vert 1b_{3g} \rangle$	-1.7231	1.7431

Table 5.1: Transition dipole moments for orbitals coupled by laser field of given wavelength for N_2^+ and $C_2H_4^+$.

Before going further we must consider the correct parameters, such that the quasienergies undergo a crossing, i.e., are degenerate. This is done by selecting an appropriate intensity of the pulse. In the figures 5.15a-c respectively, we show the quasienergies as a function of intensity for the cases of N_2^+ interacting with a 400 nm and 800 nm laser field, and $C_2H_4^+$ with a 400 nm field. From there we can choose an appropriate intensity in which there is a crossing, and set our laser fields accordingly. We can see that for N_2^+ there is a crossing at about $I = 1.5 \times 10^{15}\frac{W}{cm^2}$ for 400 nm, $I = 1.5 \times 10^{16}\frac{W}{cm^2}$ for 800 nm, and for $C_2H_4^+$ at $I = 4 \times 10^{16}\frac{W}{cm^2}$ for 400 nm.

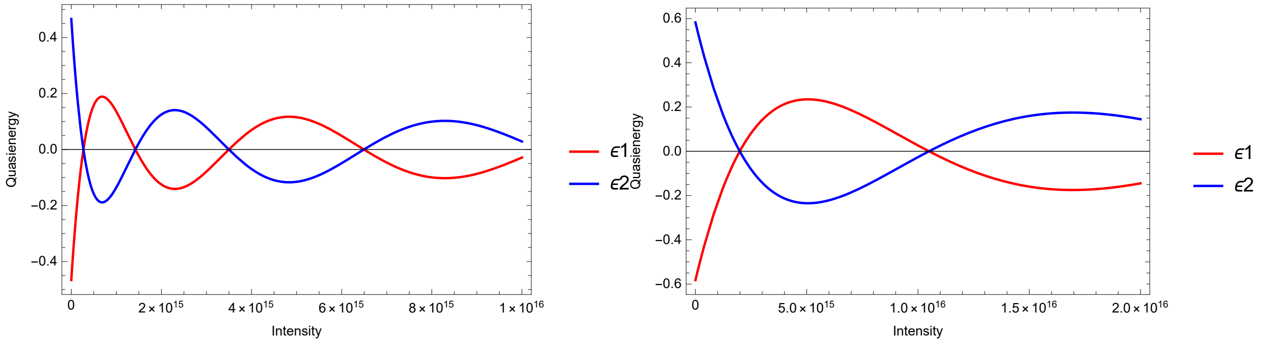

(a) N_2^+ $\lambda = 400$ nm

(b) N_2^+ $\lambda = 800$ nm

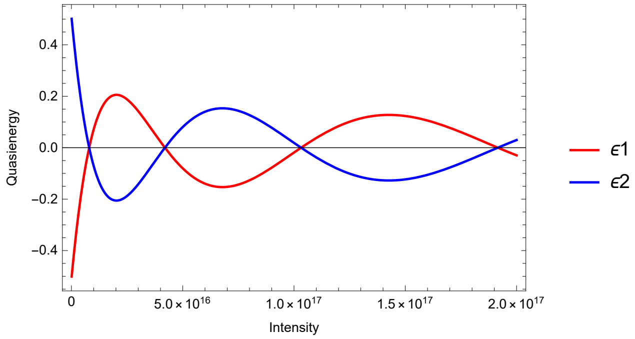

(c) $C_2H_4^+$ $\lambda = 400$ nm

Figure 5.15: Quasienergies ϵ_1 and ϵ_2 as functions of laser intensity.

We then use the chosen intensities and look at the left and right populations for each of the molecules. We first consider N_2^+ interacting with (a) a 400 nm pulse of intensity $I = 1.5 \times 10^{15} \frac{W}{cm^2}$ and (b) an 800 nm pulse of intensity $I = 1.5 \times 10^{16} \frac{W}{cm^2}$. Figures 5.16a-b show the respective left and right populations for cases (a) and (b). We see that during the propagation of the pulse the electron is localized at either the right or left side of the molecule. We note that the behavior of the oscillations of $P_L(t)$ and $P_R(t)$ is clearly nonadiabatic as there are instances during the propagation where the populations stay more localized on one of the sides of the molecule.

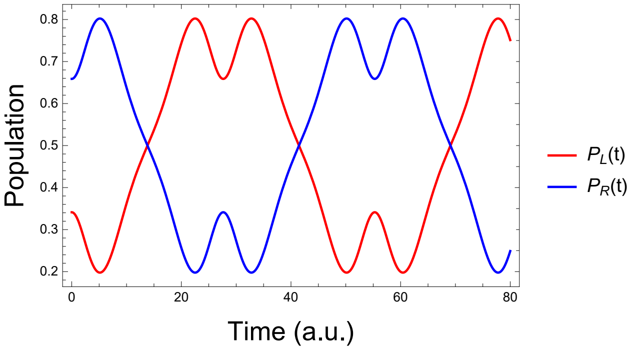

(a) N_2^+ $\lambda = 400$ nm

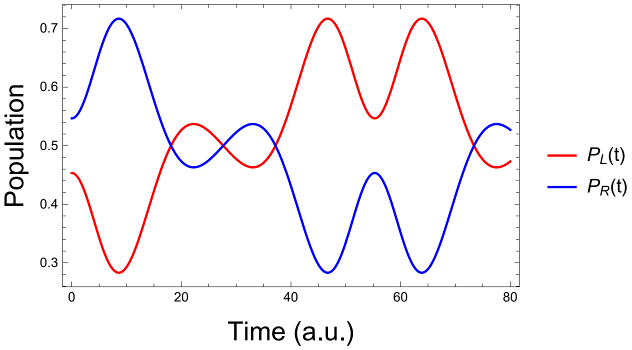

(b) N_2^+ $\lambda = 800$ nm

Figure 5.16: Time-dependent left- and right- populations for N_2^+ using the analytical solution obtained from Floquet theory for the cases where the laser is (a) at 400 nm with intensity $I = 1.5 \times 10^{15} \frac{W}{cm^2}$ and (b) at 800 nm with intensity $I = 1.5 \times 10^{16} \frac{W}{cm^2}$.

We now look at the time-dependent left and right populations of $C_2H_4^+$ interacting with a 400 nm laser at the chosen intensity $I = 4 \times 10^{16} \frac{W}{cm^2}$. Figure 5.17 shows both $P_L(t)$ and $P_R(t)$ for said case. It is evident that the behavior is nonadiabatic however we see more localization along the middle of the molecule at certain times. This is similar to the effects seen in the full 3-D TDDFT orbital contributions to localization for $C_2H_4^+$ (figure 5.7), where at certain times during the propagation of the pulse the electron is localized between the carbon nuclei.

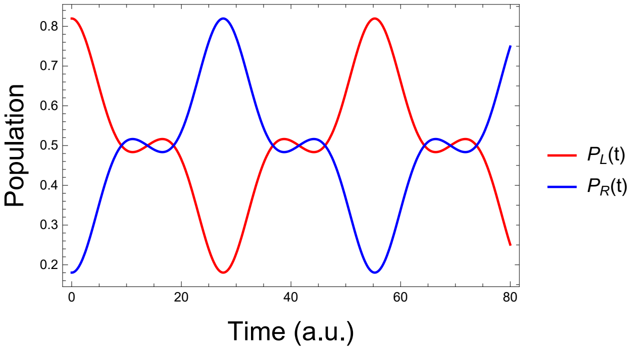

(a) $C_2H_4^+$ $\lambda = 400$ nm

Figure 5.17: Left- and right- time-dependent populations for $C_2H_4^+$ using the analytical solution obtained from Floquet Theory for the case where the laser is 400 nm with intensity $I = 1.5\times10^{15}\frac{W}{cm^2}$.

In conclusion, we see that a simple two-level system can in fact predict electron localization in molecules when there is a laser induced resonance between orbitals. However, we note that the perspective we gain by using this model is different than when using TDDFT, and we must analyze electron localization using of left- and right- localized orbitals/states (*i.e.,* charge resonance states) and populations which tell us that the population of laser induced charge resonance pairs is localized on either side of the molecule and that each population behaves nonadiabatically when there is a resonance between orbitals. While the model helps predict some of the mentioned effects we must take into consideration that we are neglecting full multielectron effects and ionization into the continuum that we can otherwise observe with the use of TDDFT. Nonetheless, the model helps to simplify the effects occurring in nonadiabatic electron localization.

5.4 Summary

In this chapter we investigated the appearance of nonadiabatic effects in electron localization for N_2^+ and $C_2H_4^+$. We first considered the case where one laser pulse induces a coupling between orbitals, and studied at the total electron localization and the orbital contributions of localization. We determined that there are several competing processes that contribute to nonadiabatic electron localization: (1) the oscillation of the electrons with the electric field and (2) the oscillation at the Rabi frequency of the electrons coupled by the field. We then investigated the case where our system interacts with two linearly polarized pulses, and exhibited the differences that arise in nonadiabatic behavior of electron localization as a consequence of the addition of the second pulse. Finally we investigated nonadiabatic electron localization with the use of Floquet theory for a two-level system and analyzed how the population of the coupled orbitals varied between the left and right sides of the molecule as a function of time and confirmed that in the case of a resonant coupling nonadiabatic behavior was evident. We also saw that while the way we looked at localization using Floquet theory was different as compared to full TDDFT calculations, it gave a simple description of the more complex dynamics occurring in the full 3-D model.

Chapter 6

Summary, Discussion, and Outlook

6.1 Summary and Discussion

In this thesis we investigated how multielectron effects play a role in the interactions between molecules and intense ultrashort pulse lasers in the context of high harmonic generation, strong-field ionization, and electron localization. We considered various theories such as time-dependent density-functional theory, optical Bloch equations, and Floquet theory to analyze our results and compared each theory with each other.

In chapter 3 we studied the multielectron effects in molecules for HHG. We saw that a laser induced coupling leads to the appearance of Mollow sidebands in HHG spectra for the cases of single-color and two-color linearly polarized laser interactions for N_2^+. We compared both TDDFT and optical Bloch equations and found that while both theories vary greatly in complexity, they both capture the essence of Rabi oscillations and hence the appearance of Mollow sidebands. We also analyzed how the pulse envelope affects the resolution of the Mollow sidebands for $C_2H_4^+$ and found that their appearance is greatly dependent on the laser pulse envelope used. We then investigated the generation of elliptically polarized harmonics from CO_2 for various intensities and investigated the orbital contributions to ellipticity. Furthermore we compared the results to those obtained in experiment and found that the theory and experiment agree. Finally we considered the interaction of H_2 and H_2^+ with circularly polarized bichromatic pulses of commensurate frequencies for the cases where they are co- and counter-rotating and found that the HHG spectra show features of the three-step model breakdown meaning that it must be modified for situations where the pulse is not linearly polarized.

In Chapter 4 we considered the effects of strong-field ionization for both N_2^+ and $C_2H_4^+$ in the cases where there was a laser induced coupling between orbitals and observed that the coupling enhances ionization from inner shell orbitals that are coupled by the field in the form of charge-resonance enhanced ionization. We then considered the case of interactions of N_2^+ with two-color linearly polarized pulses where one pulse had fixed polarization and the other had polarization varied from $\theta = 0^o$ to $\theta = 90^o$. We found that the case where a 400 nm pulse had fixed polarization parallel to the molecular axis and an 800 nm pulse had polarization rotated behaved almost analogous to the single-color 400 nm pulse case. In contrast, in the case where the 800 nm pulse had polarization fixed perpendicular to the molecular axis and a 400 nm pulse had polarization varied behaved different than what we have predicted based on previous results and that coupling between orbitals remained even at polarization orientations where we would expect there not to be any coupling, thus enhancing ionization.

Finally in chapter 5 we investigated the appearance of nonadiabatic behavior in electron localization for both N_2^+ and $C_2H_4^+$ in the cases were a laser pulse induced a coupling between orbitals. We observed such behavior in the cases of single color interactions and saw that it is apparent in the total electron density and the single orbital density, which led us to the conclusion that there are two underlying competing processes: (1) the electrons oscillate with the field, and (2) the electrons in the coupled orbitals oscillate at the Rabi frequency which leads to nonadiabatic behavior in electron localization. We then considered the case of two-color interactions similar to the other chapters and observed that the addition of a second laser pulse does not enhance or suppress nonadiabatic behavior in electron localization. Finally we looked at the Floquet picture of electron localization in the context of how the population varied from side to side of the molecule and found that while it gives a different picture than that obtained with TDDFT, the idea that laser induced coupling between orbitals leads to nonadiabatic behavior is the same as that observed in TDDFT.

6.2 Outlook

While the analysis for many of our results were conclusive, there are certain open questions that remain when looking at the cases were there is a two-color laser pulse interaction with molecules. In particular a question remains in the case where the 400 nm laser pulse had its polarization direction rotated from $\theta = 0^o$ to $\theta = 90^o$ with respect to the molecular axis and the 800 nm laser pulse had polarization direction fixed perpendicular to the molecular axis. There appears to be a coupling of the $3\sigma_g$ and $2\sigma_u$ orbitals even when the polarization direction of the 400 nm laser pulse was not parallel to the molecular axis. Perhaps with more allotted time, we could have looked further in to this to get a more detailed answer than what was provided in previous discussion in this thesis. Other interesting cases could have been considered such as studying molecules different than CO_2, N_2^+, and $C_2H_4^+$ and applying similar scenarios as in this thesis and see if any of the effects discussed change or if they remain the same or similar. Lastly, we could have further changed the way we performed our calculations and investigated how different, if at all, our results would have been. Such examples include trying different time-propagators aside from Crank-Nicolson, trying different functionals, and even different space-time grids.

Bibliography

[1] L. Keldysh. *Ionization in the field of a strong electromagnetic wave.* Sov. Phys. JETP, 20:1307, 1965.

[2] F. H. M. Faisal. *Multiple absorption of laser photons by atoms.* J. Phys. B, 6:L89, 1973.

[3] H. R. Reiss. *Effect of an intense electromagnetic field on weakly bound system.* Phys. Rev. A, 22:1786, 1980.

[4] Z. Vager, R. Naaman, and E. P. Kanter. *Coulomb explosion imaging of small molecules.* Science, 244:426431, 1989.

[5] P. H. Bucksbaum, A. Zavriyev, H. Muller, and D. W. Schumacher. *Softening of the H_2^+ molecular bond in intense laser fields.* Phys. Rev. Lett., 64:1883, 1990.

[6] A. Giusti-Suzor, X. He, O. Atabek, and F. H. Frederic. *Above-threshold dissociation of H_2^+ in intense laser fields.* Phys. Rev. Lett., 64:515, 1990.

[7] A. Etches, M. B. Gaarde, and L. B. Madsen. *Two-center minima in harmonic spectra from aligned polar molecules.* Phys. Rev. A, 84:023418, 2011.

[8] M. Lein, N. Hay, R. Velotta, J. P. Marangos, and P. L. Knight. *Interference effects in highorder harmonic generation with molecules.* Phys. Rev. A, 66:023805, 2002.

[9] J. Muth-Böhm, A. Becker, and F. H. M. Faisal. *Suppressed molecular ionization for a class of diatomics in intense femtosecond laser fields.* Phys. Rev. Lett., 85:2280, 2000.

[10] A. Jaron-Becker, A. Becker, and F. H. M. Faisal. *Saturated ionization of fullerenes in intense laser fields.* Phys. Rev. Lett., 96:143006, 2006.

[11] A.L. Marques, N.T. Maitra, F. Nogueira, E.K.U. Gross, and A. Rubio (Eds.), Lecture Notes in Physics, Vol. 837. *Fundamentals of time-dependent density functional theory.* (Springer, Berlin), (2012), ISBN: 978-3-642-23518-4.

[12] M.A.L. Marques and E.K.U. Gross. *Time-dependent density functional theory.* Annu. Rev. Phys. Chem. **55**: 427-455 (2004).

[13] C. A. Ullrich. *Time-Dependent Density-Functional Theory Concepts and Applications.* Oxford, University Press, 2012.

[14] A. Castro, M.A Marques, and A. Rubio. *Propagators for the time-dependent KohnSham equations.* J. Chem. Phys. **121**: 3425 (2004).

[15] A. Castro, H. Appel, Micael Oliveira, C.A. Rozzi, X. Andrade, F. Lorenzen, M.A.L. Marques, E.K.U. Gross, and A. Rubio. *Octopus: a tool for the application of time-dependent density functional theory.* Phys. Stat. Sol. B **243**: 2465-2488 (2006).

[16] X. Andrade, D. A. Strubbe, U. De Giovannini, A. H. Larsen, M. J. T. Oliveira, J. Alberdi-Rodriguez, A. Varas, I. Theophilou, N. Helbig, M. Verstraete, L. Stella, F. Nogueira, A. Aspuru-Guzik, A. Castro, M. A. L. Marques, and A. Rubio. *Real-space grids and the Octopus code as tools for the development of new simulation approaches for electronic systems.* Phys Chem Chem Phys **17**: 31371-31396 (2015).

[17] M.A.L. Marques, A. Castro, G. F. Bertsch, and A. Rubio. *Octopus: a first-principles tool for excited electron-ion dynamics.* Comput. Phys. Commun. **151**: 60-78 (2003).

[18] C. Legrang, E. Suraud, and P.-G. Reinhard. *Comparison of self-interaction-corrections for metal clusters.* J. Phys. B: At. Mol. Opt. Phys. **35** 1115 (2002).

[19] D.M. Gaudiosi, B.A. Reagan, T. Popmintchev, M.E. Grisham, M.A. Berrill, O. Cohen, B.C. Walker, M.M Murnane, H.C. Kapteyn, J.J. Rocca. *High harmonic generation from ions in a capillary discharge plasma waveguide.* Optics and Photonics News Vol. 17, Issue 12, 44 (2006).

[20] D. Popmintchev, C. Hernandez-Garca, F. Dollar, C. Mancuso, J. Perez-Hernandez, M.C. Chen, A. Hankla, X. Gao, B. Shim, A. Gaeta, M. Tarazkar, D. Romanov, R. Levis, J. Gaffney, M. Foord, S. Libby, A. Jaron-Becker, A. Becker, L. Plaja, M. Murnane, H. Kapteyn, and T. Popmintchev. *Efficient soft X-ray high harmonic generation in multiply-ionized plasmas: the ultraviolet surprise.* Science, **350**: 1225, (2015).

[21] E. Muybridge. *The horse in motion.* URL http://hdl.loc.gov/ loc.pnp/cph.3a45870.

[22] P. B. Corkum. *Plasma perspective on strong field multiphoton ionization.* Phys. Rev. Lett., 71:1994, 1993.

[23] M. Lewenstein, P. Balcou, M. Yu. Ivanov, A. LHullier, and P. B. Corkum. *Theory of high harmonic generation by low frequency laser fields.* Phys. Rev. A, 49:2117, 1994.

[24] X. Zhou, R. Lock, N. Wagner, W. Li, H. C. Kapteyn, and M. M. Murnane. *Elliptically polarized high-order harmonic emission from molecules in linearly polarized laser fields.* Phys. Rev. Lett., 102:073902, 2009.

[25] Y. Mairesse, J. Higuet, N. Dudovich, D. Shafir, B. Fabre, E. Mevel, E. Constant, S. Patchkovskii, Z. Walters, M. Y. Ivanov, and O. Smirnova. *High harmonic spectroscopy of multichannel dynamics in strong-field ionization.* Phys. Rev. Lett., 104:213601, 2010.

[26] A. T. Le, R. R. Lucchese, and C. D. Lin. *Polarization and ellipticity of high-order harmonics from aligned molecules generated by linearly polarized intense laser pulses.* Phys. Rev. A, 82,2010

[27] T. Zuo, S. Chelkowski, and A. D. Bandrauk. *Photon-emission spectra of the* H_2^+ *molecular ion in an intense laser field.* Phys. Rev. A, 49:3943, 1994.

[28] T. Zuo, S. Chelkowski, and A. D. Bandrauk. *Harmonic generation by the H_2^+ molecular ion in intense laser fields.* Phys. Rev., 48:3837, 1993.

[29] H. Eichmann, A. Egbert, S. Nolte, C. Momma, B. Wellegehausen, W. Becker, S. Long, and J. K. McIver. *Polarization-dependent high-order two-color mixing.* Phys. Rev. A 51, R3414, 1995.

[30] D. B. Milošević, W. Becker, and R. Kopold. *Generation of circularly polarized high-order harmonics by two-color coplanar field mixing.* Phys. Rev. A 61, 063403, 2000.

[31] M. Kbel, Z. Dube, A.Yu. Naumov, M. Spanner, G.G. Paulus, M.F. Kling, D.M. Villeneuve, P.B. Corkum, and A. Staudte. *Streak Camera for Strong-Field Ionization.* Phys. Rev. Lett. **119**, 183201 (2017).

[32] E. Constant, V. D. Taranukhin, A. Stolow, and P.B. Corkum. *Methods for the measurement of the duration of high-harmonic pulses.* Phys. Rev. A 56, 3870, 1997.

[33] M. Hentschel, R. Kienberger, Ch. Spielmann, G. A. Reider, N. Milosevic, T. Brabec, P. Corkum, U. Heinzmann, M. Drescher and F. Kraus. *Attosecond metrology.* Nature 414, 509-513, 2001.

[34] J. Itatani, F. Qur, G. L. Yudin, M. Yu. Ivanov, F. Krausz, and P. B. Corkum. *Attosecond Streak Camera.* Phys. Rev. Lett. 88, 173903, 2002.

[35] H.G. Muller. *Reconstruction of attosecond harmonic beating by interference of two-photon transitions.* Applied Physics B, Volume 74, Number 1, Page s17, 2002.

[36] M. Isinger, D. Busto, S. Mikaelsson, S. Zhong, C. Guo, P. Salires, C. L. Arnold, A. L'Huillier and M. Gisselbrecht. *Accuracy and precision of the RABBIT technique.* Philosophical Transactions of the Royal Society A: Mathematical, Physical and Engineering Sciences, 377, 2145, 2019.

[37] G. N. Gibson, R. R. Freeman, and T. J. Mcllrath. *Dynamics of the high-intensity multiphoton ionization of N_2.* Phys. Rev. Lett., 67:1230, 1991.

[38] S. L. Chin, Y. Liang, J. E. Decker, F. A. IIkov, and M. V. Ammosov. *Tunnel ionization of diatomic molecules by an intense CO_2 laser.* J. Phys. B, 25:L249, 1992

[39] T. D. G. Walsh, J. E. Decker, and S. L. Chin. *Tunnel ionization of simple molecules by an intense CO_2 laser.* J. Phys. B, 26:L85, 1993.

[40] J. Muth-Böhm, A. Becker, and F. H. M. Faisal. *Suppressed molecular ionization for a class of diatomics in intense femtosecond laser fields.* Phys. Rev. Lett., 85:2280, 2000.

[41] P. Agostini, F. Fabre, G. Mainfray, G. Petite, and N. K. Rahman. *Free-free transitions following six-photon ionization of xenon atoms.* Phys. Rev. Lett., 42:11271130, 1979.

[42] L. Keldysh. *Ionization in the field of a strong electromagnetic wave.* Sov. Phys. JETP, 20:1307, 1965.

[43] T. Zuo and A. D. Bandrauk. *Charge-resonance-enhanced ionization of diatomic molecular ions by intense lasers.* Phys. Rev. A, 52:R2511, 1995.

[44] N. Takemoto and A. Becker. *Time-resolved view on charge-resonance-enhanced ionization.* Phys. Rev. A, 84:023401, 2011.

[45] A. Santana, J. M. G. Llorente, and V. Delgado. *Semiclassical dressed states of two-level quantum systems driven by non-resonant and/or strong laser fields.* J. Phys. B 34, 2371 (2001).

[46] T. Popmintchev, M. C. Chen, P. Arpin, M. M. Murnane, and H. C. Kapteyn. *The attosecond nonlinear optics of bright coherent X-ray generation.*. Nat. Photonics, **4**:822832, 2010.

[47] J. Anderson, P. J. Burns, D. Milroy, P. Ruprecht, T. Hauser, and H. J. Siegel. *Deploying RMACC Summit: An HPC Resource for the Rocky Mountain Region.*. In Proceedings of PEARC17, New Orleans, LA, USA, July 09-13, 2017. DOI: 10.1145/3093338.3093379

Appendix A

This work utilized the RMACC Summit supercomputer, which is supported by the National Science Foundation (awards ACI-1532235 and ACI-1532236), the University of Colorado Boulder, and Colorado State University. The Summit supercomputer is a joint effort of the University of Colorado Boulder and Colorado State University [47]. In addition to Summit, the work presented in this thesis utilized the JILA computing clusters for calculations.